

# A Search for Excited Quarks with the H1 Detector at HERA

Dissertation

zur

Erlangung der naturwissenschaftlichen Doktorwürde  
(Dr. sc. nat.)

vorgelegt der  
Mathematisch-naturwissenschaftlichen Fakultät  
der

Universität Zürich

von

**Jan Becker**

aus

Deutschland

**Promotionskomitee**

Prof. Dr. Ulrich Straumann (Vorsitz)  
Prof. Dr. Peter Truöl  
Dr. Katharina Müller  
Dr. Stefan Schmitt

Zürich 2005



## Zusammenfassung

Diese Arbeit beschreibt die Suche nach angeregten Quarkzuständen  $q^*$  der ersten Generation bei  $e^+p$ -Streuungen an dem HERA Speicherring am DESY. Die Analyse beruht auf Daten, die in den Jahren 1999 und 2000 bei einer Schwerpunktsenergie von  $\sqrt{s} \approx 319$  GeV mit dem H1 Detektor gesammelt wurden. Die analysierten Daten entsprechen einer integrierten Luminosität von  $63 \text{ pb}^{-1}$ .

Der elektroschwache Zerfallskanal des angeregten Quarks:  $q^* \rightarrow q \gamma$  in ein Photon und einen Jet wurde exklusiv untersucht. Es wurden keine signifikanten Anzeichen für die Produktion von angeregten Quarks gefunden. Massen abhängige obere Grenzen für den Wirkungsquerschnitt der Erzeugung von angeregten Quarks und dem Verhältnis der Kopplungskonstante zur Zusammensetzungsskala (compositeness scale) wurden berechnet. Die Ergebnisse werden mit der aktuellen H1 Publikation zur Erzeugung angeregter Fermionen verglichen. Die Grenzen konnten im Vergleich zur Publikation für Massen größer als 100 GeV verbessert werden.

## Abstract

This thesis presents the analysis of the search for excited quark  $q^*$  of the first generation in  $e^+p$ -scattering at the collider HERA. The analysis is based on data taken 1999 and 2000 at a centre-of-mass energy of  $\sqrt{s} \approx 319$  GeV with the H1 detector with an integrated luminosity of  $63 \text{ pb}^{-1}$ .

The electroweak decay channel of the excited quark:  $q^* \rightarrow q \gamma$  into a photon and a jet is exclusively taken into account. No evidence for  $q^*$  production is found. Mass dependend exclusion limits on cross-sections and the ratio of coupling constants to the compositeness scale are derived. The results are compared to the recent H1 publication on the production of excited fermions. The calculated Limits have been improved with respect to the publication in mass regions larger than 100 GeV..



# Contents

<b>1</b>	<b>Introduction</b>	<b>1</b>
<b>2</b>	<b>The Standard Model and beyond</b>	<b>3</b>
2.1	Standard Model of electroweak and strong interactions . . . . .	3
2.2	Physics beyond the Standard Model . . . . .	4
2.2.1	Supersymmetry . . . . .	5
2.2.2	GUT . . . . .	8
2.3	Compositeness and Excited Quarks . . . . .	9
<b>3</b>	<b>HERA and the H1 Detector</b>	<b>12</b>
3.1	The HERA Collider . . . . .	12
3.2	The H1 detector . . . . .	14
3.2.1	Calorimeters . . . . .	16
3.2.2	Tracking System . . . . .	20
3.2.3	Time-of-Flight detectors . . . . .	21
3.2.4	Luminosity Measurement . . . . .	22
3.3	The H1 Trigger and Data Acquisition . . . . .	22
<b>4</b>	<b>Background processes at HERA</b>	<b>26</b>
4.1	Kinematics and cross sections of positron-proton interactions . . .	27
4.2	Neutral Current DIS . . . . .	30
4.2.1	Radiative Processes . . . . .	30
4.3	Photoproduction . . . . .	32
4.3.1	Dijet Photoproduction . . . . .	32
4.3.2	Prompt Photon Production . . . . .	33

<b>5</b>	<b>Analysis of the production of Excited Quarks</b>	<b>34</b>
5.1	Data, Background and Signal Samples . . . . .	34
5.2	Preselection . . . . .	37
5.3	Detection of Electromagnetic Particles . . . . .	42
5.4	Detection of Jets . . . . .	44
5.5	Final Selection . . . . .	47
5.5.1	Cuts on electromagnetic particle variables . . . . .	48
5.5.2	Cuts on jet variables . . . . .	51
5.5.3	Photon detection . . . . .	55
5.5.4	Final cuts and comparison to former H1 publication . . . . .	60
<b>6</b>	<b>Limits on the production of Excited Quarks</b>	<b>66</b>
6.1	Introduction to limit calculations . . . . .	66
6.1.1	Likelihood Ratio . . . . .	66
6.1.2	Confidence levels . . . . .	67
6.2	Upper limits on cross-sections . . . . .	67
6.3	Upper limits on coupling parameters . . . . .	69
<b>7</b>	<b>Conclusions and Outlook</b>	<b>72</b>
<b>A</b>	<b>Event Displays of Final Events</b>	<b>74</b>
<b>B</b>	<b>CIP2000 Trigger Readout System</b>	<b>78</b>
B.1	CIP2000 Trigger System Overview . . . . .	78
B.2	CIP2000 Trigger System Readout Structure . . . . .	80
B.3	CIP2000 Trigger System Readout hardware . . . . .	82
B.3.1	Connection of CPU and trigger card: VME . . . . .	82
B.3.2	Trigger card . . . . .	84
B.3.3	CPU board . . . . .	85
B.3.4	Connection of CPUs: pVIC . . . . .	87
B.3.5	Connection between different VME busses: VIC . . . . .	88
B.4	CIP2000 Trigger System Readout software . . . . .	90
	<b>Acknowledgements</b>	<b>98</b>
	<b>Curriculum Vitae</b>	<b>100</b>

# List of Figures

2.1	Leading diagram for the production and decay of excited quarks in ep collisions . . . . .	10
2.2	Detector signature for the decay of an excited quark . . . . .	11
3.1	The HERA storage ring . . . . .	12
3.2	Annual integrated luminosity of HERA and H1 . . . . .	13
3.3	Overview of the H1 detector . . . . .	15
3.4	Longitudinal cut through the LAr calorimeter . . . . .	16
3.5	Transverse cut through the LAr calorimeter . . . . .	17
3.6	Longitudinal cut through the H1 tracking system . . . . .	20
3.7	Transverse cut through the central tracking chambers . . . . .	21
3.8	Principle of pipelining in H1 subsystems . . . . .	23
3.9	Principle of the H1 detector readout . . . . .	24
4.1	Neutral current and charged current process diagrams . . . . .	27
4.2	Initial and final state photon radiation diagrams . . . . .	31
4.3	Direct and resolved dijet photoproduction diagrams . . . . .	33
4.4	Direct and resolved prompt photon production diagrams . . . . .	33
5.1	Distribution of z-vertex Position . . . . .	38
5.2	Trigger efficiency for subtrigger S67 with respect to $\theta_{em}$ and $E_T$ . . . . .	39
5.3	Distribution of $y_e$ . . . . .	40
5.4	Distribution of $(E - P_z)$ . . . . .	40
5.5	Efficiency of preselection on MC signal data samples . . . . .	41
5.6	Distribution of $\theta$ of first em particle after preselection . . . . .	43
5.7	Distribution of $p_T$ of first em particle after preselection . . . . .	44
5.8	Distribution of $\theta$ of first jet after preselection . . . . .	46
5.9	Distribution of the energy of the first jet after preselection . . . . .	47

5.10	Efficiency and rejection power of cut on $p_T$ of first em particle . . .	48
5.11	Efficiency and rejection power of cut on $\theta$ of first em particle . . .	49
5.12	Distribution of $p_T$ of first em particle after final cut on $\theta$ of first em particle . . . . .	50
5.13	Distribution of $\theta$ of first em particle after final cut on $p_T$ of first em particle . . . . .	50
5.14	Distribution of distance of first jet and first em particle in $\theta$ and $\phi$	51
5.15	Efficiency and rejection power of cut on the energy of first jet . . .	52
5.16	Efficiency of energy cut of first jet with respect to $\theta$ of first em particle . . . . .	53
5.17	Distribution of the energy of first jet after cuts on first em particle variables $p_T$ and $\theta$ and jet energy . . . . .	54
5.18	Distribution of $\theta$ of first jet after cuts on first em particle variables $p_T$ and $\theta$ and jet energy . . . . .	54
5.19	Distance between LAr cluster and track after preselection . . . . .	55
5.20	Distance between LAr cluster and CIP hit after preselection . . . . .	56
5.21	Efficiency of tracking cuts with respect to $\theta$ of first em particle . . .	56
5.22	Efficiency of tracking cuts with respect to $\phi$ of first em particle . . .	57
5.23	Photon conversion rate with respect to $\theta$ of first em particle . . . . .	57
5.24	Event display of cosmic muon filtered out by visual scan . . . . .	60
5.25	Distribution of invariant mass calculated from jet and photon . . . . .	62
5.26	Distribution of $\theta$ and $p_T$ of first em particle after final selection . . .	63
5.27	Distribution of $\theta$ and energy of first jet after final selection . . . . .	64
5.28	Distribution of missing $p_T$ after preselection and final selection . . .	64
6.1	Extrapolation of optimal mass windows . . . . .	68
6.2	Limit on the production cross-section of excited quark . . . . .	69
6.3	Branching ratio for the photon, W and Z branch in u-quark decay	70
6.4	Branching ratio for the photon, W and Z branch in d-quark decay	70
6.5	Limit on the coupling parameters for excited quark . . . . .	71
A.1	Event display of final data event number: 41978, run: 255579 . . . . .	74
A.2	Event display of final data event number: 68646, run: 256879 . . . . .	75
A.3	Event display of final data event number: 54795, run: 264978 . . . . .	75
A.4	Event display of final data event number: 19635, run: 268175 . . . . .	76
A.5	Event display of final data event number: 17345, run: 276828 . . . . .	76

A.6	Event display of final data event number: 18086, run: 277142 . . .	77
A.7	Event display of final data event number: 147679, run: 278419 . .	77
B.1	Schematic overview of the CIP2000 trigger system . . . . .	79
B.2	CIP2000 trigger readout structure . . . . .	81
B.3	Structure of VME functional modules and buses . . . . .	82
B.4	Address mapping to the VME resources on the trigger cards . . .	85
B.5	Structure of the RIO2 8062 PC board . . . . .	86
B.6	VIC 8250 module structure . . . . .	89
B.7	Readout structure of the CIP2000 trigger readout system software	91
B.8	Eventbuffer structure . . . . .	92

# List of Tables

2.1	Chiral supermultiplets in the MSSM . . . . .	7
2.2	Gauge supermultiplets in the MSSM . . . . .	7
5.1	Summary of data sets and Monte Carlo samples . . . . .	35
5.2	Cuts of preselection applied to all data sets . . . . .	42
5.3	Cut efficiencies for different cuts on first em particle variables . . . . .	49
5.4	Efficiency for jet energy cut . . . . .	53
5.5	Efficiencies for tracking cuts . . . . .	58
5.6	Comparison of cuts between this analysis and the latest H1 publication . . . . .	61
5.7	Comparison of final data and background events for this analysis and the latest H1 publication . . . . .	61
5.8	Comparison of selection efficiencies for this analysis and the latest H1 publication . . . . .	62
B.1	Description of banks written by the CIP2000 trigger readout . . . . .	92
B.2	Description of files in the CIP2000 trigger readout package . . . . .	93

# Chapter 1

## Introduction

In the last decades the Standard Model of elementary particle interactions has become the accepted theory to describe the experimental results in high energy physics. In this framework matter consists of quarks and leptons as fundamental particles, each of them appearing in three families. Interactions between the particles are based on the strong and electroweak forces and are mediated by the exchange of gauge bosons.

The Standard Model has been tested in many aspects and to some extent with impressive accuracy. Up to now, it has successfully accomplished all extensions to new energy regimes which have been opened for experimental research by upgraded or new accelerators. Nevertheless the Standard Model can not be the final theory of fundamental interactions, since it leaves too many experimental facts unexplained and since it has some basic fundamental problems which have to show up at high energies. The Standard Model contains many free parameters which are not predicted by theory but must be measured experimentally like the particle masses. The explanation why there are exactly three generations of quarks and leptons is missing. The problem, called hierarchy problem, why the electroweak unification happens already at the 100 GeV scale far below the so-called Planck scale, is not solved.

At the ep storage ring HERA the best way to look for deviations of the Standard Model apart from the precise measurement of the inclusive neutral current cross section at high  $x$  and  $Q^2$  are dedicated searches. The experiments at HERA are well suited to test some of the new models since they explore the highest center-of-mass energy available for deep inelastic scattering with a lepton and a quark in the initial state.

The subject of this thesis is the search for excited quarks by investigating the dedicated decay channel of the excited quark decaying into a photon and a jet. The results of the analysis are used to derive an upper limit on the production cross section of the excited quarks.

- **Chapter 2** gives an introduction to the Standard Model of particle physics and gives an overview of different theories extending the physical contents

beyond the Standard Model. The concept of compositeness and excited fermions as the basic theory of this thesis are introduced.

- **Chapter 3** gives an overview of the HERA collider and the H1 detector with detailed descriptions of components important for this thesis.
- **Chapter 4** deals with the different background processes of ep scattering with the same event signature like the signal events.
- **Chapter 5** presents the data samples and selections used in this analysis. The detection of electromagnetic particles, jets and the detection of photons is explained in detail. The final selections are introduced and the final results are derived including a discussion of the errors of the measurements. The results are compared to the recent H1 publication.
- **Chapter 6** presents the calculation of the limits on the cross-section and on the ratio of the coupling constant to the compositeness scale.
- **Chapter 7** summarizes the conclusions and gives an outlook to future analysis. the coupling constant to the compositeness scale.
- **Appendix A** shows the event displays of all data events after the final selection.
- **Appendix B** gives an overview of the new CIP2000 Trigger readout data system and software. Before carrying out this analysis I was involved in the development of this readout system.

# Chapter 2

## The Standard Model and beyond

This chapter gives an introduction to the Standard Model of electroweak and strong interactions and the physics of positron-proton interactions at HERA. Different extensions of the Standard Model are discussed including the model of composite leptons and quarks used and analyzed in this thesis.

### 2.1 Standard Model of electroweak and strong interactions

The Standard Model of particle physics, which has been developed in the second half of the last century has proved very successfully in describing all experimental results in the field of high energy physics. It summarizes the knowledge gained by scientists about the structure of matter today. The following basic assumptions are the basis of the Standard Model. Matter is composed of elementary fermions with spin  $\frac{1}{2}$ , quarks and leptons. Both types we group in three families consisting of two particles. Each of the 12 particles has a corresponding anti-particle with opposite charge but otherwise identical properties.

$$\text{Leptons: } \begin{pmatrix} \nu_e \\ e \end{pmatrix} \begin{pmatrix} \nu_\mu \\ \mu \end{pmatrix} \begin{pmatrix} \nu_\tau \\ \tau \end{pmatrix} \quad \text{Quarks: } \begin{pmatrix} u \\ d \end{pmatrix} \begin{pmatrix} c \\ s \end{pmatrix} \begin{pmatrix} t \\ b \end{pmatrix}$$

These elementary particles are subject to three fundamental forces, which are the strong, the electromagnetic and the weak force. The fourth known fundamental interaction named Gravity has not yet been included in the Standard Model. The interactions between the particles composing matter are mediated by bosons carrying spin 1. These exchange particles are the massless photon for the electromagnetic force, the massive  $Z^0$  and  $W^\pm$  bosons for the weak force and eight massless gluons mediating the strong interaction. The third kind of particle in the Standard Model is the Higgs boson, which is responsible for the creation of particle masses. The electromagnetic and weak force are combined in the Standard Model into the electroweak interaction. The gauge theory describing the

strong interaction is the Quantum Chromodynamics.

The modern experiments in high energy physics to verify the predictions of the Standard Model are based on the same principle, which has already been utilised by Rutherford and his assistants Geiger and Marsden in their experiments revolutionising physics at the start of the 20th century. Aiming alpha particles on a thin gold foil, Rutherford deduced from the rate at which the alpha particles have been scattered at specific angles, that gold atoms must be largely made up of empty space containing a small heavy core, which carries nearly all of the mass and the total positive charge of the gold atom. The atomic nucleus had finally been discovered.

The experimental techniques have grown more complex, but the basic principle of using point-like particles as a probe to investigate another particle that scatters the first has not changed for the recent experiments. Beneath these scattering experiments the investigation of electron-proton interactions has already played an important role in revealing the structure of the proton and establishing Quantum Chromodynamics as the theory of strong interactions. The H1 and ZEUS experiments at the Hadron-Elektron-Ring-Anlage HERA, which is the only accelerator colliding positrons or electrons on high-energetic protons worldwide, provide an unique testing ground for the Standard Model. Although no deviation from the Standard Model has been established, it is widely believed that the Standard Model is incomplete and that new physics signals may appear below energies of 1TeV. A large variety of extensions to the Standard Model has been constructed during the last decades, predicting various phenomena appearing at high energies or large transverse momenta. HERA data have been used to test some of these models of new processes by analysing their anticipated experimental signatures, and limits on their parameters have been derived.

## 2.2 Physics beyond the Standard Model

The Standard  $SU(3) \times SU(2) \times U(1)$  Model of strong, electromagnetic and weak forces is remarkably well confirmed at the phenomenological level over the past quarter of century. But in certain points it remains incomplete and unsatisfactory. First of all, it only offers a partial “unification” of the electroweak and strong forces. Quarks are assumed to carry flavour degrees of freedom and color quantum numbers somehow independently. The electroweak interactions couple only to flavours and are indifferent to colors. The strong interaction of colored quarks and gluons described by the  $SU(3)$  quantum chromodynamics (QCD) gauge field theory remains separate. A “Grand Unification” of carriers of fundamental interactions in, for instance, a larger local gauge theory is simply postponed.

The Standard Model’s predictive power suffers from a large number of arbitrary parameters like the particle masses that have to be measured experimentally. These masses are assumed to originate solely from the electroweak sector. A fundamental scalar field, the Higgs-boson field, is assumed to pervade the universe and to possess, through self-interaction, a non-zero field strength

of  $v = (\sqrt{2}G_F)^{-1/2} \simeq 246$  GeV of the ground state. The non-zero vacuum expectation value induces a breaking of the electroweak  $SU(2)_L \times U(1)_Y$  symmetry down to the electromagnetic  $U(1)_{EM}$  symmetry. This so called ‘‘Higgs mechanism’’ gives masses to the  $W^\pm$  and  $Z$  bosons and leaves the photon massless, but remains experimentally unproven. The mass of the Higgs boson itself is not predicted by the Standard Model but an upper bound must nevertheless be imposed to preserve the internal consistency of the model. It is the Yukawa interactions, of arbitrary strengths, of fermions with the Higgs field that are assumed to be responsible for the fermion masses after electroweak symmetry breaking. In contrast, the local gauge symmetries of the strong interactions remain unbroken at all levels of the theory.

In the Standard Model there are no direct couplings between quark and lepton families and the theory is consistent with a separate and exact conservation of the lepton and baryon numbers in all processes. The viability of the Standard Model rests on an empirical similarity between lepton and quark sectors. Anomalies that would prevent renormalizability of the theory are avoided by an exact cancellation between contributions of lepton and quark fields. No deeper understanding is provided for this exact cancellation, which happens thanks to the special arrangement of fermion multiplets in the model and the fact that quarks have the additional color degree of freedom. At a more fundamental level, the structure of the leptonic and quarkonic sectors could, for instance, imply the existence of new bosonic carriers of lepton and baryon numbers.

The Standard Model incorporates an apparent threefold replica of fermion generations which remain unexplained. The electroweak interaction Lagrangian is constructed separately for each of the lepton and quark generations, with anomalies cancelled within each generation. There are no direct couplings between different lepton families while three quark families (at least) are needed if quark mixing is to be the cause of all observed electroweak CP violation. The existence of the fermion generations could be hinting that more elementary constituents exist which form the known quarks and leptons. The origin of ordinary particle masses remains a mystery, too. It is nevertheless a common belief that an electroweak symmetry breaking mechanism characterized by one (or more) scalar particles is responsible. Such particles could be elementary as in the Standard Model or in supersymmetric theories like Supergravity. Alternatively, the parametrization in terms of scalar couplings may in fact represent a low-energy manifestation of more fundamental dynamics, with additional particles and interactions. This is the underlying assumption of Technicolour or compositeness theories. The following sections give an overview of models designed to extend the Standard Model and to approach its problems.

### 2.2.1 Supersymmetry

The following section gives an overview of the basic concepts of supersymmetry focussing on the particle content and the properties of the Minimal supersymmetric extension of the SM (MSSM). For a detailed description please see [1, 2].

A theory is called supersymmetric if it is invariant under the following supersymmetric transformation  $Q$  which transforms a bosonic state into a fermionic state and vice versa:

$$Q | \text{boson} \rangle = | \text{fermion} \rangle \quad Q | \text{fermion} \rangle = | \text{boson} \rangle \quad (2.1)$$

Stated by the Coleman-Mandula theorem [3] the symmetry has very restricted properties and the operator  $Q$  has to satisfy the following commutation and anticommutation relations:

$$\{ Q, Q^\dagger \} = P^\mu \quad (2.2)$$

$$\{ Q, Q \} = \{ Q^\dagger, Q^\dagger \} = 0 \quad (2.3)$$

$$[P^\mu, Q] = [P^\mu, Q^\dagger] = 0 \quad (2.4)$$

$P^\mu$  is the momentum generator of spacetime translations. The representations of this superalgebra are called supermultiplets. The supermultiplets contain both fermionic and bosonic states called superpartners. In unbroken supersymmetry particles of the same supermultiplet must have the same mass, the same electric charge, the same weak isospin and the same color [4]. In addition, the number of fermionic degrees of freedom and the number of bosonic degrees of freedom in a supermultiplet must be the same.

The simplest supermultiplet satisfying the upper conditions is a so-called matter or chiral supermultiplet as a combination of a two-component Weyl fermion and a complex scalar field. The next simplest case of a supermultiplet is the so-called gauge supermultiplet containing a vector boson with spin 1 which is massless before spontaneous symmetry breaking and a Weyl fermion. A supersymmetric model with only gauge and chiral multiplets is called “N=1 supersymmetry”.

In the Minimal Supersymmetric Standard Model (MSSM) each of the known particles must be arranged in either a chiral or gauge supermultiplet. The left-handed and right-handed SM fermions (quarks and leptons) are Weyl fermions. They are arranged in a chiral supermultiplet. Each fermion has its own complex scalar partner, called the squarks and sleptons respectively. They are denoted with a tilde. For squarks and sleptons the handedness does not refer to the helicity of the squark or slepton, which are scalar, but to the helicity of the corresponding superpartners (quarks and leptons). The scalar Higgs boson must be a member of a chiral supermultiplet since it has a spin of 0. One Higgs chiral supermultiplet with  $Y = \frac{1}{2}$ , which gives masses to up-type quarks (u, c, t), called  $H_u$ , and one Higgs chiral supermultiplet with  $Y = -\frac{1}{2}$ , which gives masses to down-type quarks (d, s, b) and to charged leptons (e,  $\mu$ ,  $\tau$ ), called  $H_d$ , are introduced. The particle content of all chiral supermultiplets is given in Table 2.1.

Name		Spin 0	Spin $\frac{1}{2}$
squarks, quarks (in 3 generations)	$Q$	$(\tilde{u}_L \tilde{d}_L)$	$(u_L d_L)$
	$U$	$\tilde{u}_R^*$	$u_R^\dagger$
	$D$	$\tilde{d}_R^*$	$d_R^\dagger$
sleptons, leptons (in 3 generations)	$L$	$(\tilde{\nu}_L \tilde{e}_L)$	$(\nu_L e_L)$
	$E$	$\tilde{e}_R^*$	$e_R^\dagger$
Higgs, higgsinos	$H_u$	$(H_u^+ H_u^0)$	$(\tilde{H}_u^+ \tilde{H}_u^0)$
	$H_d$	$(H_d^0 H_d^-)$	$(\tilde{H}_d^0 \tilde{H}_d^-)$

Table 2.1: *Chiral supermultiplets in the MSSM.*

The vector bosons of the SM are members of a gauge supermultiplet. Their superpartners are called gauginos, which are denoted by a tilde. The partner of the spin 1  $SU(3)_C$  gauge boson, the gluon is the gluino which has spin  $\frac{1}{2}$ . The  $SU(2)_L \times U(1)_Y$  gauge bosons of the SM are  $W^\pm$ ,  $W^0$  and  $B^0$ . Their spin  $\frac{1}{2}$  partners are called wino and bino. The particle content of all gauge supermultiplets is given in Table 2.2. As in the SM  $W^0$  and  $B^0$  gauge eigenstates mix to form mass eigenstates  $Z^0$  and  $\gamma$ . The corresponding mixtures of  $\tilde{W}^0$  and  $\tilde{B}^0$  are called zino ( $\tilde{Z}^0$ ) and the photino ( $\tilde{\gamma}$ ).

Name	Spin $\frac{1}{2}$	Spin 1
gluino, gluon	$\tilde{g}$	$g$
winos, W bosons	$\tilde{W}^\pm \tilde{W}^0$	$W^\pm W^0$
bino, B boson	$\tilde{B}^0$	$B^0$

Table 2.2: *Gauge supermultiplets in the MSSM.*

Because of the electroweak symmetry breaking effects, the superpartners listed above are not necessarily the mass eigenstates of the theory. Mixing can appear between electroweak gauginos and the higgsinos, and between the various squarks and sleptons and the Higgs scalars which have the same electric charge. The neutral states, the two neutral gauginos ( $\tilde{B}^0$ ,  $\tilde{W}^0$ ) and the two neutral higgsinos ( $\tilde{H}_u^0$ ,  $\tilde{H}_d^0$ ), combine to form the four neutral mass eigenstates which are called neutralinos ( $\chi_i^0$ ). The charged states, the two winos ( $\tilde{W}^-$ ,  $\tilde{W}^+$ ) and the two charged higgsinos ( $\tilde{H}_u^+$ ,  $\tilde{H}_d^-$ ) mix to form the two mass eigenstates with charge  $\pm 1$  which are called charginos ( $\chi_i^\pm$ ). Different arguments encourage the development of the supersymmetry theories:

- The natural value of the Higgs mass of about  $10^{14} - 10^{17}$  GeV is not around

the electroweak scale as suggested by precise electroweak data. This hierarchy problem could be solved by the supersymmetry theory.

- The SUSY particles contribute to the different couplings of the strong, weak and electromagnetic interactions above the effective SUSY scale of about 1 TeV, which causes a change in the slope in the evolution of the couplings where they could unify in the above 15 TeV region.
- If supersymmetry is embedded in a grand unified theory and the unifications of the coupling constants is assumed, it makes a very precise prediction of the electroweak mixing parameter  $\sin^2 \theta_W$  which has been confirmed at LEP at the per mill level.
- In supersymmetric models the electroweak symmetry breaking is a natural result of renormalisation group evolution.
- If supersymmetry is formulated as a local symmetry, it naturally incorporates gravity since a field of spin 2 must be introduced, which can be identified as the graviton.

### 2.2.2 GUT

The philosophy of the Grand Unification Theory (GUT) is to find a simple gauge group that includes the  $SU(3)$ ,  $SU(2)$  and  $U(1)$  gauge groups of the QCD and electroweak sector of the SM.

As a first approximation in the most models gravity is neglected. The three low-energy gauge couplings of the different forces are independent arbitrary parameters. The simplest GUT theory embeds the SM gauge group into the simple unified gauge group, Georgi-Glashow  $SU(5)$ , with one universal gauge coupling  $\alpha_G$  defined at the grand unification scale  $M_G$  [5]. The three low energy gauge couplings are now determined in terms of the two independent parameters  $\alpha_G$  and  $M_G$ . In order to break the electroweak symmetry at the weak scale and give mass to quarks and leptons, Higgs doublets are needed. The additional 3 states are color triplet Higgs scalars. The couplings of these color triplets violate baryon and lepton number, and nucleons decay via the exchange of a single color triplet Higgs scalar. In order not to violently disagree with the non-observation of nucleon decay, their mass would have to be greater than  $\sim 10^{10} - 10^{11}$  GeV. A complete unification is possible with the symmetry group  $SO(10)$  with one universal gauge coupling  $\alpha_G$  and one family of quarks and leptons in a 16-dimensional spinor representation. Even larger symmetry groups have been considered like the  $E(6)$  or  $SU(6)$  groups.

A combination of supersymmetric models and GUT theory is one of the most promising theories beyond the SM that is probed at current and future accelerators.

## 2.3 Compositeness and Excited Quarks

The family structure and the pattern of the masses of leptons and quarks are not explained by the Standard Model. Models of composite leptons and quarks were introduced in an attempt to provide an explanation. A natural consequence of these models is the existence of excited states of leptons and quarks.

It is often assumed that the compositeness scale for excited fermions is in the TeV region, which would give excited fermion masses in the same energy region. With the dynamics at the constituent level being unknown, the lowest excitation states of the fermions could possibly have masses in the order of a few hundred GeV. Positron-Proton interactions at very high energies provide an excellent environment to look for the excited fermions of the first generation.

Excited fermions can carry different spin and isospin assignments [6]. In some models quarks and leptons are composites of a scalar and a spin  $\frac{1}{2}$  constituent and the lowest lying excitations have spin  $\frac{1}{2}$ . Given that the lowest spin states are often considered as the most probable a model in which excited fermions are assumed to have spin  $\frac{1}{2}$  and isospin  $\frac{1}{2}$  is chosen. The interaction between the excited fermionic particles  $f^*$ , the gauge bosons and the ordinary fermionic matter  $f$  is described by an effective Lagrangian. Both left-handed and right-handed components of the excited fermions form weak isodoublets  $F_L^*$  and  $F_R^*$ . Couplings of excited fermions to ordinary fermions of both chiralities should be avoided in order to protect the light leptons from radiatively acquiring a large anomalous magnetic moment [7, 8]. It is chosen to consider couplings to left-handed fermions only, in which case only the right-handed component of the excited fermions takes part in the following magnetic-moment type Lagrangian:

$$\mathcal{L}_{eff} = \frac{1}{2\Lambda} \bar{F}_R^* \sigma^{\mu\nu} \left[ g f \frac{\tau^a}{2} W_{\mu\nu}^a + g' f' \frac{Y}{2} B_{\mu\nu} + g_s f_s \frac{\lambda^a}{2} G_{\mu\nu}^a \right] F_L + h.c. \quad (2.5)$$

$W_{\mu\nu}^a$ ,  $B_{\mu\nu}$  and  $G_{\mu\nu}^a$  are the field-strength tensors of the SU(2), U(1) and SU(3) gauge fields.  $\tau^a$ ,  $Y$  and  $\lambda^a$  are the Pauli matrices, the weak hypercharge operator and the Gell-Mann matrices. The  $g$ ,  $g'$  and the  $g_s$  are the standard electroweak and the strong gauge couplings.  $\Lambda$  is the compositeness scale while  $f$ ,  $f'$  and  $f_s$  can be viewed as form factor parameters to allow the composite fermion to couple with an arbitrary strength to the three different gauge groups. The coupling constants of the  $f^*$  with the boson and the fermion  $f$  are related to the parameters  $f$  and  $f'$ . The coupling constants for the different bosons are:

$$c_{\gamma f^* f} = \frac{1}{2} \left( f I_3 + f' \frac{Y}{2} \right) \quad (2.6)$$

$$c_{Z f^* f} = \frac{1}{2} \left( f I_3 \cot \theta_W - f' \frac{Y}{2} \tan \theta_W \right) \quad (2.7)$$

$$c_{W^* f} = \frac{f}{2\sqrt{2} \sin \theta_W} \quad (2.8)$$

$I_3$  is the third component of the isospin of the fermion and  $\theta_W$  is the Weinberg angle. The partial width [9, 10] for the various electroweak decay channels of an excited fermion  $f^*$  in a fermion  $f$  and a real boson  $V$  are given as:

$$\Gamma(f^* \rightarrow f V) = \alpha \frac{M_{f^*}^3}{\Lambda^2} c_{Vf^*f}^2 \left(1 - \frac{M_V^2}{M_{f^*}^2}\right)^2 \left(1 + \frac{M_V^2}{2M_{f^*}^2}\right) \quad (2.9)$$

$M_{f^*}$  is the mass of the excited fermion,  $M_V$  the mass of the electroweak boson and  $\alpha$  the fine structure constant. The partial width for excited quarks decaying into a quark and a gluon is given as:

$$\Gamma(f^* \rightarrow f g) = \frac{4}{3} \alpha_s \frac{M_{f^*}^3}{\Lambda^2} \left(\frac{1}{2} f_s\right)^2 \left(1 - \frac{M_V^2}{M_{f^*}^2}\right)^2 \left(1 + \frac{M_V^2}{2M_{f^*}^2}\right) \quad (2.10)$$

For  $M_{f^*}$  values between 50 to 250 GeV and  $\Lambda = M_{f^*}$ , the intrinsic widths of the excited fermions are typically of the order of some hundred MeV for excited electrons and  $f$  and  $f'$  values  $\simeq 1$  while for excited quarks the width varies between 1 GeV to  $\simeq 10$  GeV with  $f_s \simeq 1$ .

Figure 2.1 shows the leading diagram for the production and decay of excited quarks in ep collisions. In this analysis only the decay channel into a photon and a jet is investigated because the signature of this decay can be detected in the H1 detector very well.

Figure 2.2 shows the photon-jet signature of a typical signal event in the H1 detector. The photon is detected in the electronic part of the Liquid Argon Calorimeter and has no track pointing to its cluster. The jet is seen as the accumulation of connected clusters in the electronic and hadronic part of the Liquid Argon Calorimeter. In most cases the scattered positron is not seen in the detector. Detailed information on the detector components can be found in the following Chapter 3. In Chapter 4 the typical photon-jet signal signature is compared to the signatures of possible background processes.

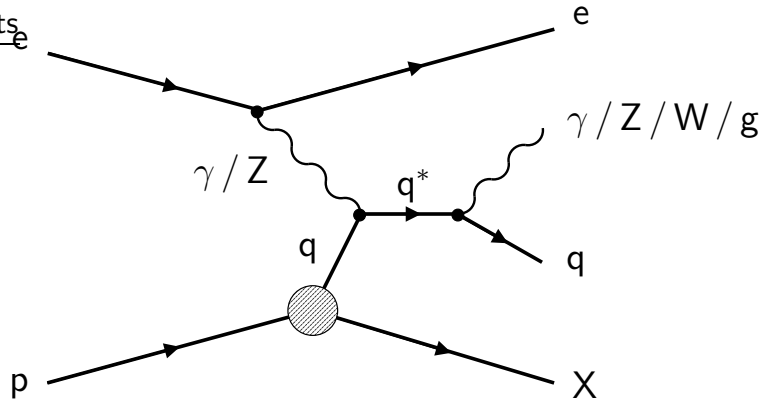


Figure 2.1: *Leading diagram for the production and decay of excited quarks in ep collisions*

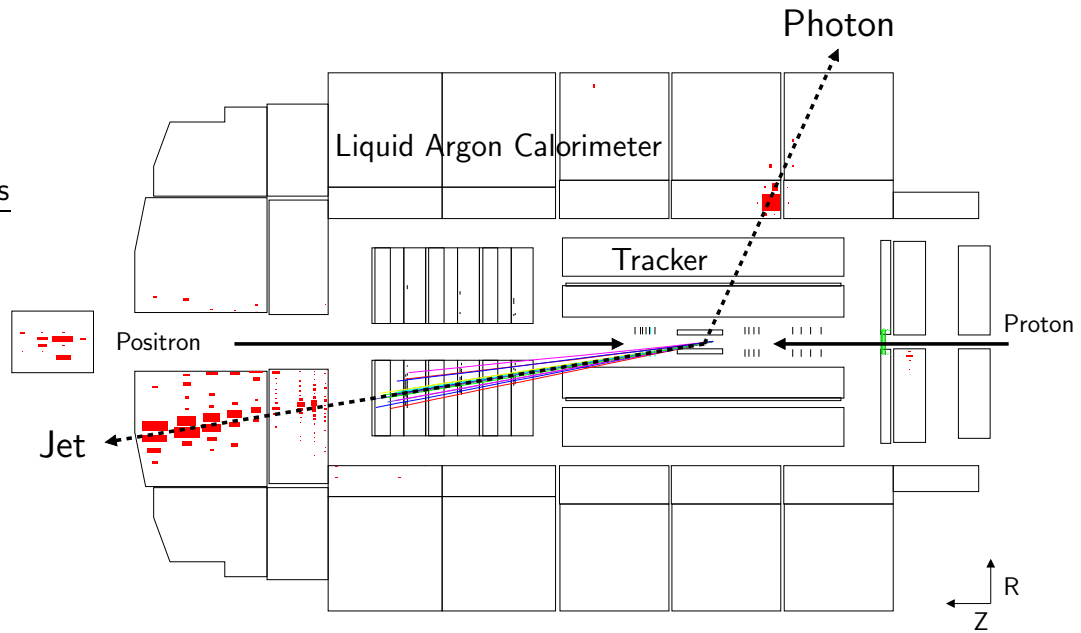


Figure 2.2: *Detector signature for the decay of an excited quark into a jet and a photon. The photon is detected in the electronic part of the Liquid Argon Calorimeter and has no track pointing to its cluster. The jet is seen as the accumulation of connected clusters in the electronic and hadronic part of the Liquid Argon Calorimeter.*

# Chapter 3

## HERA and the H1 Detector

The analysis of this thesis is based on data taken with the H1 detector at the HERA ep collider in the years 1999-2000. This chapter describes the HERA collider and the detector components of the H1 experiment which are relevant for this thesis.

### 3.1 The HERA Collider

Two independent machines reside in the 6.4 km long tunnel some 15 m below the surface. One is an positron (alternatively electron) storage ring, which accelerates the particles from an initial 14 GeV to 30 GeV. The proton machine starts with initial 40 GeV protons which are accelerated to 920 GeV before a collision with the positrons or a target is forced. The energy of the proton beam is limited by the strength of the magnets needed to bend the beam on its orbit. The HERA proton ring consists of superconducting magnets which produce a field of 4.6 T.

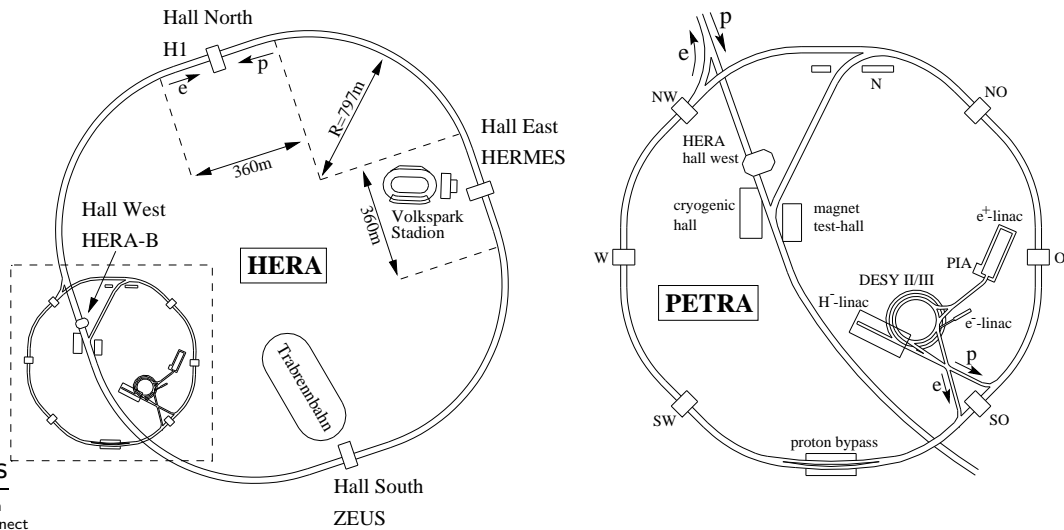


Figure 3.1: HERA storage ring with pre-accelerators PETRA, DESY and Linacs.

Figure 3.1 gives an overview of HERA and its injector chains. The particles are packed into a maximum of 210 bunches, with a bunch crossing distance of only 96 ns. Not all of the bunches are filled with particles. The bunch crossings with no interactions are used to investigate beam induced background. The currents of the beams have been successfully increased in the last years. At the moment four experiments use the HERA storage ring. H1 and ZEUS are built around two interaction regions of the storage rings. The HERMES detector records the scattering of the polarized positron beam on polarized gas targets. The HERA-B experiment was built to measure  $CP$  violation in  $B^0 - \bar{B}^0$  systems generated by collisions of beam protons with a wire target. The experiment stopped data taking in the end of 2003.

During the data taking period 1999-2000, HERA was operated with a center-of-mass energy of  $\sqrt{s} \approx 319$  GeV. With typical positron currents of 40 mA and proton currents of 90 mA a peak luminosity of about  $1.5 \times 10^{31} \text{ cm}^{-2}\text{s}^{-1}$  has been achieved which corresponds to the design value of HERA. Figure 3.2 shows the annual integrated luminosity provided by HERA since 1992 and the luminosity accumulated by H1. The H1 experiment has recorded data corresponding to an integrated luminosity of about  $120 \text{ pb}^{-1}$  in the years 1992 to 2000. In September 2000 the HERA operation was shut down to allow for a major luminosity upgrade of the HERA machine and the detectors. More information on the luminosity upgrade can be found in the appendix.

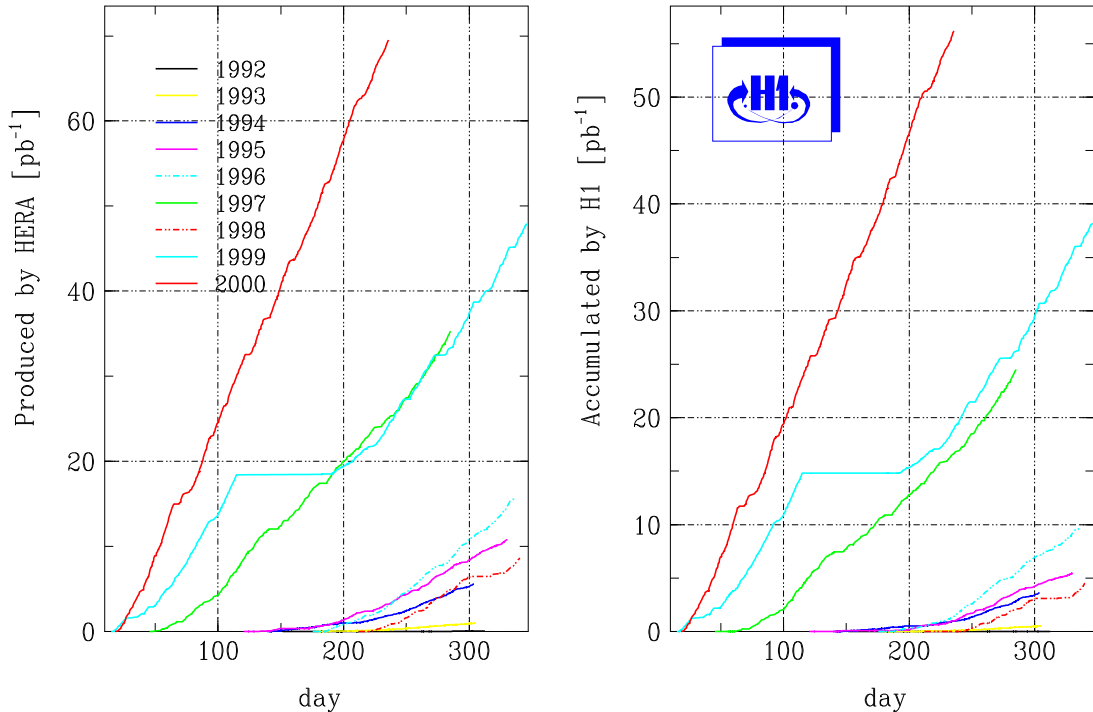


Figure 3.2: Annual integrated luminosity as function of time. The figure on the left shows the integrated luminosity provided by HERA. The right figure shows the integrated luminosity accumulated by the H1 experiment.

## 3.2 The H1 detector

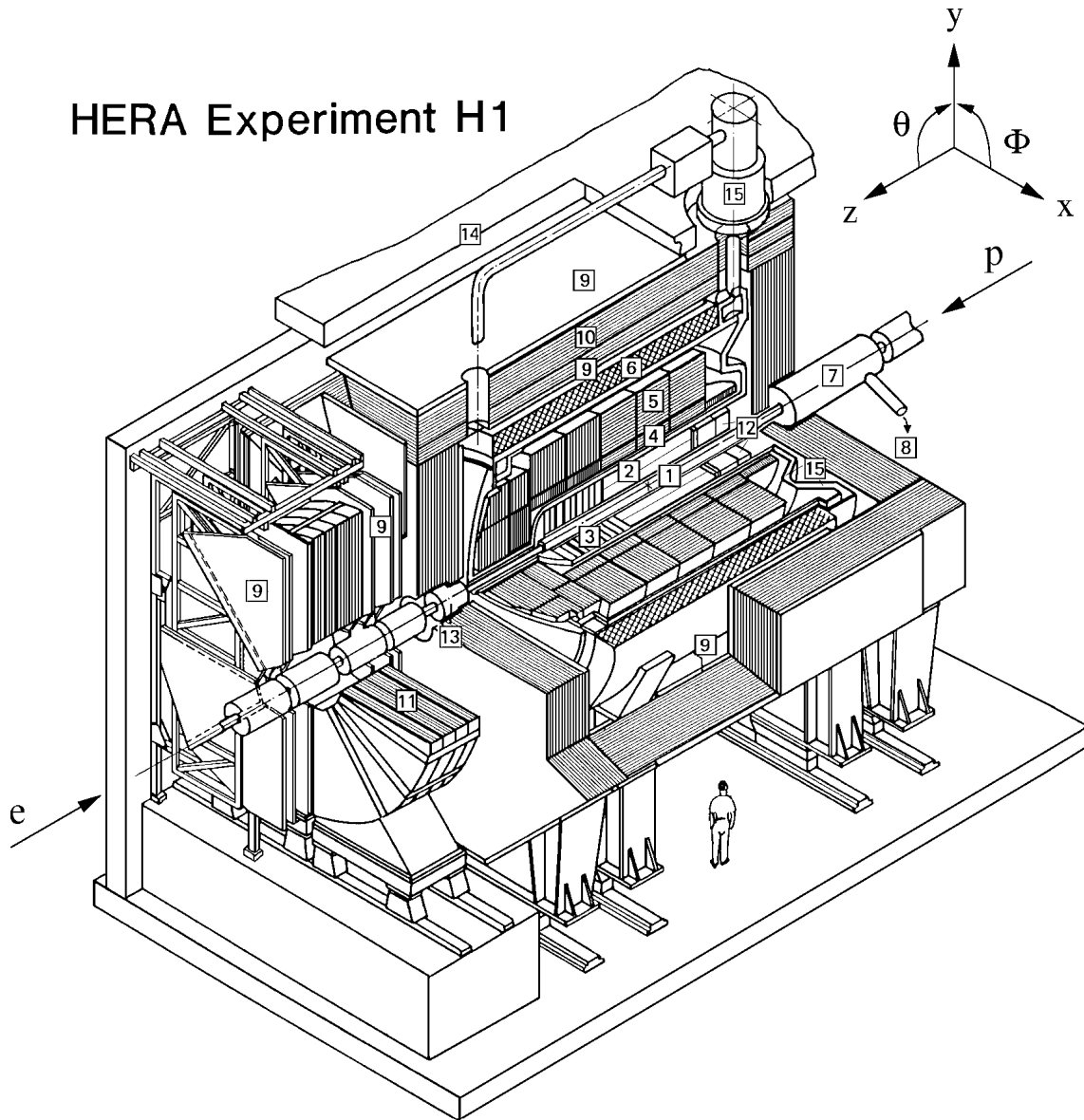
The H1 detector is located at the north interaction region of HERA. Figure 3.3 shows a schematic overview including the standard coordinate system. The detector is described in detail in [11, 12]. It was designed as a multi-purpose detector on the basis of the HERA physics program, which includes the precise measurement of the proton structure, tests of the Standard Model and searches for new physics. The detector measures the energy and direction of particles emerging from the ep interactions. Emphasis is placed on accurate lepton identification as well as on the high granularity and resolution for the measurement of hadronic jets. To allow for the recognition of missing transverse energy, the detector provides almost hermetic coverage of the solid angle of  $4\pi$  with some unavoidable losses due to the feed through of the beam pipe.

The standard H1 coordinate system is defined as a Cartesian coordinate system with the origin placed at the geometrical center of the central tracking chambers defining the nominal interaction point. The z-axis points in the proton beam direction, the y-axis points vertically upwards and the x-y plane is referred to as the transverse plane. The forward and backward directions denote the regions of  $z > 0$  and  $z < 0$  respectively. The polar angle  $\theta$  is measured with respect to the proton beam direction and the azimuthal angle  $\phi$  is defined with respect to the positive x-axis.

Due to the different beam momenta and the corresponding strong boost into the proton direction in the ep center-of-mass system, the design of the detector is asymmetric with respect to the interaction point. The individual detector components are mounted concentrically around the beam line with an enhanced instrumentation in the forward direction.

The interaction region is covered by silicon detectors in the central and backward direction to improve the quality of the measurement of particle tracks and to detect secondary vertices. The silicon detectors are surrounded by the central and forward tracking detectors measuring the trajectories and momenta of charged particles. The tracking system is enclosed in a large calorimeter system which consists of the Liquid Argon calorimeter (LAr) in the central and forward direction and is supplemented in the backward region by a Spaghetti calorimeter (SpaCal). The calorimeters are divided into an electromagnetic and a hadronic section measuring the position and energies of charged and neutral particles. This separation allows a good identification of positrons. The Liquid Argon calorimeter is surrounded by a superconducting cylindrical coil which provides a homogeneous magnetic field of 1.15 T parallel to the beam axis. The field lines are closed by the iron return yoke which is instrumented with streamer tubes to detect muons and to measure the energy leakage from hadrons not fully contained in the calorimeters. The forward muon detector consists of drift chambers and a toroidal magnet to identify and measure the momentum of penetrating muons in the forward direction. The luminosity system is placed in the negative z-direction close to the beam pipe. In the following only the components important for the present analysis are described in more detail.

# HERA Experiment H1



- |   |                                 |    |                        |
|---|---------------------------------|----|------------------------|
| 1 | Beam pipe and beam magnets      | 9  | Muon chambers          |
| 2 | Central tracker                 | 10 | Instrumented iron yoke |
| 3 | Forward tracker                 | 11 | Forward muon toroid    |
| 4 | Electromagnetic LAr calorimeter | 12 | Backward calorimeter   |
| 5 | Hadronic LAr calorimeter        | 13 | PLUG calorimeter       |
| 6 | Superconducting coil            | 14 | Concrete shielding     |
| 7 | Compensating magnet             | 15 | Liquid Argon cryostat  |
| 8 | Helium cryogenics               |    |                        |

Figure 3.3: Schematic overview of the H1 detector. The H1 coordinate system is indicated in the top right corner.

### 3.2.1 Calorimeters

The calorimetric information of an event plays a key role in this analysis. It is used to identify the scattered positron, photons and all hadronic final states. The main calorimeters are the Liquid Argon (LAr) calorimeter and the Spaghetti Calorimeter (SpaCal). Together they cover almost the whole solid angle around the interaction region. The plug calorimeter covering the very forward region between the LAr calorimeter and the beam pipe is not used in this analysis.

#### LAr - Liquid Argon Calorimeter

The LAr calorimeter covers the polar angle range of  $4^\circ \leq \theta \lesssim 154^\circ$ . It is housed in a single cryostat and surrounded by a superconducting solenoid. The LAr calorimeter is a sampling calorimeter which consist of an inner, fine grained electromagnetic section and an outer coarser grained hadronic part. Figure 3.4 shows a vertical cut through the calorimeter along the beam axis. It is divided into eight self-supporting wheels along the z-direction. The different parts are namend according to their position with respect to the proton beam: Backward Barrel (BBE), Central Barrel (CB1, CB2, CB3), Forward Barrel (FB1, FB2),

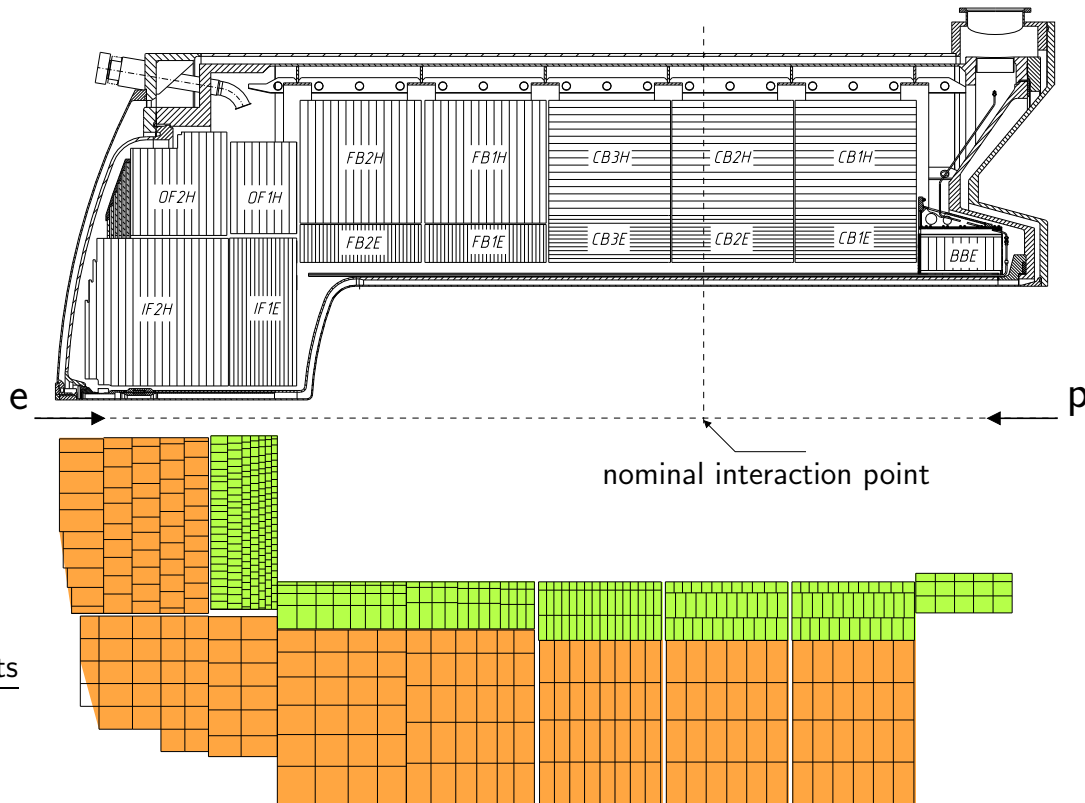


Figure 3.4: *Longitudinal cut through the LAr calorimeter. The upper part shows the sampling structure and the lower part shows the readout structure of the calorimeter.*

Outer Forward (OF) and Inner Forward (IF). The OF just consists of two hadronic sections and the IF just consists of an electromagnetic section. Figure 3.5 shows the segmentation of the calorimeter in the  $\phi$  direction. Each wheel is divided into eight identical units, the so-called octants with their typical octagon structure. In the BBE the structure of the octants is bent at the edges leading to a 16-fold polygonal surface of the calorimeter front. The insensitive areas at the connecting points of the modules are called “z-cracks” between the wheels and “ $\phi$ -cracks” between the octants.

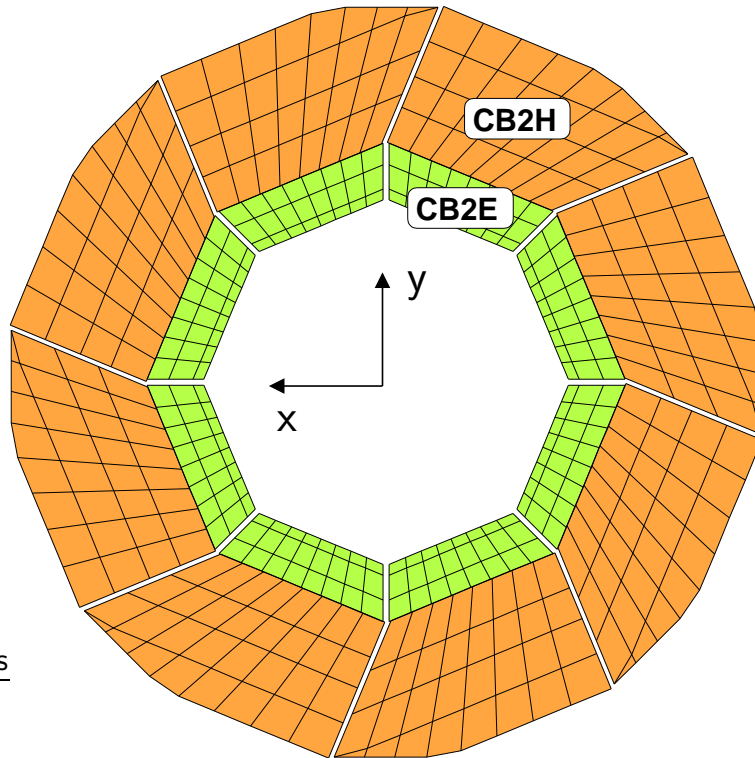


Figure 3.5: *Transverse cut through a central barrel (CB2) of the LAr calorimeter viewed along the proton beam direction.*

The LAr calorimeter is built of absorber plates supplemented by high voltage and read-out electrodes. The interspaces between the plates are filled with liquid Argon as an active medium. The orientation of the plates is arranged such that the angle of incidence of particles originating from the nominal interaction point is always larger than  $45^\circ$ . The absorber plates in the electromagnetic section consist of 2.4 mm lead with gaps filled with liquid argon with an average thickness of 2.35 mm. This leads to an absorption length of 20 radiation lengths ( $X_0$ ) in the central to 30 radiation lengths in the forward direction. The absorber material in the hadronic section consists of 19 mm thick stainless steel plates with a double gap of 2.4 mm filled with liquid Argon. The total amount of absorbing material of the calorimeter corresponds to about 5 to 8 hadronic interaction lengths ( $\lambda$ ). The calorimeter is further segmented into about 44000 read-out cells to enable a

good spatial resolution of deposited energies. The segmentation is coarse in the backward part and becomes finer towards the forward direction. Seen from the nominal interaction point, the number of layers increases from three to six in the electromagnetic section and from four to six in the hadronic section. Due to the fine granularity it is possible to measure precisely the position of electromagnetically interacting particles and to separate electromagnetic and hadronic showers. The energy measurement in the LAr calorimeter relies on the absorption of the total energy of the primary particle by a cascade of secondary particles. Part of the energy is deposited in the LAr gaps by ionisation (about 10% for electromagnetic showers). The charge is collected by charge sensitive amplifiers from the read-out pads. Calibration constants were derived from test beam measurements for each cell geometry to convert the measured charge into energy units. The electronic noise contribution depends linearly on the capacitance of the complete read-out chain which is mainly given by the cell size. The noise for a single cell would amount to an equivalent energy of about 10 to 30 MeV. Noise suppression algorithms are applied and reduce the noise contribution to a large extent without significant effects on the real energy measurements. Further correction factors entering the charge to energy conversion are: the charge collection efficiency at nominal high voltage operation (measured from high voltage curves using cosmic or halo muons) and corrections for local variations of the size of cracks or absorbers derived from Monte Carlo simulations. The energy reconstruction combines different groups of cells to so-called clusters which approximately correspond to the energy deposition of single particles.

The LAr calorimeter is non-compensating. The deposited charge for hadrons is smaller than for positrons of the same energy. The signal ratio of positrons to pions ( $e/\pi$  ratio) is about 1.35 for 10 GeV particles and decreases logarithmically with energy. Therefore large  $\pi^0$  fluctuations in hadronic showers yield a non-linear energy response and significant non-Gaussian contributions to the energy measurement. This effect is compensated by a software energy weighting technique. The method of the reweighting relies on the fine segmentation of the LAr calorimeter which allows to identify the electromagnetic components within hadronic showers.

The energy resolution of the LAr calorimeter was measured with test beams at CERN. The energy resolution for positrons and photons is:

$$\sigma_{em}(E)/E = 12\%/\sqrt{E[GeV]} \oplus 1\% \quad (3.1)$$

The energy resolution for charged hadrons is:

$$\sigma_{had}(E)/E = 50\%/\sqrt{E[GeV]} \oplus 2\% \quad (3.2)$$

## SpaCal - Spaghetti Calorimeter

The Spaghetti calorimeter (SpaCal) covers the polar angle range of  $153^\circ \leq \theta \leq 177.5^\circ$  and therefore supplements the calorimetric measurement in the backward region. The SpaCal is a sampling calorimeter made of lead as the absorber material and scintillating fibres as the active components. The light produced in the scintillating fibres by charged particles is collected and read out by photomultiplier tubes. The SpaCal is divided into an electromagnetic and a hadronic section. The electromagnetic section consists of 1192 cells of transverse size of  $40.5 \times 40.5 \text{ mm}^2$  and is made of 0.5 mm diameter scintillating plastic fibres with a lead-to-fibre volume ratio of 2.3:1 providing a spatial resolution of a few millimeters. The electromagnetic energy resolution was measured in test beam measurements to be:  $\sigma_{em}(E)/E = 7\%/\sqrt{E[\text{GeV}]} \oplus 1\%$ . The absolute energy scale is known to a precision of 1.0%.

The hadronic section consists of 136 cells of the size  $119 \times 119 \text{ mm}^2$  and is made of 1.0 mm diameter scintillating plastic fibres with a lead-to-fibre volume ratio of 3.4:1. In total, the SpaCal is two interaction lengths deep. It provides a coarse hadronic energy measurement and a precise time information which is used on the first trigger level to suppress background events.

## Tail Catcher Calorimeter

The iron yoke of the main solenoid surrounds all major detector components and serves as a hadronic tail catcher, measuring hadronic energy leaking out of the LAr and SpaCal calorimeters, and for the measurement of penetrating muons. The iron system consists of ten iron layers (7.5 cm thick) which are instrumented with a total of 16 layers of limited streamer tubes. Five layers are equipped with strip electrodes running perpendicular to the wires. The spatial resolution of tracks measured by this unit is of the order of 5-15 mm. The detector is subdivided into the forward endcap, the barrel and the backward endcap, which cover different polar angle regions and have different orientations of the wires and strips.

To measure the hadronic energy leaking out of the main calorimeter, eleven layers of the instrumented iron are equipped with read-out pad electrodes, which have the typical size of  $40 \times 50 \text{ cm}^2$  in the barrel part and  $28 \times 28 \text{ cm}^2$  in the endcaps. The energy measurement is based on the analog read-out of the pad signals of five consecutive inner and six outer pads providing a two-fold energy sampling in depth. The main energy contributions of the tail catcher to the total calorimetric energy measurement comes from the directions close to the beam and from the transition region between the LAr and SpaCal calorimeter. The energy resolution was measured in a test beam measurement and is to be:  $\sigma_{em}(E)/E = 100\%/\sqrt{E[\text{GeV}]}$ .

### 3.2.2 Tracking System

The tracking system of the H1 detector is designed to measure the momenta and angles of charged particles and to provide fast trigger signals. The trajectories of particles are derived from signals of different sub-detectors. The momenta are obtained from the curvature of the tracks within the magnetic field of the superconducting solenoid magnet. Figure 3.6 shows the different sub-detectors of the inner tracking system. The tracker is divided into central and forward tracking devices. The backward drift chamber (BDC) is not used in this analysis.

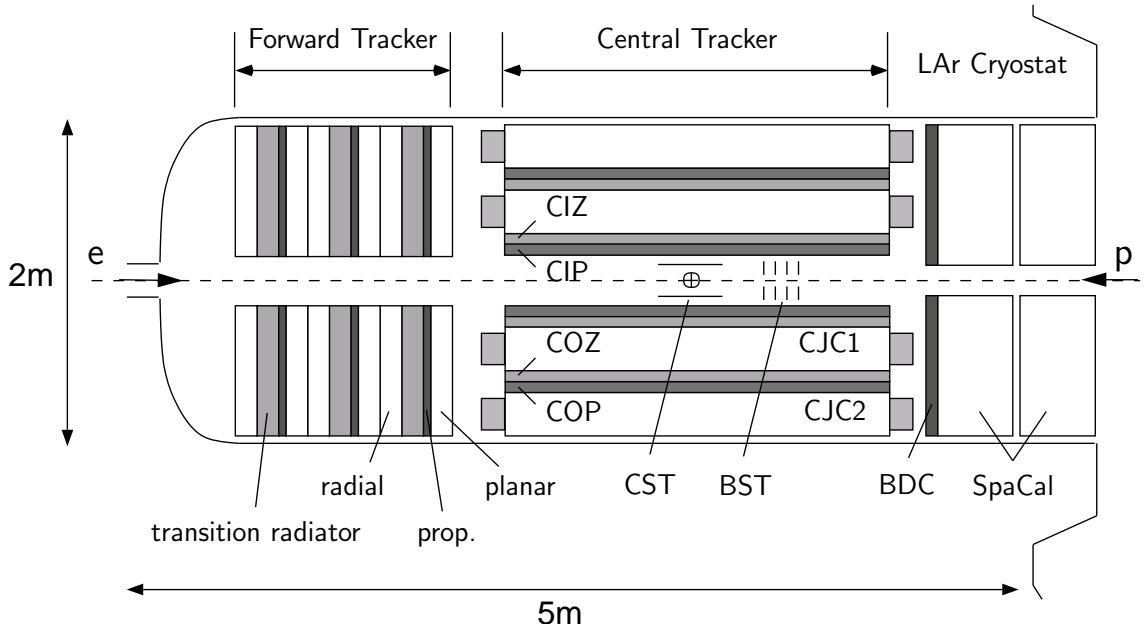


Figure 3.6: Longitudinal cut through the H1 tracking system.

#### Central tracking chambers

The central tracking detector covers the angular range of  $15^\circ \leq \theta \leq 165^\circ$  with a full azimuthal acceptance. Figure 3.7 shows the transverse cut through the central tracking chambers which are mounted concentrically around the beam pipe. The most inner part is the Central silicon tracker (CST) not shown in the figure. It consists of two detector layers and was built to provide vertex information from precision measurements of charged particle tracks close to the interaction point. The central inner and outer multi-wire proportional chambers (CIP and COP) are used to deliver fast timing signals with time difference between HERA bunch crossings to derive first trigger level decisions based on tracks of charged particles. The primary components of the tracking system are the two jet-type chambers CJC1 and CJC2. They measure the  $r$ - $\phi$ -coordinate of the particle tracks with a precision of  $\sigma_{r\phi} \approx 170 \mu\text{m}$ . The  $z$ -coordinate is measured by comparing the collected charge on the two ends of the wires, resulting in a resolution of  $\sigma_z \approx 2.5 \text{ cm}$ . A much better precision of  $\sigma_z \approx 400 \mu\text{m}$  can be achieved with the

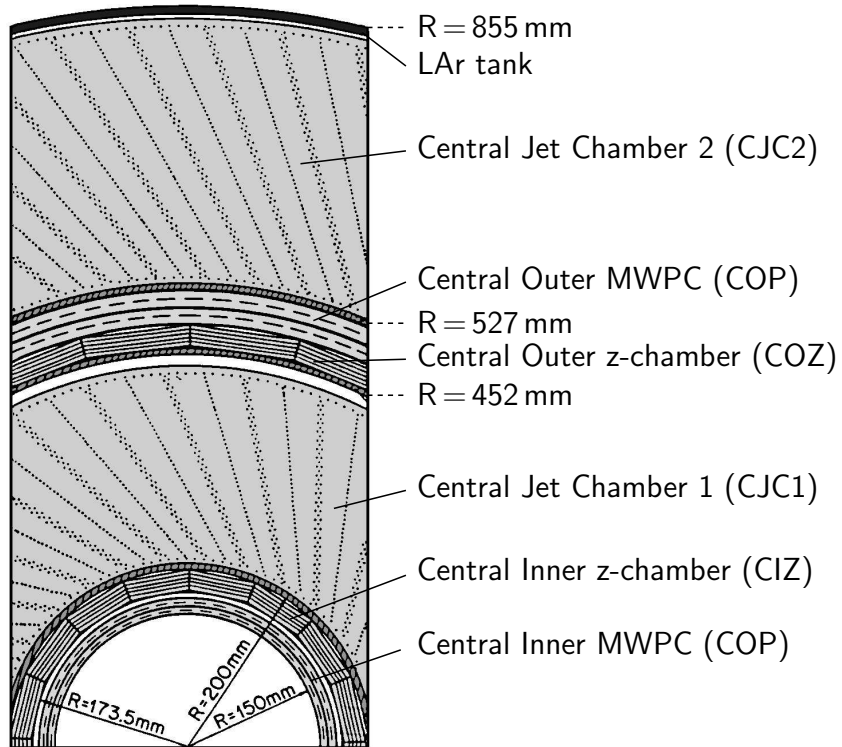


Figure 3.7: *Transvers cut through the central tracking chambers.*

assistance of the z-chambers CIZ and COZ. These chambers are equipped with wires perpendicular to the beam axis. The tracking system achieves a momentum resolution of  $\sigma(p_T)/p_T \approx 0.008 \cdot p_T$  [GeV] in the coordinate transverse to the magnetic field.

### Forward tracking chambers

The forward tracking system extends the polar angle coverage of the central tracking system down to  $\theta \approx 7^\circ$ . It consists of three identical super-modules, each containing three planes of planar drift chambers (each rotated by  $60^\circ$  against each other), a multi-wire proportional chamber, a transition radiator detector and a radial drift chamber.

### 3.2.3 Time-of-Flight detectors

The Time-of-Flight (ToF) system is used to reject proton beam induced background. This background yield a large contribution to the non-ep background when the beam interacts with residual gas inside the beam pipe or with the beam pipe wall itself. The ToF system consist of several scintillator arrays located in the backward region of the H1 detector. They provide precise time information of

traversing particles. Based on the detailed known time structure of ep collisions non-ep events can be rejected by filtering out certain time windows. The precise time resolution of the SpaCal calorimeter provides additional time information which is used in an analogous way as the ToF system.

### 3.2.4 Luminosity Measurement

The instantaneous luminosity  $\mathcal{L}$  connects the interaction rate  $dN/dt$  with the cross section  $\sigma$  of a given process:

$$\frac{dN}{dt} = \mathcal{L} \cdot \sigma \quad (3.3)$$

The total number of events is related to the integrated luminosity  $L = \int \mathcal{L} dt$ , which is given in units of inverse picobarn ( $pb^{-1}$ ). The measurement of the integrated luminosity and the number of events allows the determination of a cross section. The cross section of the Bethe-Heitler process of small angle bremsstrahlung,  $ep \rightarrow e'\gamma p$  is calculable to high precision and diverges for photons radiated collinear to the positron. Therefore it is used at H1 to measure the luminosity. The large cross section enables a precise measurement of the event rate and thus of the luminosity. The luminosity system of the H1 experiment consists of the electron tagger (ET) located at  $z_{ET} = -33.4$  m and the photon detector (PD) located at  $z_{PD} = -102.9$  m. Both detectors are segmented crystal Cerenkov counters with high radiation resistance and good energy, coordinate and time resolution. The scattered positron from the Bethe-Heitler process, which has a reduced momentum compared to the beam positrons, is deflected by a magnet system and measured in the electron tagger. The photon is predominantly scattered under small angles and leaves the upwards bent proton beam pipe before hitting the photon detector. The photon detector is shielded from synchrotron radiation by a lead filter. A water Cerenkov veto counter (VC) recognises and rejects events with photons interacting with the lead absorber. The positron and photon detectors are permanently calibrated during data taking constraining the energy sum  $E_{ET} + E_{PD}$  to the beam energy  $E_e$ . The systematic uncertainty of the luminosity measurement is typically of the order of 1%.

## 3.3 The H1 Trigger and Data Acquisition

Due to the low cross sections of ep interactions, the rate of genuine events is much smaller than the rates for background processes. Typical background sources are collisions between beam protons and rest gas in the vacuum pipes, scattering of off-momentum protons or positrons on beam apertures, collisions of protons between bunches (satellites) due to incorrect pre-acceleration or scattered synchrotron radiation from the positron beam. The HERA experiments need to rely on sophisticated triggering systems, selecting the good events very quickly. The

trigger of the H1 detector is divided into four levels. A description of the H1 trigger system can be found in [11, 12, 13].

The first and second level systems (L1 and L2) are phase-locked to the HERA accelerator clock of 10.4 MHz. The L1 system provides a trigger decision for each bunch crossing after  $2.3 \mu\text{s}$  without causing dead time. Pipelines in the different subsystems store the data for this period. Every L1 subsystem generates trigger information coded in bit pattern of a multiple of 8 bits. These bit patterns are called trigger elements and contain special information of the event. With Boolean decisions subtriggers are formed from the different subsystem trigger elements in the central trigger system. The central trigger system merges all the trigger information of the different subsystems and the different levels.

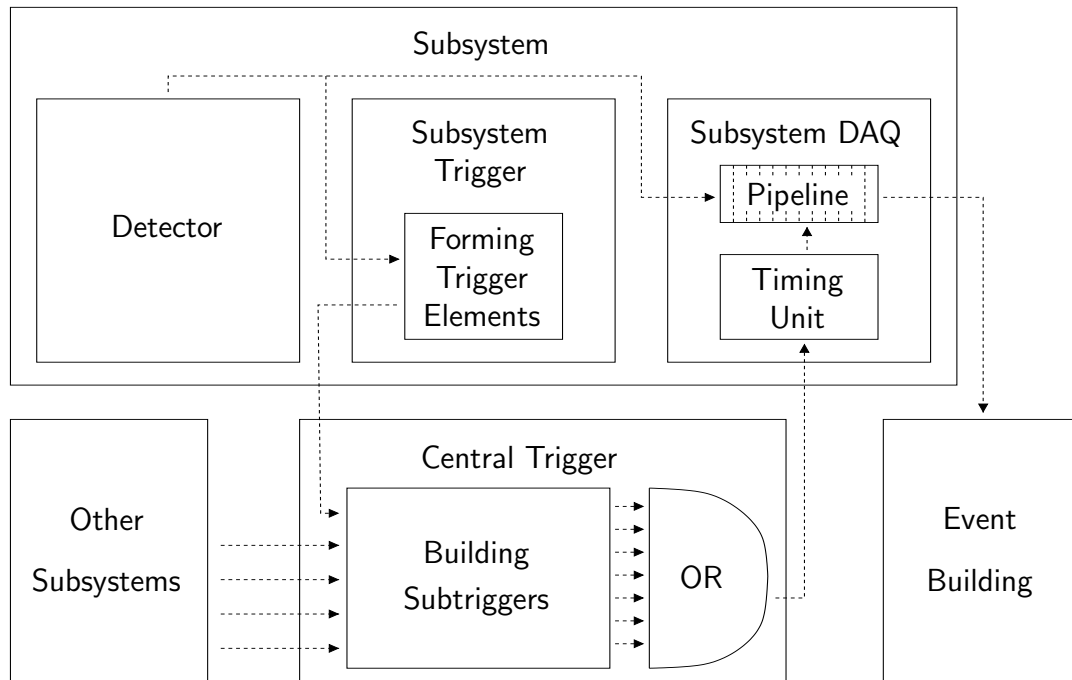


Figure 3.8: *Principle of pipelining in H1 subsystems. The chamber information is stored in a pipeline to avoid dead time in the first level of the trigger system. After a positive trigger decision the corresponding event information is read out from the pipelines.*

If one subtrigger comes to a positive decision the L1 Keep signal is sent to the subsystems and stops the pipelines. Figure 3.8 shows the principle of pipelining and the calculation of the trigger decision. All signals used until this point are synchronous to the HERA Clock. These signals are called fast signals. After the L1 trigger decision the asynchronous part of the trigger and the readout system begins. The event is passed to the second level trigger (L2). Here the signals of different detector components can be connected to provide topological information about the event. Signals used in the asynchronous communication

are called slow signals. The full detector information is available on the next trigger level (L4), which performs a partial reconstruction of the whole event to verify the decision of the previous levels. The events accepted by L4 are written to tape with a typical rate of 10-20 Hz. Finally, the accepted raw data are subject to the full event reconstruction. The events are classified according to different physics categories, what is also known as L5 classification.

An overview of the H1 DAQ system can be found in [11, 12, 13]. A total of over a quarter of a million analogue channels are read out and digitized, resulting in some 3 Mbyte of raw digitized information for a triggered event. The levels of hardware triggering, software filtering and digital compression reduce the event size to between 50 KByte and 100 KByte. Figure 3.9 shows an overview of the H1 detector readout system. The whole data is passed from the subsystems via an optical readout ring to the event building unit where the data is examined in different stages and written on tape. For the readout the individual subsystems use VME bus crates each containing a readout controller, a memory buffer and a fibre optic link to a coordinating event manager.

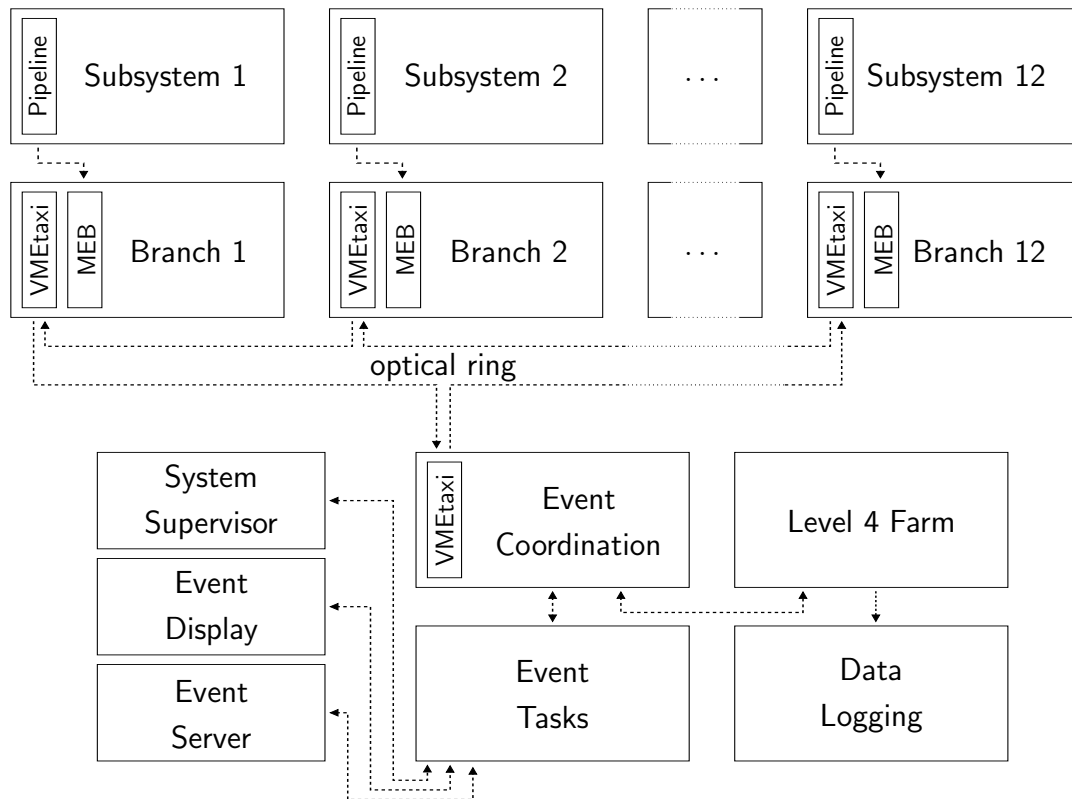


Figure 3.9: Principle of the H1 detector readout. The different subsystems are connected to the main event building via an optical ring. The event coordination collects the full event data. It is processed in the event task unit. After processing the data it is send to the data logging. The Level 4 farm does first online reconstructions on the read out data.

The event manager coordinates the data flow between the optical readout ring, systems observing the read out data and the process of data logging. The different parts of the optical link are called branches. Some subsystems share the same optical branch. The VME bus and VSB bus are used as the main standards in the H1 detector readout. VMEtaxi [14] cards are used to drive the optical ring connecting the subdetector VME crates to the event building.

# Chapter 4

## Background processes at HERA

In this section the theoretical foundation on background scattering processes of positrons and protons for this analysis is introduced. At the Hadron-Elektron-Ring-Anlage HERA positrons and protons collide with a centre-of-mass energy of up to 319 GeV. These high-energetic positron-proton interactions provide an unique testing ground for the Standard Model and allow for the investigation of complementary aspects compared to electron-positron annihilation and proton-antiproton scattering processes. At moderate energies the scattering of positrons on protons is essentially an elastic process, where the proton recoils from the impact but is actually resumed intact after the interaction. The differential cross section for the positron-proton elastic scattering has been calculated for the first time in 1950 and is known as Rosenbluth formula. It is dominated by the form factors, which determine how the scattering process is reduced from its value for a pointlike proton.

In 1954 physicists supplied the experimental evidence that protons have a measurable diameter. Raising the momentum transfer between the positron and proton and thus increasing the spatial resolution, the structure of the proton is resolved. Within this high-energetic probing process the proton is getting likely to break up, referred to as inelastic positron-proton scattering, where no restriction is applied on the type of the hadronic final state.

In 1964 Gell-Mann and Zweig postulated that all hadrons are composed of pointlike particles, which Gell-Mann called quarks. From that point of view the elastic positron-quark scattering is getting accessible within the inelastic scattering process of positrons on protons. Finally, the early 1970's saw the discovery of the quarks in experiments performed at the Stanford Linear Accelerator SLAC. The inclusive measurements of e.g. the inclusive cross sections give directly access to the proton structure functions.

The pattern of perturbative QCD is maybe even better accessible in the exploration of the hadronic final state. Although colored partons can not be observed directly, their fragmentation produces jets of hadrons collimated around the primal direction of the partons. In such a way the gluon has been observed for the first time in the measurement of three-jet events at the PETRA accelerator at DESY in 1979. The investigation of exclusive final states allows for the search

for signals of new physics which would manifest themselves in dedicated event topologies. The presented analysis in this thesis makes use of the investigation of certain exclusive final states.

The following sections introduce the relevant background processes covered by the Standard Model creating similar signatures as the signal process introduced in Section 2.3.

## 4.1 Kinematics and cross sections of positron-proton interactions

The theoretical description of the scattering process of positrons on protons is based on the theory of electroweak interactions and the Quantum Chromodynamics.

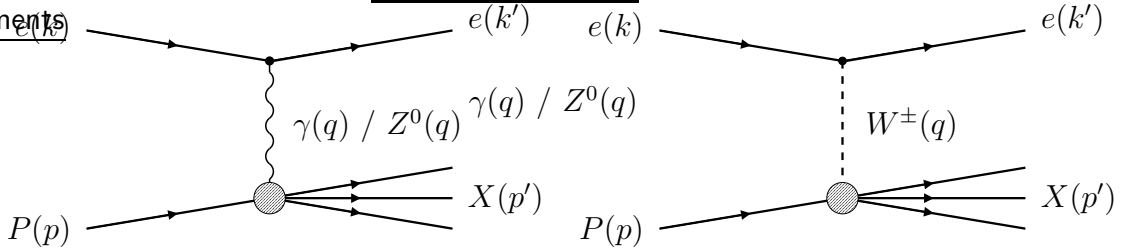


Figure 4.1: *Lowest-order diagrams for positron-proton scattering for neutral current (left) and charged current (right) processes.*

In the most general case the amount of possible reactions is subdivided into two kinds of processes according to the type of the intermediate bosons as depicted in figure 4.1.

The incoming positron with the four-momentum  $k$  interacts with the proton carrying the four-momentum  $p$  via the exchange of an electroweak gauge boson transferring the four-momentum  $q$ . Since the lepton number has to be conserved, the final state consist of a scattered lepton with the four-momentum  $k'$ , while the struck proton might fragment into the hadronic system  $X$  carrying the four-momentum  $p'$ .

In case of neutral current (NC) processes  $ep \rightarrow eX$  the exchanged boson is a neutral particle ( $\gamma$  or  $Z^0$ ), while charged particles ( $W^+$  or  $W^-$ ) mediate the interaction in charged current (CC) processes  $ep \rightarrow \nu X$  resulting in the outgoing lepton being a neutrino.

Based on the four-momenta of the initial positron, the final state lepton and the incoming proton, the kinematics of the positron-proton scattering are determined at the lowest-order by the following three Lorentz-invariant variables:

$$Q^2 = -q^2 = -(k - k')^2 \quad (4.1)$$

$$x = \frac{Q^2}{2(p \cdot q)} \quad (4.2)$$

$$y = \frac{p \cdot q}{p \cdot k} \quad (4.3)$$

$Q^2$ , defined as the negative square of the four-momentum transfer  $q$ , is a measure of the virtuality of the intermediate boson and determines the hardness or resolving power of the interaction. The non-dimensional variables  $x$  and  $y$  are ranging between zero and one and are best understood in dedicated frames of reference.

$x$  is called the Bjørken scaling variable. Its value evaluated in the infinite momentum frame of the proton can be interpreted in the framework of the Quark Parton Model as the proton momentum fraction carried by the struck quark. In the rest frame of the proton  $y$  determines the relative energy loss of the scattered positron and gives thus a measure of the inelasticity of the interaction.

In the proton rest frame  $y$  is given by  $y = 1 - \frac{E_{k'}}{E_k}$ , where  $E_k$  and  $E_{k'}$  denote the energies of the incoming positron and scattered lepton in this frame of reference. The square of the centre-of-mass energy  $s$  and the square of the invariant mass  $W^2$  of the hadronic system  $X$  recoiling against the scattered lepton are given by:

$$s = (k + p)^2 \quad \text{and} \quad W^2 = (p + q)^2 = p'^2 \quad (4.4)$$

Based on the invariant mass  $W$  of the hadronic system the mentioned transition from the elastic to the inelastic regime of positron-proton scattering can be formulated more quantitatively. In case of elastic interactions where the proton does not break up the value of  $W$  apparently amounts to the mass of the proton. For increasing energy transfers the proton might be excited into a resonant state, such as the  $\Delta^+$ . In this case of the so called quasi-elastic scattering the invariant mass  $W$  reaches values of the order of the mass of the according resonance. Entering the regime of inelastic positron-proton scattering, the complicated multi-particle final states with large invariant masses result in a smooth distribution of  $W$ .

Neglecting the positron and proton masses the square of the centre-of-mass energy is connected with the energies of the incoming positron  $E_k$  and proton  $E_p$  via the relation:

$$s = 4 \cdot E_k \cdot E_p \quad (4.5)$$

Under the same assumption the following equations are obtained, relating the introduced kinematic variables  $Q^2$ ,  $x$ ,  $y$ ,  $W^2$  and  $s$ :

$$Q^2 = s \cdot x \cdot y \quad W^2 = Q^2 \frac{1-x}{x} \quad (4.6)$$

In case of fixed centre-of-mass energies  $\sqrt{s}$ , as it is true for the HERA accelerator, only two of those four Lorentz-invariant variables  $Q^2$ ,  $x$ ,  $y$ ,  $W^2$  are independent and sufficient to determine the kinematics of the positron-proton scattering.

The inclusive differential cross section, integrated over all possible hadronic final states of the positron-proton scattering process, is a function of two independent variables uniquely determining the kinematics of the events. In anticipation of the structure of the proton the variables  $x$  and  $Q^2$  are typically chosen for parametrisation.

Based on the diagrams in figure 4.1 the double differential cross section for inelastic positron-proton scattering is given at lowest order in electroweak interactions in the most general formulation by the convolution of a leptonic tensor  $L_{\mu\nu}$  and a hadronic tensor  $W^{\mu\nu}$ , which describe the currents at the corresponding vertices:

$$\frac{d^2\sigma}{dx dQ^2} \propto \epsilon_V L_{\mu\nu}^V(k, q) \cdot W_V^{\mu\nu}(p, q) \quad (4.7)$$

The subscript  $V$  labels the exchanged vector bosons  $\gamma$  and  $Z^0$  for neutral current processes and  $W^\pm$  in case of charged current interactions. The according couplings of the intermediate bosons to the particles involved in the scattering process are given by  $\epsilon_V$ .

The leptonic part of the diagrams is calculable within the electroweak theory. The tensor  $W_V^{\mu\nu}$  serves to parametrise the ignorance of the form of the currents at the hadronic vertex. Exploiting the Lorentz structure of the hadronic tensor and the restriction of current conservation the double differential cross section for unpolarised positron-proton scattering can finally be expressed as:

$$\begin{aligned} \frac{d^2\sigma^{e^\pm p}}{dx dQ^2} = \mathcal{A} \cdot \left[ \frac{y^2}{2} \cdot 2 \cdot x \cdot \mathcal{F}_1(x, Q^2) \right. \\ \left. + (1 - y) \cdot \mathcal{F}_2(x, Q^2) \right. \\ \left. \mp \left( y - \frac{y^2}{2} \right) \cdot x \cdot \mathcal{F}_3(x, Q^2) \right] \quad (4.8) \end{aligned}$$

The factor  $\mathcal{A}$  varies for neutral and charged current processes and is given by:

$$\mathcal{A}^{NC} = \frac{4\pi \alpha^2}{x Q^4} \quad \text{and} \quad \mathcal{A}^{CC} = \frac{G_F^2}{2\pi x} \cdot \left( \frac{M_W^2}{Q^2 + M_W^2} \right)^2 \quad (4.9)$$

where  $M_W$  denotes the mass of the  $W$  boson and  $G_F$  is the Fermi constant. The unknown interaction at the proton side is absorbed in the definition of the generalised proton structure functions  $\mathcal{F}_i(x, Q^2)$ , which are sensitive to the structure of the proton and are in general functions of the kinematics of the scattering process. The generalised structure functions are process dependent, since they encode the contributions arising from the exchange of the various electroweak

bosons. In such a way the expected  $Z^0$  propagator is completely absorbed in case of neutral current interactions. The structure function  $F_3$  is non-zero only for weak interactions as it is generated by the parity violating interactions. The positron-proton scattering is dominated by processes with very small momentum transfers. In this kinematic domain the weak interactions mediated by  $Z^0$  and  $W$  exchange can be neglected compared to the dominant cross section of the electromagnetic scattering process. In the limit  $Q^2 \rightarrow 0 \text{ GeV}^2$  the exchanged photon adopts the character of real photons and the positron-proton interaction can be considered as photon-proton scattering. The positron-proton scattering is then referred to as photoproduction, in analogy to the denotation of the process of hadron production in the scattering of real photons on nucleons.

## 4.2 Neutral Current DIS

In interactions with high momentum transfers between the positron and the proton, the partons behave as free particles and the positron scatters incoherently off single partons. Therefore, deep-inelastic eq scattering (DIS) [15, 16] is also known as elastic ep scattering. DIS denotes interactions which have  $Q^2 \gg M_p^2$  (deep) and  $W^2 \gg M_p^2$  (inelastic) where  $M_p$  is the proton mass and  $W$  is the center-of-mass energy of the exchanged gauge boson and the proton.

The signature of NC DIS events is dominated by a so called scattered parton jet originating from the parton which was interacting with the exchanged gauge boson and the scattered positron most of the time seen in the detector depending on its  $\theta$  value. The remaining partons of the proton which proceed along the proton direction hadronise and produce a jet close to the beam axis. NC DIS events can mimic the event signature of excited quarks if the track pointing to the scattered electron is missing due to inefficiencies of the tracking detector or dead regions. In this case the scattered electron is missidentified as an photon leading to the typical photon-jet signature of the excited quark decay.

### 4.2.1 Radiative Processes

Hard photons may arise from next-to-leading order QED corrections on the positron-proton scattering process involving the radiation of real photons. For neutral current scattering initial and final state radiation from both the positron and quark lines contribute.

Since the cross section for the emission of real photons depends inversely proportional at least on the logarithm of the mass of the radiating particle, the radiation processes from the quark lines are suppressed due to the relative large effective quark masses. The radiation of real photons proceeds in both elastic and inelastic scattering processes. Depending on the kinematics of the interaction the radiated photon receives large transverse momentum and is thus directly observable in the

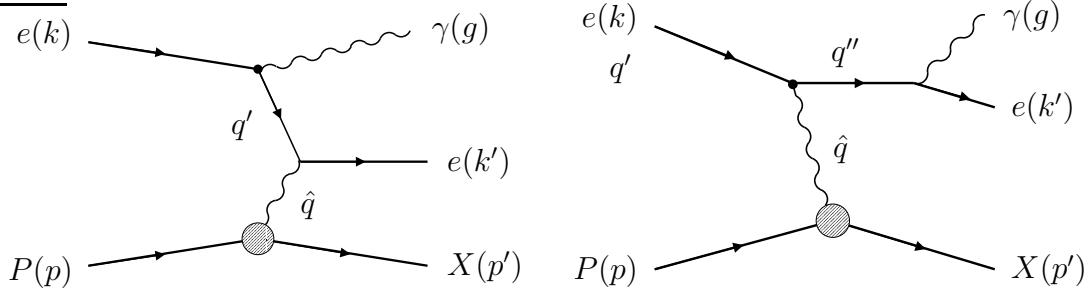


Figure 4.2: *Diagrams for initial (left) and final (right) state photon radiation in electromagnetic  $ep$  scattering.*

measurement. Figure 4.2 shows the diagrams for the initial and final state radiation processes including the assignment of the four-momenta to the participating particles. With the following definitions of the four-momenta transferred by the intermediate photon and the virtual positron states:

$$\hat{Q}^2 = -\hat{q}^2 = -(p' - p)^2 \quad (4.10)$$

$$Q'^2 = -q'^2 = -(k - g)^2 \quad (4.11)$$

$$Q''^2 = -q''^2 = (k' + g)^2 \quad (4.12)$$

the double differential cross sections for the initial and final state radiation processes are determined by:

$$\frac{d^2\sigma}{d\hat{Q}^2 dQ'^2} \propto \frac{1}{\hat{Q}^2 (Q'^2 + m_e^2)} \quad \text{and} \quad \frac{d^2\sigma}{d\hat{Q}^2 dQ''^2} \propto \frac{1}{\hat{Q}^2 (Q''^2 + m_e^2)} \quad (4.13)$$

The diagrams shown in figure 4.2 represent the real QED corrections at the positron line to the deep-inelastic electromagnetic scattering process. The photon emission proceeds for both the initial and final state radiation processes preferably collinear to the direction of the incoming and scattered positron. If the photon is radiated in the initial state the positron momentum is decreased, resulting in a reduction of the effective centre-of-mass energy available in the subsequent scattering process. The radiated photon mostly remains undetected in the primal direction of the positron. In the case of final state radiation both electromagnetic particles typically form a common energy cluster preventing the experimental discrimination between the positron and photon. For both processes the photon becomes observable in the measurement with increasing values of  $Q'^2$  and  $\hat{Q}^2$ . In rare cases if the angle between the radiated photon and the positron is big this signature can be misidentified as the excited quark decay signature if the electron vanishes through the beampipe and is not visible in the detector. Radiative processes can also lead to signal like event topologies in charged current

events  $ep \rightarrow \nu X$ . For this class of events a charged  $W$  is exchanged in the interaction of the positron with the proton. The outgoing neutrino is not detected and leads to missing transverse momentum. Background from radiative charged current events plays a minor role in the composition of the background sources and was therefore neglected in this analysis. Its final contribution is discussed in Section 5.5.4.

## 4.3 Photoproduction

The cross section of ep interactions decreases strongly with  $Q^2$ . In the region of  $Q^2 \approx 0$  we can consider the exchanged photon as almost real. These events are called photoproduction events because they can be considered as  $\gamma p$  scattering events. The positron can be seen as a source of photons with an energy spectrum given by the Weizsäcker Williams formula integrated to a maximal  $Q_{max}^2$

$$f_{\gamma e} = \frac{\alpha}{2\pi} \cdot \frac{1 + (1-x)^2}{x} \cdot \log \left( \frac{Q_{max}^2 (1-x)}{m_e^2 \cdot x^2} \right) \quad (4.14)$$

The photon is an elementary particle but it can fluctuate into virtual pairs of charged leptons or quarks for a short time according to the quantum uncertainty principle. For photons of high energy the quark-antiquark pair can develop into a quark-gluon cascade leading to a complicated partonic object with the same quantum numbers as the photon. We distinguish two classes of photoproduction according to the fluctuation of the photon. In the direct process the exchanged photon couples directly to the quarks of the proton. In the resolved process the photon fluctuates into a hadronic state and a parton of the photon enters the hard interaction. In this case there is a photon remnant which is not participating in the hard interaction similar to the case of the positron proton interaction. The main background processes in the photoproduction regime are the dijet photoproduction events and the prompt photon events. As in the NC DIS regime radiative processes contribute to the photoproduction background in this analysis, too.

### 4.3.1 Dijet Photoproduction

In the direct dijet photoproduction a quasi real photon interacts with a quark of the proton. In the resolved photoproduction process a virtual photon acts as a source of partons. One of the partons takes part in the hard subprocess. One of the main signatures of the resolved process is the low  $p_T$  photon remnant which did not take part in the scattering. Figure 4.3 shows the Feynman diagrams for direct and resolved dijet photoproduction. The outgoing jets can mimic a photon signal if most of the jet energy is carried by a neutral meson, typically  $\pi_0$  or  $\eta$ .  $\pi_0$  and  $\eta$  both decay into photons very close to each other and can not be resolved in the detector. These processes can lead to an excited quark decay like signature and have to be considered as a background source.

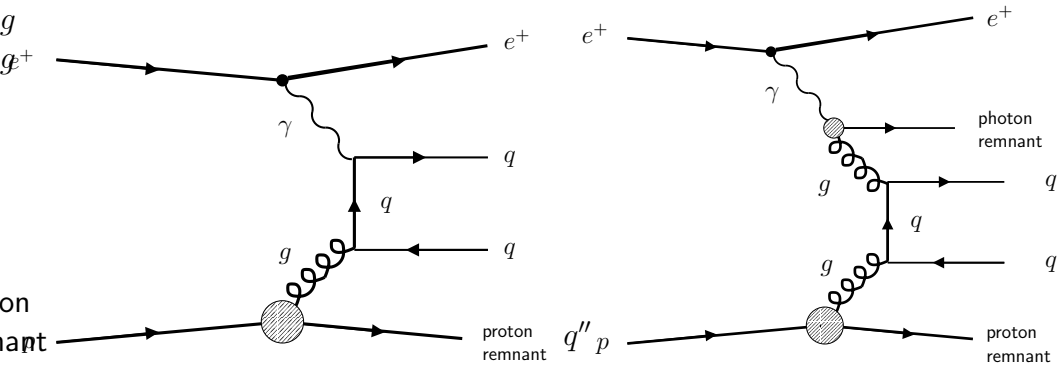


Figure 4.3: *Examples for leading order Feynman diagrams for direct (left) and resolved (right) dijet photoproduction*

### 4.3.2 Prompt Photon Production

In the regime of photoproduction the production of photons in hard interactions is referred to as prompt photon production. Both direct and resolved photoproduction processes contribute. The process of prompt photon production is sensitive to the partonic structure of the proton and due to the resolved component also to the parton content of the photon.

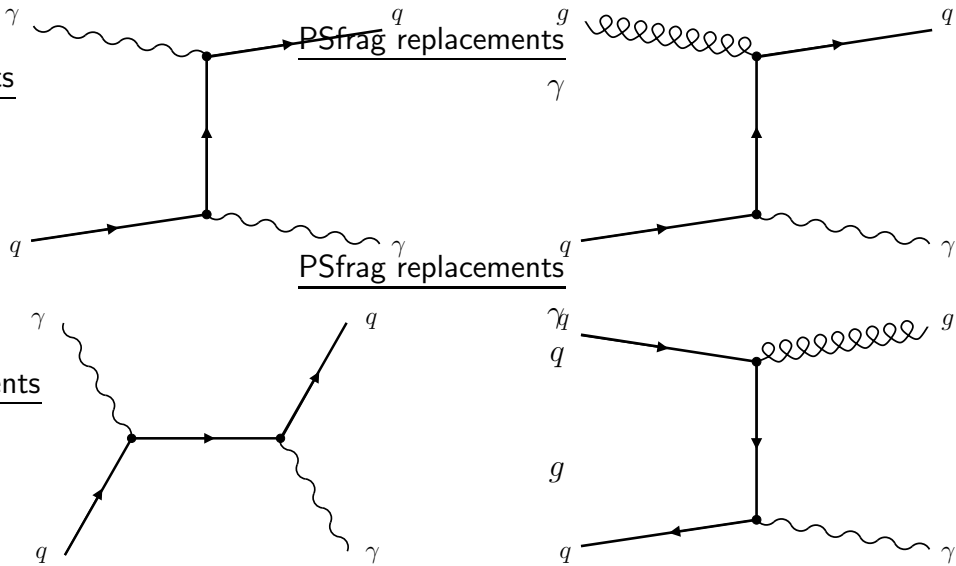


Figure 4.4: *First order diagrams for direct (left) and resolved (right) prompt photon production processes at leading order*

Figure 4.4 shows diagrams of prompt photoproduction at leading order. In comparison to the dijet photoproduction events the cross section of the prompt photon processes are reduced by  $\sim \frac{\alpha}{\alpha_S}$ . But even with this low cross section they play an important role as background processes in this analysis because the events have the same signature as the excited quarks.

# Chapter 5

## Analysis of the production of Excited Quarks

This analysis of the production of excited quarks is carried out by investigating the dominant channel of the excited quark decaying into a jet and a photon. This chapter introduces all data sets used beginning with the data collected by the H1 detector up to all Monte Carlo generated event files for the expected signal and all background processes. The preselection applied on all data sets is explained. The detection of electromagnetic particles and jets as well as the detection of photons is described in detail. The final results are compared to the recent H1 publication. The analysis was carried out with the H1OOlt Analysis Framework package [17] as part of the H1OO environment in version 2.5.10 [18].

### 5.1 Data, Background and Signal Samples

At HERA positrons collide with an energy of 27.6 GeV with protons at an energy of 920 GeV resulting in a centre-of-mass energy of  $\sqrt{s} = 319$  GeV. The data which was used for this analysis was collected in the years 1999/2000 with an integrated luminosity of  $63.0041 \text{ pb}^{-1}$ .

Extensive software packages are used to simulate dedicated physical processes and the according detector response with the so-called Monte Carlo technique. Based on theoretically calculated cross sections Monte Carlo event generators deliver the four-momenta of the final state particles and the detector response is determined by the simulation software. Events are reconstructed using the same reconstruction program as for the data. Processes not computable within the framework of perturbative theory, such as the fragmentation of quarks and gluons into hadrons, are approached using phenomenological models. The following paragraphs describe the considered processes and their Monte Carlo generation. This analysis investigates the phase space region of high transverse momenta. In this kinematic regime the dominating SM background processes are photoproduction and neutral current deep-inelastic scattering. All processes are generated

with a luminosity significantly higher than the luminosity of the analysed data sample. A summary of the data sets and Monte Carlo samples used in this analysis is presented in Table 5.1.

Gen-Id	Description	Events	Luminosity
Data sets:			
Data	1999 positron data: CDST3.C9900001-C9900620 2000 positron data: CDST3.C0000001-C0000792 CDST3.C0000831-C0001628		63.0041 pb <sup>-1</sup>
Background MC sets:			
1821	Generator RAPGAP: Neutral Current DIS ( $Q^2 > 4$ GeV)	257741	81.01 pb <sup>-1</sup>
1808	Neutral Current DIS ( $Q^2 > 100$ GeV)	1000000	220.01 pb <sup>-1</sup>
Generator PYTHIA:			
1625	Resolved Photoproduction	1165591	999.54 pb <sup>-1</sup>
1624	Direct Photoproduction including Direct Prompt Photons	533035	1000.18 pb <sup>-1</sup>
1265	Resolved Prompt Photons	8176	128.48 pb <sup>-1</sup>
1271	Resolved Prompt Photons	10055	279.07 pb <sup>-1</sup>
Signal MC sets:			
Generator FERMION:			
2719	Excited Quarks ( $m_{q^*} = 50$ GeV)	100000	
2720	Excited Quarks ( $m_{q^*} = 75$ GeV)	100000	
2721	Excited Quarks ( $m_{q^*} = 100$ GeV)	100000	
2722	Excited Quarks ( $m_{q^*} = 125$ GeV)	100000	
2723	Excited Quarks ( $m_{q^*} = 150$ GeV)	100000	
2724	Excited Quarks ( $m_{q^*} = 175$ GeV)	100000	
2725	Excited Quarks ( $m_{q^*} = 200$ GeV)	100000	
2726	Excited Quarks ( $m_{q^*} = 225$ GeV)	100000	
2728	Excited Quarks ( $m_{q^*} = 250$ GeV)	100000	

Table 5.1: Summary of the data sets and Monte Carlo samples used in this analysis. For comparisons the unique generator-id for the MC simulated data is given.

## Photoproduction

The PYTHIA event generator [19] is used to simulate the direct and resolved photoproduction and the direct and resolved production of prompt photons. The simulation contains the Born level hard scattering matrix elements and radiative

QED corrections. Higher order QCD effects are accounted for by leading logarithmic parton showers. The hadronization of the outgoing partons is based on the Lund String model [20]. The parton density function (pdf) GRV LO [21] is used on the photon side and the CTEQ5L [22] pdf is chosen for the proton.

## Neutral Current Deep-Inelastic Scattering

The RAPGAP [23] event generator is used to model neutral current DIS events. QED radiative effects due to real photon emission from both the incoming and outgoing positron as well as one-loop virtual corrections are simulated using the HERACLES [24] generator. The generation of parton cascades is based on the leading logarithmic parton shower approach, accounting for higher order QCD effects. The CTEQ5L pdf is used on the proton side to evaluate the nominal NC cross section.

## Excited Quark event generator

The generator FERMION [25] is used to generate events where excited quarks are produced. It uses an integration package BASES and SPRING [26], which yields an efficient method to generate points in phase space. The proton structure functions was chosen to be the PDFLIB 2.02 package (CERN W5051 H. Plothow-Besch). The fragmentation and decay of unstable particles is covered by the Lund program JETSET 7.3 [27], which is called after generating the event on the quark parton level.

In the simplest case the excited quark states which are produced have spin 1/2 and are produced as resonances in photon quark reactions, where the photon comes from the incoming positron [28]. The Weizsäcker Williams formula is used to obtain the energy spectrum of the photons, which are taken to be collinear radiated. The number of photons in the positron with energy fraction  $z$ ,  $E_\gamma = zE_e$  is given by [29]:

$$f_{\gamma e} = \frac{\alpha}{2\pi} \cdot \frac{1 + (1 - z)^2}{z} \cdot \log\left(\frac{s}{4m_e^2}\right) \quad (5.1)$$

$\alpha$  is the electromagnetic coupling constant,  $s$  is the center of mass energy squared, and  $m_e$  is the electron mass. A lower limit for  $z$  is naturally given by requiring enough energy in the quark photon subsystem to produce the excited quark. The differential cross section for the subprocess  $q + \gamma \rightarrow q^* \rightarrow q + \gamma$  is:

$$\frac{d\hat{\sigma}}{dQ^2} = \frac{-\pi\alpha^2 Q_q^2}{\Lambda^4} \cdot \frac{\hat{u}}{\hat{s}} \cdot \left[ \frac{\hat{s}^2}{(\hat{s} - m_*^2)^2 + m_*^2 \Gamma_*^2} + \frac{\hat{u}^2}{(\hat{u} - m_*^2)^2} \right] \quad (5.2)$$

with  $Q_q$  being the electric charge of the quark.  $m_*$  and  $\Gamma_*$  are the mass and the total decay width of the excited quark, respectively. The Mandelstam variables

used in the equation are:

$$\hat{s} = (p_\gamma + p_q)^2 = x \cdot z \cdot s, \quad (5.3)$$

$$\hat{t} = (p_q - p'_q)^2 = -Q^2, \quad (5.4)$$

$$\hat{u} = (p_q - p'_\gamma)^2 = Q^2 - \hat{s}. \quad (5.5)$$

The parameter  $\Lambda$  gives the coupling strength of the excited quarks to the normal quarks and photons. The decay width is:

$$\Gamma_* = \frac{\alpha |Q_q|}{4} \cdot \frac{m_*^3}{\Lambda^2} \quad (5.6)$$

and the angular distribution in the  $q^*$  rest frame is given by:

$$\frac{d\Gamma}{d\cos\theta^*} \sim 1 + \cos\theta^* \quad (5.7)$$

The total differential cross section is then obtained by folding the subprocess formula with the quark distribution of the proton:

$$\frac{d\sigma}{dx dz dQ^2} = f_{\gamma,e} \cdot \frac{d\hat{\sigma}}{dQ^2} \cdot q(x, Q^2) \quad (5.8)$$

Here  $x$  and  $Q^2$  are not equal to  $x_{Bj}$  and  $Q_{Bj}^2$  but they are defined as above.

All generated events are passed through a full detector simulation using the H1 simulation program H1SIM based on the GEANT [30] software package. Taking into account the geometrical setup and material parameters of each sub-component the response of the H1 detector for every simulated particle is determined. All secondary particles produced are tracked stepwise in their way through the detector and interaction with the material is simulated based on the according cross sections. As for real data the simulated events are reconstructed using the H1 software package H1REC and subject to the same analysis chain in order to compare the measurement with the prediction provided by the Standard Model. To ensure stable detector conditions and to reduce non-ep background events a preselection is applied on all different data sets. This preselection is described in the next section.

## 5.2 Preselection

The preselection described in this section is applied to all data sets. At first general and kinematic cuts are applied. Only runs with good and medium quality are used from the recorded data. In addition all major systems which are essential for the analysis are required to be operational. These subdetectors are the luminosity system, the LAr calorimeter, the Central Jet Chambers CJC1 and CJC2 as well as the Central Proportional Chamber CIP. For these detectors the HV has to be turned on for each subdetector. To reduce non-ep background events the

reconstructed event vertex is restricted to be within a distance of 35 cm around the nominal  $z$  position of the vertex. To ensure a well defined measurement of the event vertex at least one track has to be found in the detector. Figure 5.1 shows the  $z$ -vertex distribution of the data and the MC background samples reweighted to the data sample.

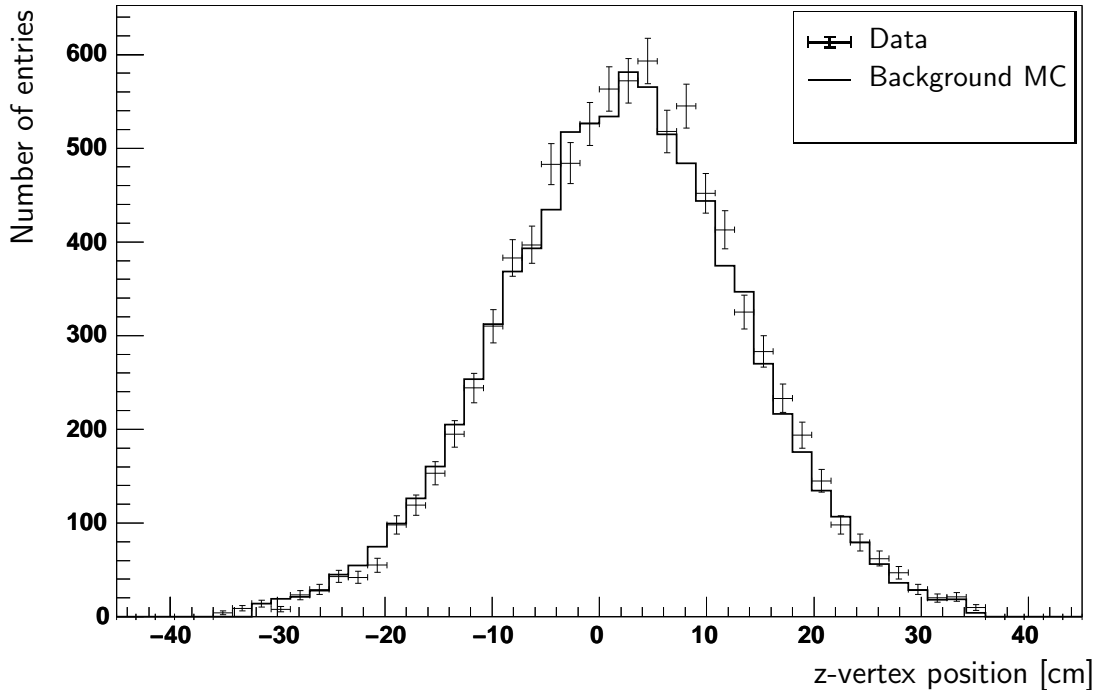


Figure 5.1: *Distribution of the  $z$ -vertex position of data and MC background samples.*

Further background is rejected by searching for event topologies typical for cosmic ray and beam-induced background events. The H100 version [31] of the software package QBGMAR [32] is used, providing 26 background finders, to minimize the remaining non-ep background events.

The subtrigger chosen as the main trigger for this analysis is the subtrigger S67. It triggers on energy deposits above an energy threshold in the electromagnetic and hadronic part of the LAr calorimeter. The efficiency of the analysis subtrigger is calculated with events triggered by an independent subtrigger, the so called monitor trigger. The analysis subtrigger is not allowed to consist of trigger elements which are also used in the monitor trigger. The fraction of events which are triggered by both the analysis subtrigger and the monitor trigger gives the trigger efficiency. As monitor trigger the subtrigger S71 was chosen. It combines information of the central and forward multiwire proportional chambers with calorimetric information with lower thresholds than the electron trigger S67. It triggers, both on electrons and on jets. Since the events studied in this analysis contain a high energetic jet and an electromagnetic particle, S71 can be taken as

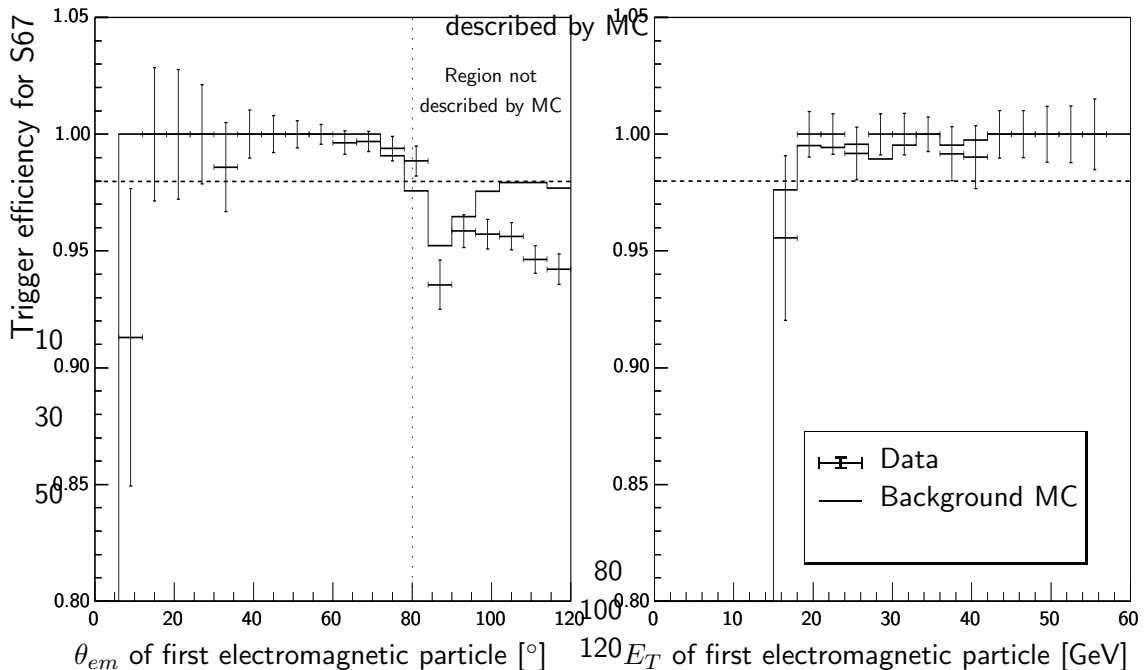


Figure 5.2: Trigger efficiency for the subtrigger S67 with respect to  $\theta_{em}$  (left) and  $E_T$  (right) of the first electromagnetic particle found derived from comparison to subtrigger S71. The data is not well described by the background MC set in the range of  $\theta \geq 80^\circ$ . This region is skipped in the calculation of the trigger efficiency with respect to  $E_T$ . The level of 98 % efficiency is marked with a dashed line.

an independent subtrigger. Figure 5.2 (left) shows the trigger efficiency of subtrigger S67 with respect to  $\theta_{em}$  of the first electromagnetic particle. As one can derive from this plot the data is not well described by the background MC set in the range of  $\theta \geq 80^\circ$ . As this region is not important for the analysis, as will be discussed in the next sections, it was skipped for the evaluation of the trigger efficiency as a function of the transverse energy  $E_T$ . Figure 5.2 (right) shows the efficiency of subtrigger S67 with respect to  $E_T$ . The trigger efficiency is well above 98 % in the kinematic range considered in this analysis and it is well described by the MC background samples. Therefore all events passing the preselection have to be validated by the S67 subtrigger.

To define a clean sample of positrons respectively photons and a jet additional cuts are introduced. The basic preselection requires at least one electromagnetic particle with a transverse momentum bigger than  $p_T > 15 \text{ GeV}$  and a jet to be found anywhere in the detector acceptance with a transverse momentum bigger than  $p_T > 15 \text{ GeV}$  and  $\theta_{jet} > 10^\circ$ . A detailed description and definition of electromagnetic particles and jets can be found in the next sections. The  $\theta$  acceptance for the electromagnetic particle is constraint to  $10^\circ \leq \theta_{em} \leq 120^\circ$ . Close to the cracks of the LAr calorimeter in the  $\phi$  and  $\theta$  plane a clear differentiation between hadrons and photons is very difficult. Furthermore the energy measurement has

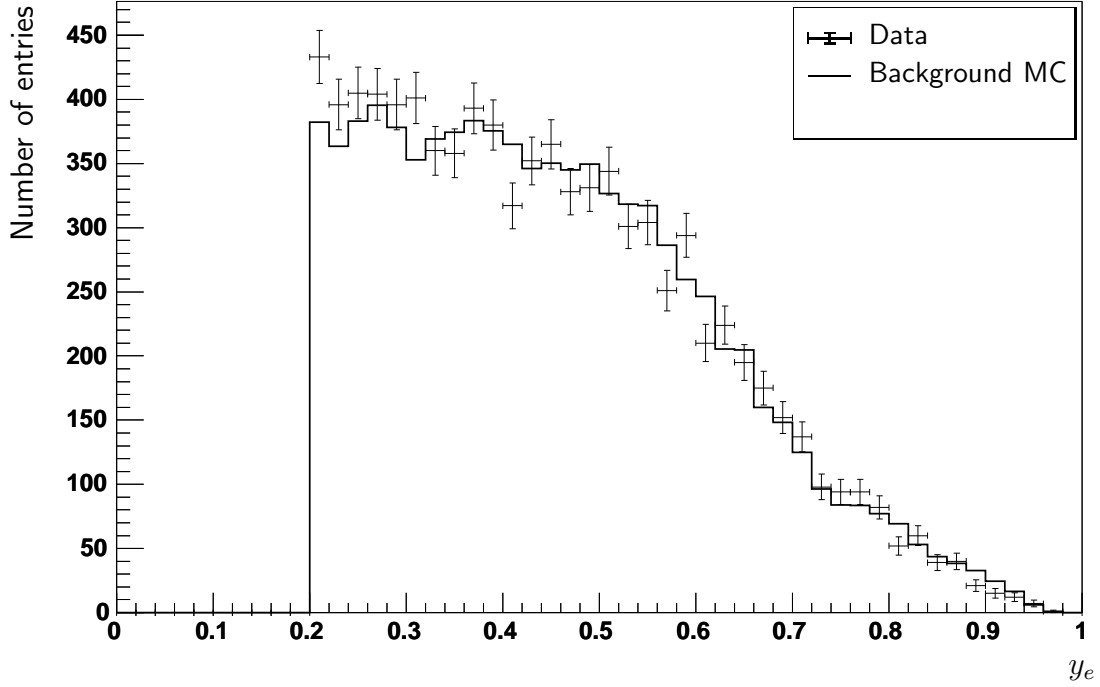


Figure 5.3:  $y_e$  distribution of data and MC background samples.

a large error due to losses in the crack region. For this reason the areas near the cracks are excluded from measurements in this analysis. To reduce further non-ep background events a kinematic cut on  $0.2 \leq y_e \leq 1.0$  is applied. Figure 5.3 shows the distribution of the inelasticity  $y_e$  that can be interpreted as the

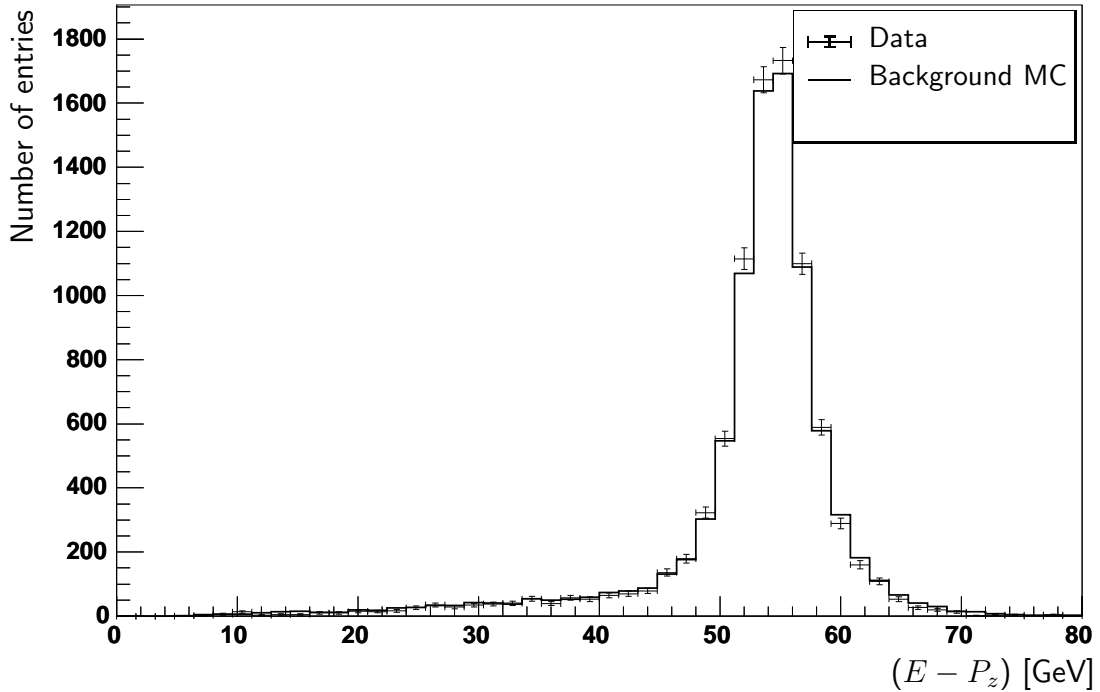


Figure 5.4:  $(E - P_z)$  distribution of data and MC background samples.

fractional energy loss of the scattering lepton. It is calculated using the electron method [33] with  $y_e = 1 - \frac{E'_e}{E_e} \sin^2 \frac{\theta_e}{2}$  exclusively using the measured energy  $E'_e$  and angle  $\theta_e$  of the scattered positron. Figure 5.4 shows the distribution of the variable  $(E - P_z) = \sum_i (E_i - P_{z,i})$  where  $E_i$  and  $P_{z,i} = E_i \cos \theta_i$  are the energy and the longitudinal momentum measured in a calorimeter cell  $i$ . For an event where the only particles which remain undetected are close to the proton direction, momentum conservation implies that  $(E - P_z)$  nearly equals twice the energy of the incoming positron (55 GeV). This signature is found in the distribution showing that mainly neutral current events with an positron and a jet found in the LAr calorimeter remain in the preselected data sample. The preselection is designed such that losses for the signal MC samples are minimal. Figure 5.5 shows the efficiency of the preselection on the MC signal for different masses of the excited quark. The cuts effecting the MC signal the most are the cut on  $\theta$  of the first electromagnetic particle ( $\sim 4\%$  reduction), the cut on  $y_e$  ( $\sim 4\%$  red.) and the cut on the areas around cracks in the LAr calorimeter which is a geometrical cut ( $\sim 12\%$  red.) derived from the LAr calorimeter geometry. The cut on  $p_T$  of the first jet ( $\sim 2\%$  red.) has a smaller but significant effect, too. The average efficiency of the preselection is about 75% in the important mass regions. The shape of the preselection efficiency as a function of the mass of the excited quark can be understood as follows. For the low masses the cut on  $p_T$  of the electromagnetic particle has more effect than for the higher masses. For higher masses the jet is dominantly pointing in the forward region of the detector. The effect of the cut on the lower edge of  $\theta_{jet}$  of the jet gets dominant. An overview of all cuts applied in the preselection can be found in Table 5.2.

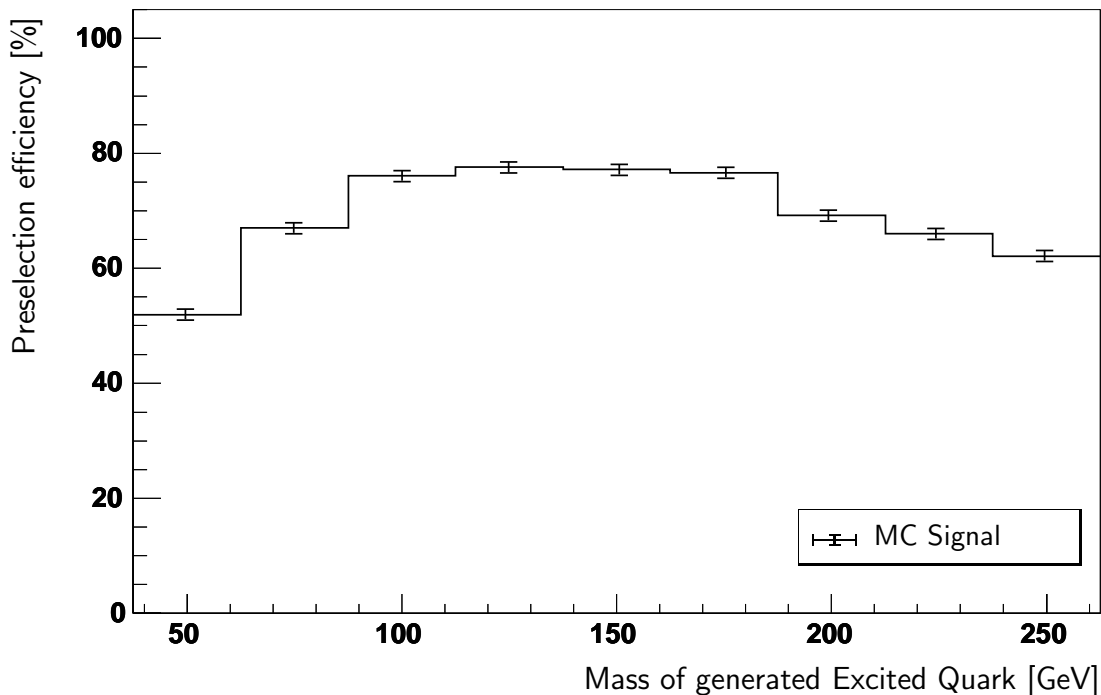


Figure 5.5: *Efficiency of preselection on MC signal data samples.*

General and Kinematic Cuts:	
$z$ -Vertex	$-35 \text{ cm} \leq z_{\text{vtx}} \leq +35 \text{ cm}$
Vertex Type	defined vertex (central or forward)
$y_e$	$0.2 \leq y_e \leq 1.0$
Run Quality	good or medium
HV Cuts: HV on for CJC, LAr, Tof, Lumi, CIP	
Track Cuts:	
Number	1 or more tracks
Trigger Cuts:	
S67	Subtrigger S67 has to be active
Electromagnetic Particle Cuts:	
Number	1 or more electromagnetic particles
$p_T$	$p_T \geq 15 \text{ GeV}$
$\theta_{em}$	$10^\circ \leq \theta_{em} \leq 120^\circ$
Cracks	Remove $\phi$ and $z$ cracks from LAr calorimeter $\pm 2^\circ$ for $\phi$ and $\pm 15 \text{ cm}$ for $z$ cracks
Jet Cuts:	
Number	1 or more jets
$p_T$	$p_T \geq 15 \text{ GeV}$
$\theta_{jet}$	$\theta_{jet} > 10^\circ$

Table 5.2: *Cuts of preselection applied to all data sets.*

### 5.3 Detection of Electromagnetic Particles

This section describes the general detection of electromagnetic particles. The detection of the photon in the typical jet-photon signature of the excited quark decay is very important. The discrimination of photons from other particles is explained in Section 5.5.

Electrons, positrons or photons produce compact and narrow showers by ionisation in the LAr calorimeter. Their shape differs significantly from the shower shape of hadrons which are usually very broad and penetrate deeply into the hadronic part of the calorimeter. The charges are collected in the calorimetric cells and converted by calibration factors into energies. The typical value of electronic noise in a cell is 10 to 20 MeV. A clustering algorithm [34] forms groups of cells corresponding to particle showers. The algorithm is tuned such that it identifies electromagnetic showers (electrons or photons) as single clusters. Hadronic showers instead are in general split into several clusters. Corrections due to

losses in the measured energies in dead material (beam pipe, central tracker, inner cryostat wall) and in the cracks between the calorimeter stacks are applied. The corrections are derived from Monte Carlo studies [11, 35].

To select electron or photon candidates the standard electromagnetic shower finder of H1 named QESCAT [36] is used. It searches for the electromagnetic shower with the highest  $E_T$  fulfilling some shape and isolation criteria. The estimators providing sufficient cluster characteristics are:

- Fraction of energy deposited in the electromagnetic section of the LAr calorimeter.
- Fraction of energy deposited in the cells of the core of the cluster.
- Transverse dispersion:  $\sigma_R = \sqrt{\langle r^2 \rangle - \langle r^1 \rangle^2}$  with  $\langle r^n \rangle = \frac{\sum_{\text{cells}} w_i r_i^n}{\sum_{\text{cells}} w_i}$  and  $n = 1, 2$  where  $w_i$  are the energy densities of the cells  $i$  and  $r_i$  are the distances to the shower axis.
- Energy deposited in a cone starting from the interaction point around the axis of the candidate momentum of radius  $R = 0.25$  in the  $(\eta, \phi)$  plane.
- Energy deposited in the hadronic section of the LAr calorimeter.

An electromagnetic shower is distinguished from a hadronic shower by requiring that almost all its energy is deposited in the electromagnetic part of the liquid Argon calorimeter and only a small fraction of the energy can be found in the hadronic part. Furthermore the shower is asked to be compact to distinguish it

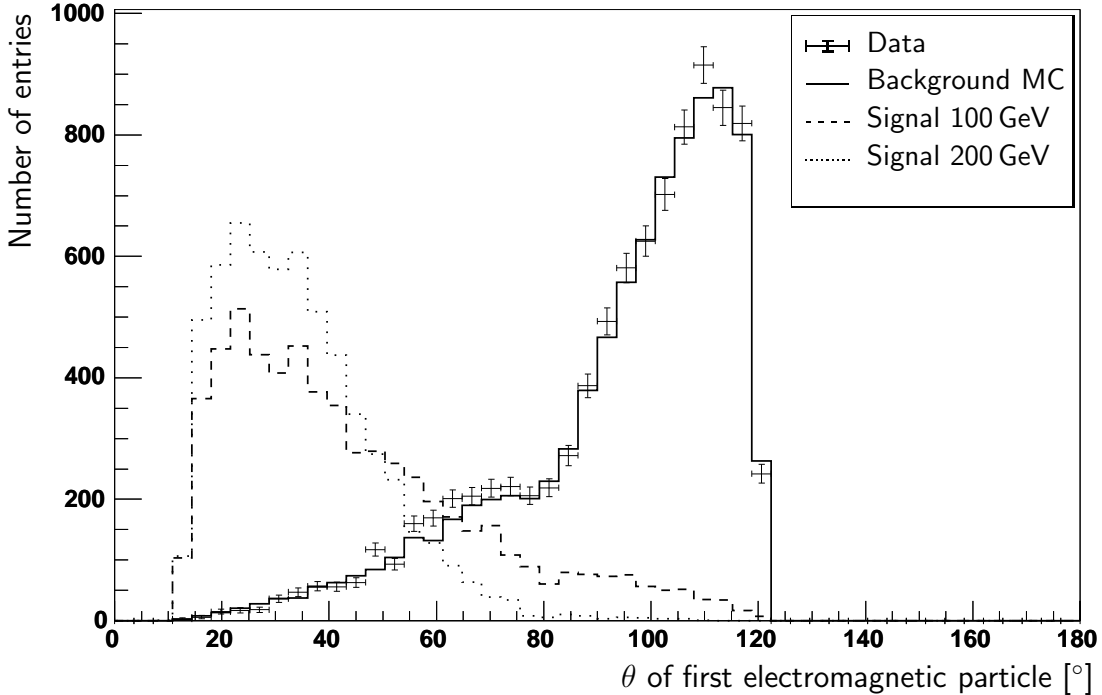


Figure 5.6:  $\theta$  of first electromagnetic particle after preselection. The plot shows data, background MC and signal MC samples (scaled by an arbitrary factor).

from the broader hadronic showers or showers produced by several particles close to each-other. The shower candidate is required to be isolated rejecting candidates that are products of decays with accompanying particles. In addition the shower is required to be formed by at least 3 cells to minimize the impact of electronic noise. The efficiency of the QESCAT finder was studied in [37]. In the kinematic range important for this analysis the efficiency of the electron finder is above 98% outside the crack regions of the LAr calorimeter.

Figure 5.6 and Figure 5.7 show the distribution of the variables  $\theta$  and  $p_T$  of the first electromagnetic particle after the preselection on the different data sets. The particles are ordered descending in  $p_T$ . The distributions for the Signal MC samples corresponding to excited quarks of  $m_{q^*} = 100$  GeV and  $m_{q^*} = 200$  GeV are shown also as dashed and dotted lines scaled by an arbitrary factor. The agreement of the data and the background MC sample is satisfactory. Both variables are used to discriminate the signal events from the different background sources in the further selections.

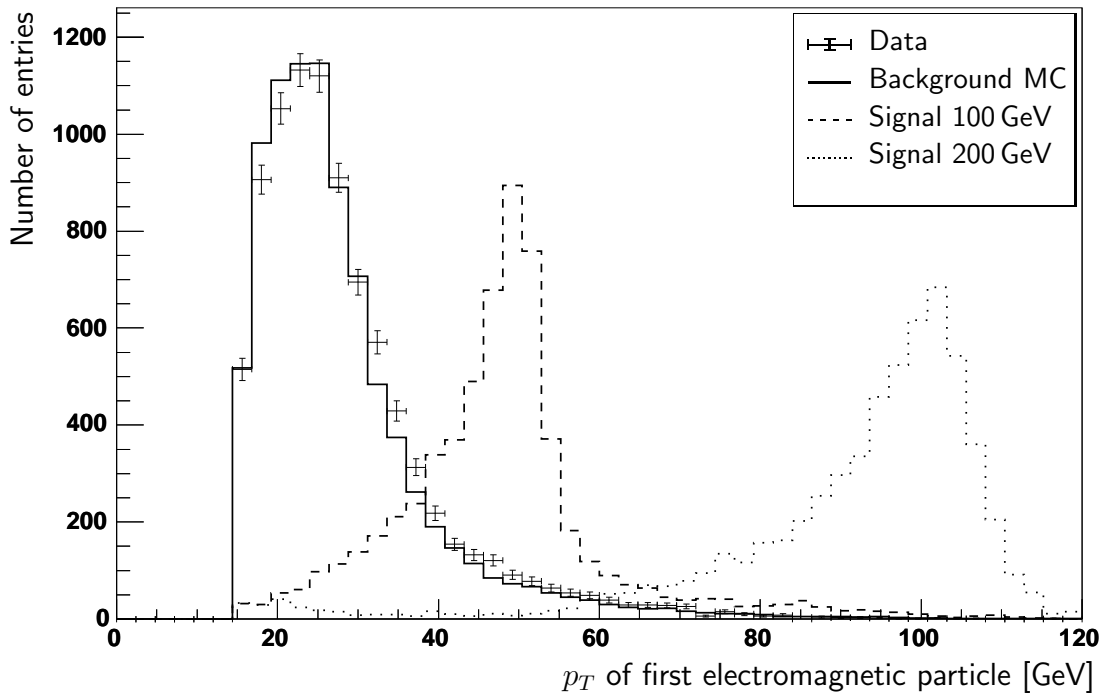


Figure 5.7:  $p_T$  of first electromagnetic particle after preselection. The plot shows data, background MC and signal MC samples (scaled by an arbitrary factor).

## 5.4 Detection of Jets

Jet algorithms are used to define objects in an analysis framework on the different abstraction levels ranging from the experimental detector level to the hadron or parton level. A good correlation between the different levels should be of course ensured. A jet algorithm should minimise the effect of the hadronisation. If two

collinear input objects are replaced by one of the same momentum as the sum of the two individual objects or if soft objects are added the result of the algorithm should stay the same.

Different algorithms have been proposed, tested and optimised. The two most popular algorithms used in collisions involving hadrons are the cone algorithm [38] and the inclusive  $k_T$  algorithm [39]. One basic advantage of the inclusive  $k_T$  algorithm is that it uniquely assigns particles to jets whereas in the cone algorithm particles belonging to more than one overlapping jet need special treatment. In addition comparisons of jet algorithms in DIS [40] have shown that the hadronisation corrections for the inclusive  $k_T$  algorithm are smaller than for the cone algorithm. The application of the inclusive  $k_T$  algorithm has become standard in analyses at HERA [41]. Therefore this algorithm is described in detail in the following.

The inclusive  $k_T$  algorithm is a so-called clustering algorithm that iteratively combines particles into jets until all input particles are merged. As a consequence all particles belong to a jet at the end of the procedure. An additional hardness requirement is necessary to identify the jets of the hard interaction, typically a minimum transverse momentum is required. The different steps in the iterative procedure are as follows:

1. For each object  $i$  calculate the

$$\text{distance to the beam axis : } d_i = p_{T_i}^2 \quad (5.9)$$

2. For each combination of objects  $i$  and  $j$  calculate their

$$\text{distance between each other : } d_{ij} = \min(p_{T_i}^2, p_{T_j}^2) \cdot \frac{\Delta R_{ij}^2}{R_0^2} \quad (5.10)$$

where  $\Delta R_{ij}^2 = \Delta\eta_{ij}^2 + \Delta\phi_{ij}^2$  is the distance of the two objects in the  $\eta - \phi$  plane and  $R_0$  is a separation parameter of the order 1. Here  $\eta = \ln(\tan(\frac{\theta}{2}))$  is the pseudorapidity and  $\phi$  is the azimuthal angle of the object.

3. Find the smallest distances  $d_{i,min}$  and  $d_{ij,min}$ .
4. If  $d_{i,min} < d_{ij,min}$  remove object  $i$  and add it to the list of jets. Otherwise merge particles  $i$  and  $j$  that correspond to  $d_{ij,min}$ .
5. Continue at 1. if there are still objects left in the input list.

The merging of two objects is done according to the  $p_T$ -weighted scheme:

$$p_{T,ij} = p_{T,i} + p_{T,j} \quad (5.11)$$

$$\eta_{ij} = \frac{p_{T,i} \cdot \eta_i + p_{T,j} \cdot \eta_j}{p_{T,ij}} \quad (5.12)$$

$$\phi_{ij} = \frac{p_{T,i} \cdot \phi_i + p_{T,j} \cdot \phi_j}{p_{T,ij}} \quad (5.13)$$

The resulting jets are massless and ordered descendingly in  $p_T$ . An additional cut on the  $p_T$  of these jets yields the final hard jets. The separation parameter  $R_0$  is set to 1. The algorithm is applied in the laboratory frame.

For a better reconstruction of the jet quantities an additional calibration is applied to the individual jets. The hadronic calibration makes use of the fact that for neutral current DIS events the transverse momentum of the scattered positron and of the hadronic final state are balanced. The quantities used for the calibration are determined with the double angle kinematic method. The hadronic transverse momentum determined with this method is independent on the LAr energy calibration to a good approximation. The calibration is said to be absolute if the measured

$$p_{T,\text{had}} = \sqrt{\left(\sum_{\text{had}} p x_{\text{had}}\right)^2 + \left(\sum_{\text{had}} p y_{\text{had}}\right)^2} \quad (5.14)$$

coincides with the  $p_{T,\text{da}}$  defined by

$$p_{T,\text{da}} = \frac{2 E_0}{\tan\frac{\theta_e}{2} + \tan\frac{\theta_h}{2}} \quad (5.15)$$

where  $\tan\frac{\theta_h}{2} = \sum_{\text{had}} \frac{E_{\text{had}} - p_{z,\text{had}}}{p_{T,\text{had}}}$ . With the use of the double angle method as a reference the calibration method does not rely on Monte Carlo samples which are separately calibrated and no relative calibration is needed. The method is also independent of the electron calibration. From  $p_{T,\text{bal}} = \frac{p_{T,\text{had}}}{p_{T,\text{da}}}$  calibration factors

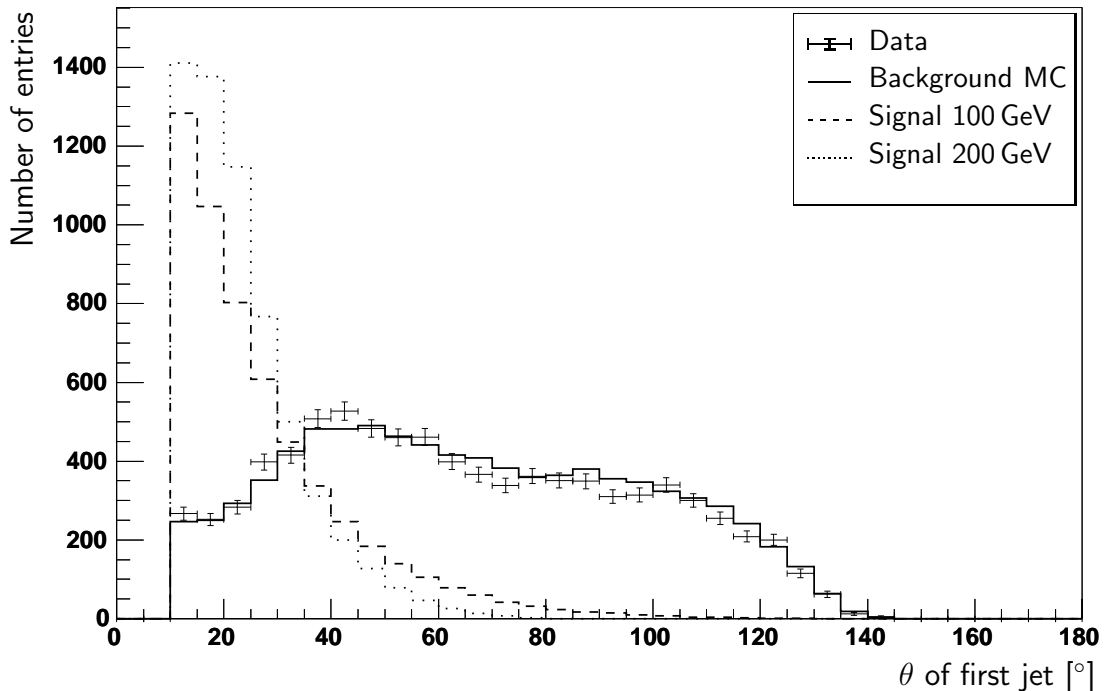


Figure 5.8:  $\theta$  of the first jet after preselection. The plot shows data, background MC and signal MC samples (scaled by an arbitrary factor).

for the jets can be derived. The hadronic reconstruction and calibration package hadroo2 has been used in this analysis for the hadronic calibration. More information on the package and a detailed description of the calibration method can be found in [42].

Figure 5.8 and Figure 5.9 show the calibrated distributions of the variables  $\theta$  and energy  $E$  of the first jet after the application of the preselection on the different data sets. The distributions for the signal MC samples corresponding to excited quarks of  $m_{q^*} = 100$  GeV and  $m_{q^*} = 200$  GeV are shown as dashed and dotted lines scaled by an arbitrary factor. The background MC samples describe the data reasonably well. The jet as the decay product of the excited quark decay is dominantly pointing into the forward region of the detector and has a large transverse energy. In contrary the NC background events are distributed almost equally in  $\theta$  but show a rapidly falling energy spectra. Therefore the energy of the first jet is used to discriminate the signal events from the background sources in the further selections.

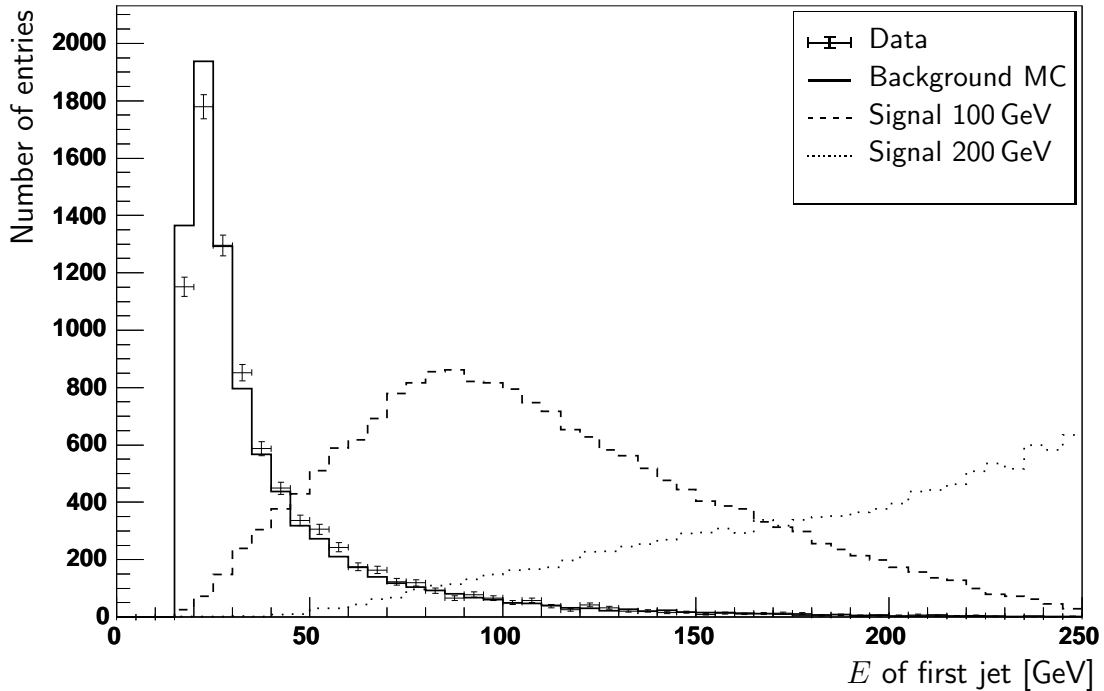


Figure 5.9: *Energy of the first jet after preselection. The plot shows data, background MC and signal MC samples (scaled by an arbitrary factor).*

## 5.5 Final Selection

This section describes the final selections applied on top of the preselection to separate the signal most efficiently from the different background sources. The different variables and cuts are introduced and examined separately. The combi-

nation of all cuts is discussed afterwards. A comparison to the latest H1 publication is described in Section 5.5.4.

### 5.5.1 Cuts on electromagnetic particle variables

The two variables  $p_T$  and  $\theta$  of the first electromagnetic particle are used to discriminate the signal from the background events. Figure 5.10 and Figure 5.11 show the efficiency of both cuts separately for signal MCs with different masses of the excited quark. The figures show as well the background rejection efficiency for the sum of all background MCs. The final cut on the different variables is marked in each plot. The shape of the  $p_T$  and  $\theta$  distributions have already been shown in the Figure 5.7 and Figure 5.6. The peak of the  $p_T$  distribution of the signal samples can be found at a  $p_T$  value of around half of the mass of the generated quark and shifts linearly with the generated mass of the excited quark to higher values. Therefore the cut on this variable effects the signal samples with the lowest generated masses the most. Table 5.3 shows the efficiencies for the  $p_T$  and  $\theta$  cut individually and combined with respect to the preselection described in the previous section. A cut of  $p_T > 40$  GeV has been chosen to reduce the background most efficiently with minimal losses in the signal samples. Due to the high energies of the photon in the excited quark decay the photon can be found dominantly in the forward region of the detector. The shape of the  $\theta$  distribution does not vary much for different masses. Hence a cut can be chosen with good

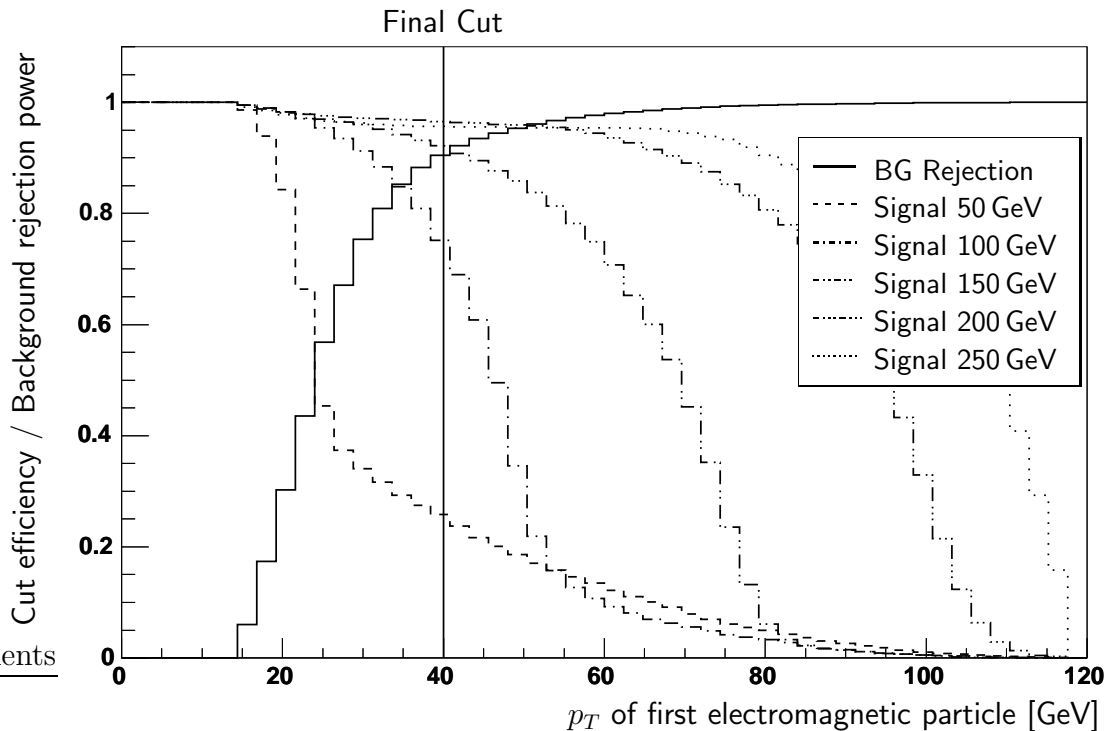


Figure 5.10: *Cut Efficiency and background rejection power of cut on  $p_T$  of the first electromagnetic particle. The value of the final cut on this variable is marked in the plot as a vertical solid line.*

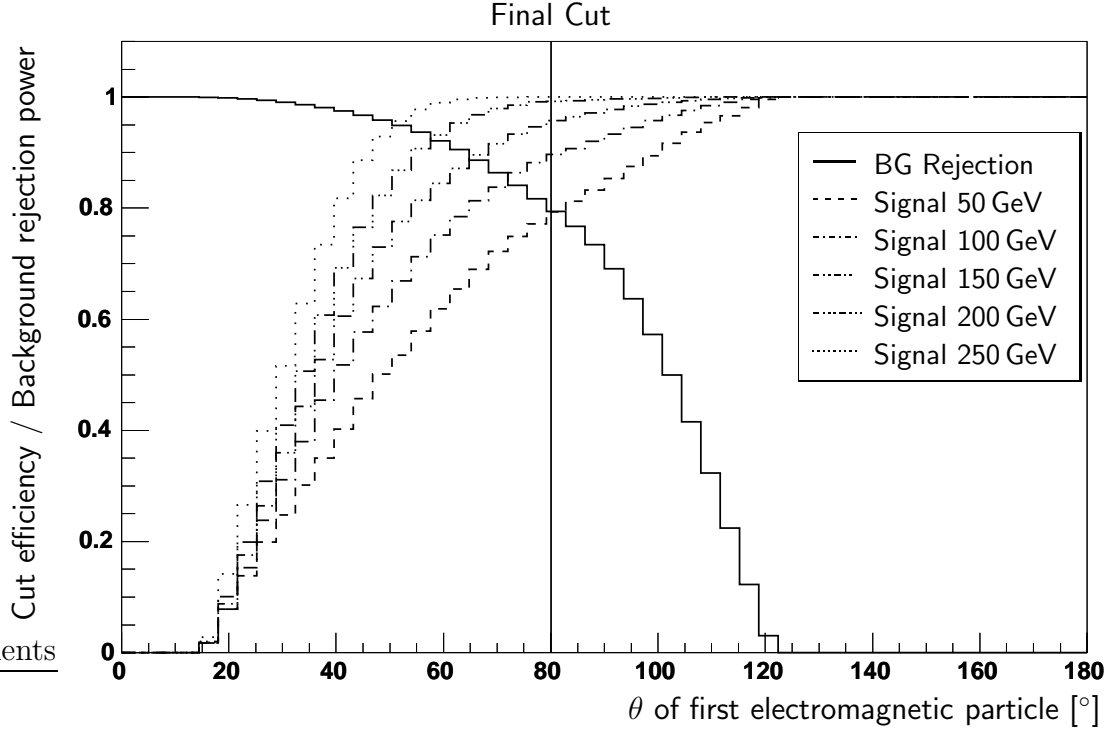


Figure 5.11: Cut efficiency and background rejection power of cut on  $\theta$  of the first electromagnetic particle. The value of the final cut on this variable is marked in the plot as a vertical solid line.

acceptance for all masses. A cut of  $\theta < 80^\circ$  allows a good background rejection with a signal acceptance of more than 80%. Figure 5.12 shows the  $\theta$  distributions after the cut on  $p_T > 40$  GeV, 5.13, respectively, the  $p_T$  distributions after the

	Cut efficiency [%]		
	$\theta < 80^\circ$ cut	$p_T > 40$ GeV cut	$\theta$ and $p_T$ cut
Data	$23.6 \pm 0.4$	$11.5 \pm 0.3$	$8.8 \pm 0.3$
NC Background	$20.9 \pm 0.4$	$10.2 \pm 0.3$	$7.8 \pm 0.3$
Photoproduction BG	$87.0 \pm 1.8$	$3.2 \pm 1.0$	$3.1 \pm 1.0$
Signal ( $m_{q^*} = 50$ GeV)	$89.2 \pm 0.2$	$3.3 \pm 0.1$	$3.1 \pm 0.1$
Signal ( $m_{q^*} = 75$ GeV)	$88.6 \pm 0.1$	$13.9 \pm 0.2$	$13.8 \pm 0.2$
Signal ( $m_{q^*} = 100$ GeV)	$89.4 \pm 0.1$	$73.2 \pm 0.2$	$72.2 \pm 0.2$
Signal ( $m_{q^*} = 125$ GeV)	$91.9 \pm 0.1$	$87.5 \pm 0.1$	$85.8 \pm 0.1$
Signal ( $m_{q^*} = 150$ GeV)	$94.2 \pm 0.1$	$93.6 \pm 0.1$	$91.9 \pm 0.1$
Signal ( $m_{q^*} = 175$ GeV)	$96.3 \pm 0.1$	$96.7 \pm 0.1$	$95.3 \pm 0.1$
Signal ( $m_{q^*} = 200$ GeV)	$98.0 \pm 0.1$	$98.5 \pm 0.1$	$97.3 \pm 0.1$
Signal ( $m_{q^*} = 225$ GeV)	$99.0 \pm 0.1$	$99.3 \pm 0.1$	$98.7 \pm 0.1$
Signal ( $m_{q^*} = 250$ GeV)	$99.6 \pm 0.1$	$99.6 \pm 0.1$	$99.3 \pm 0.1$

Table 5.3: Cut efficiencies for different cuts on variables of the first electromagnetic particle with respect to the preselection.

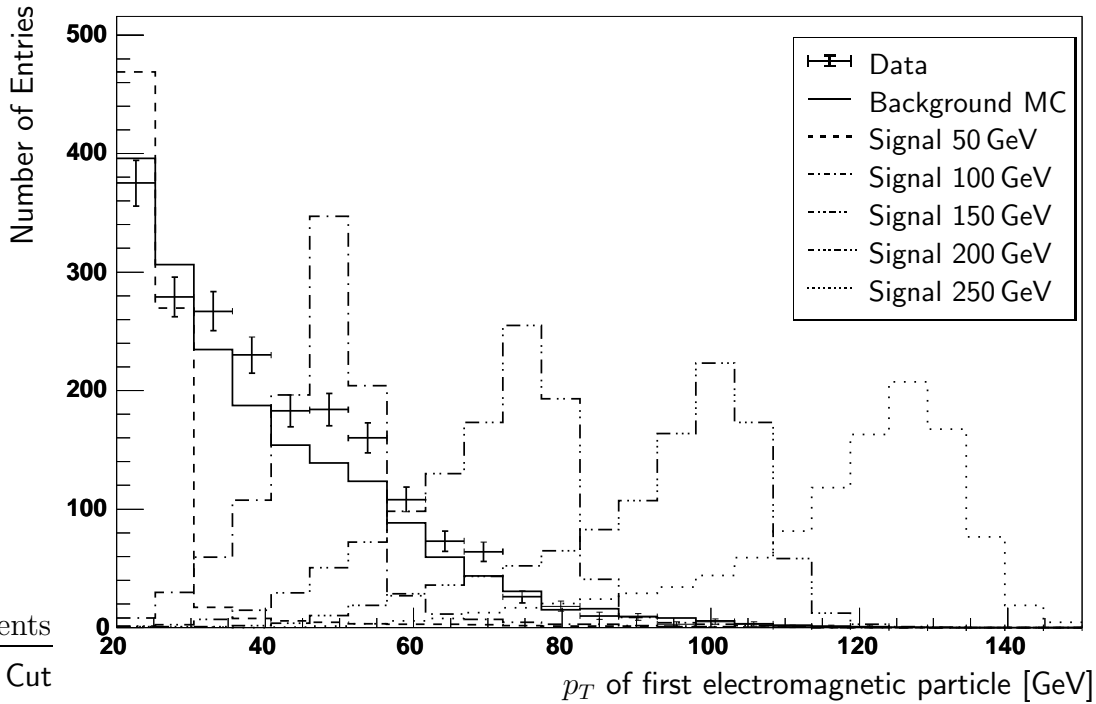


Figure 5.12:  $p_T$  of first electromagnetic particle after final cut on  $\theta$  of first electromagnetic particle. The plot shows data, background MC and signal MC samples (scaled by an arbitrary factor).

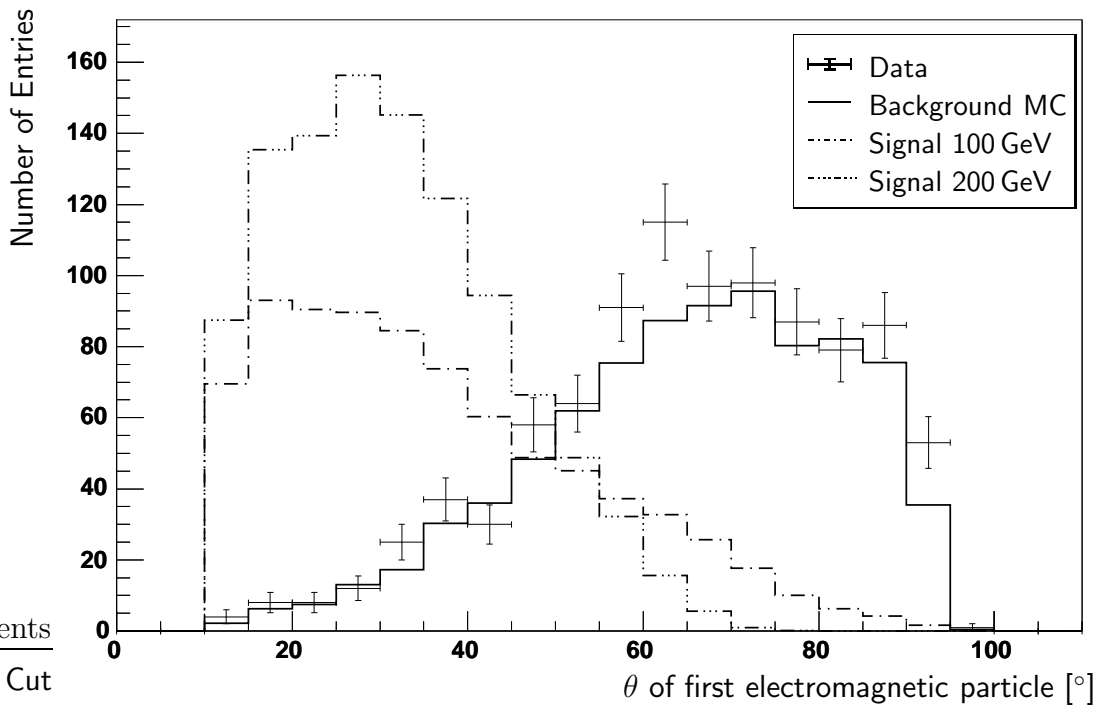


Figure 5.13:  $\theta$  of first electromagnetic particle after final cut on  $p_T$  of first electromagnetic particle. The plot shows data, background MC and signal MC samples (scaled by an arbitrary factor).

cut on  $\theta < 80^\circ$ . In all figures the distributions of the signal samples are scaled to an arbitrary value to make the figures best readable. The data sample after the individual cuts is still described sufficiently by the background MC samples. From Table 5.3 one can derive that this analysis is not sensitive to masses below 100 GeV. This region has already been ruled out by other experiments [43].

### 5.5.2 Cuts on jet variables

The energy of the first jet is used to further discriminate the signal from the background events. The shape of the energy distribution of the first jet has already been shown in the Figure 5.9. Figure 5.14 shows the distance between the first jet and the first electromagnetic particle in  $\phi$  and  $\theta$  for the data sample, the background MC samples and two selected signal MC samples. One can see very good the difference between the signature in the signal and the data. In the signal sample the distribution of the distance in  $\theta$  and  $\phi$  is very sharp meaning that the jet and the photon have nearly the same  $\theta$  value and are back-to-back in  $\phi$ . This is clear because both the jet and the photon are decay products of the excited quark having an initial momentum. In contrast to the signal the background MC and the data show no pronounced correlation in  $\theta$ . The jet and the photon candidate are well separated in  $\phi$  also for the background events which eases the jet-photon discrimination.

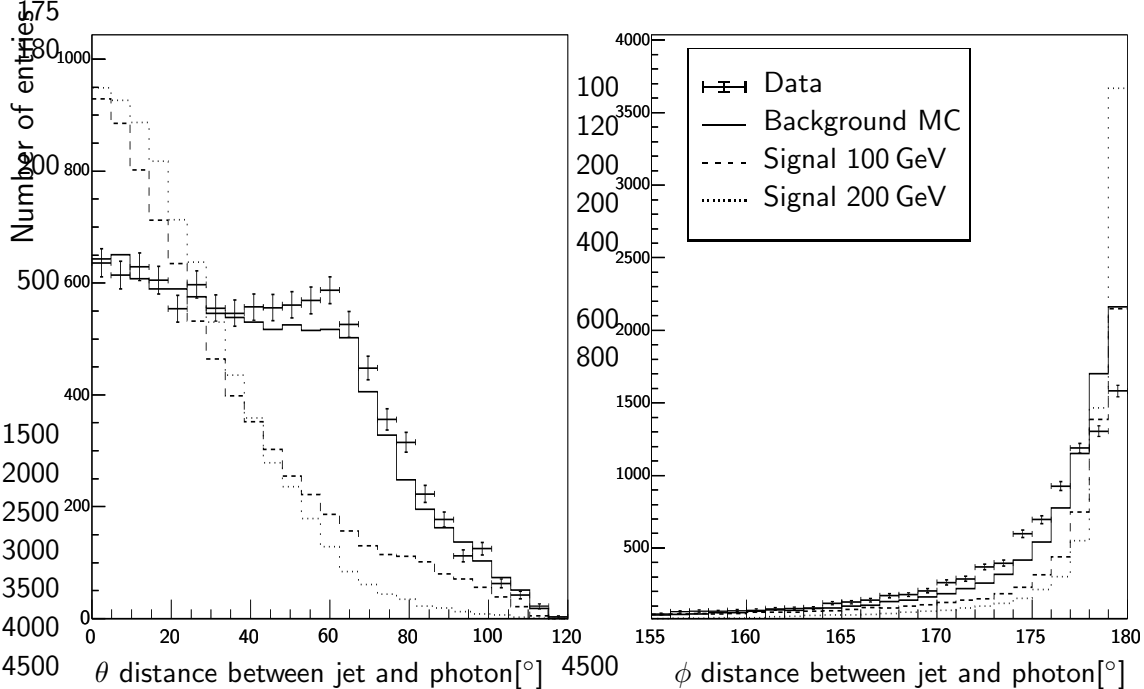


Figure 5.14: Distance between first jet and first electromagnetic particle in variables  $\theta$  and  $\phi$ . The plot shows data, background MC and signal MC samples (scaled by an arbitrary factor).

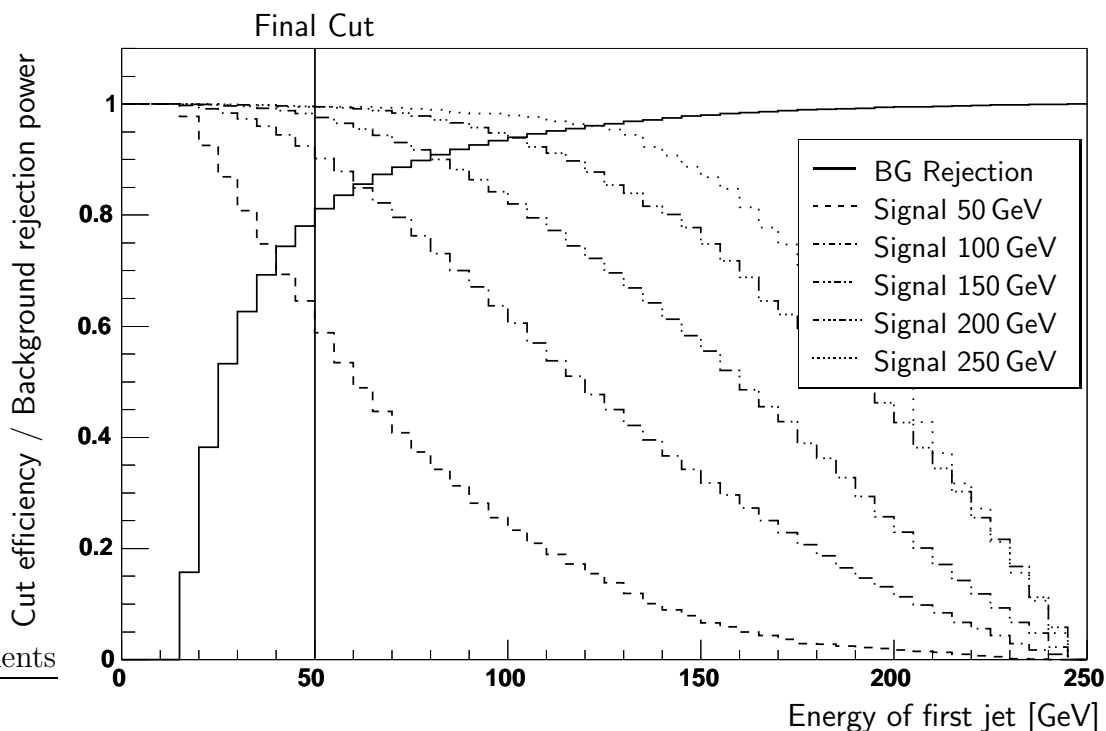


Figure 5.15: *Cut efficiency and background rejection power of cut on the energy of the first jet with respect to the preselection. The value of the final cut on this variable is marked in the plot as a vertical solid line.*

Figure 5.15 shows the efficiency of the jet energy cut for signal MCs with different masses of the excited quark. The figure shows as well the background rejection efficiency for the sum of all background MCs. The final cut on the different variables is marked in the plot. A cut of  $E > 50$  GeV was chosen. Figure 5.15 shows the cut efficiency of the jet energy cut with respect to  $\theta_{em}$  of the first electromagnetic particle and Table 5.4 shows the efficiencies for the energy cut with respect to the preselection and with respect to the combined cuts on the electromagnetic particle variables. With respect to the preselection the jet energy cut would reject roughly 75% of the remaining background events while keeping more than 85% of the signal. Because of the jet energy cut not being independent from the cuts on the electromagnetic particle the cut rejects about 20% of the background events in addition to the previous applied electromagnetic particle cuts.

Figure 5.17 and Figure 5.18 show the energy and  $\theta$  distribution of the first jet after the cut on  $E > 50$  GeV and the previous cuts on the variables of the electromagnetic particles. In all figures the distributions of the signal samples are scaled to an arbitrary value to make the figures best readable. The data is described by the background MC samples reasonably well with the data generally lying a few percent above the background samples but within the range of possible structure function errors. An excess of data in regions where the signal would have been expected can not be found.

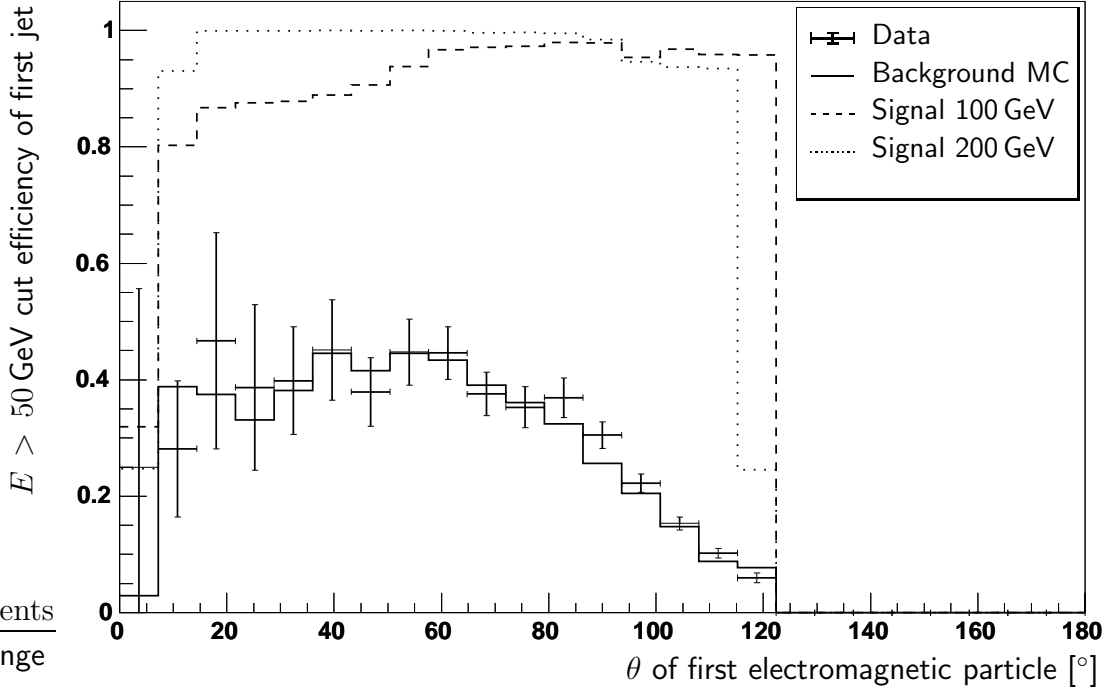


Figure 5.16: Cut efficiency of jet energy cut with respect to  $\theta$  of first electromagnetic particle. The plot shows data, background MC and signal MC samples (scaled by an arbitrary factor).

	$E > 50$ cut efficiency [%] with respect to	
	preselection	em particle cuts
Data	$22.7 \pm 0.5$	$78.1 \pm 1.5$
NC Background	$20.7 \pm 0.5$	$80.2 \pm 1.6$
Photoproduction BG	$29.6 \pm 3.0$	$78.8 \pm 13.5$
Signal ( $m_{q^*} = 50$ GeV)	$51.9 \pm 0.3$	$71.9 \pm 1.4$
Signal ( $m_{q^*} = 75$ GeV)	$77.6 \pm 0.2$	$82.7 \pm 0.5$
Signal ( $m_{q^*} = 100$ GeV)	$91.7 \pm 0.1$	$92.4 \pm 0.2$
Signal ( $m_{q^*} = 125$ GeV)	$96.5 \pm 0.1$	$96.8 \pm 0.1$
Signal ( $m_{q^*} = 150$ GeV)	$98.4 \pm 0.1$	$98.5 \pm 0.1$
Signal ( $m_{q^*} = 175$ GeV)	$99.4 \pm 0.1$	$99.5 \pm 0.1$
Signal ( $m_{q^*} = 200$ GeV)	$99.9 \pm 0.1$	$99.9 \pm 0.1$
Signal ( $m_{q^*} = 225$ GeV)	$99.9 \pm 0.1$	$99.9 \pm 0.1$
Signal ( $m_{q^*} = 250$ GeV)	$100.0 \pm 0.1$	$100.0 \pm 0.1$

Table 5.4: Efficiency for jet energy cut with respect to the preselection and with respect to the cuts on the electromagnetic particle variables.

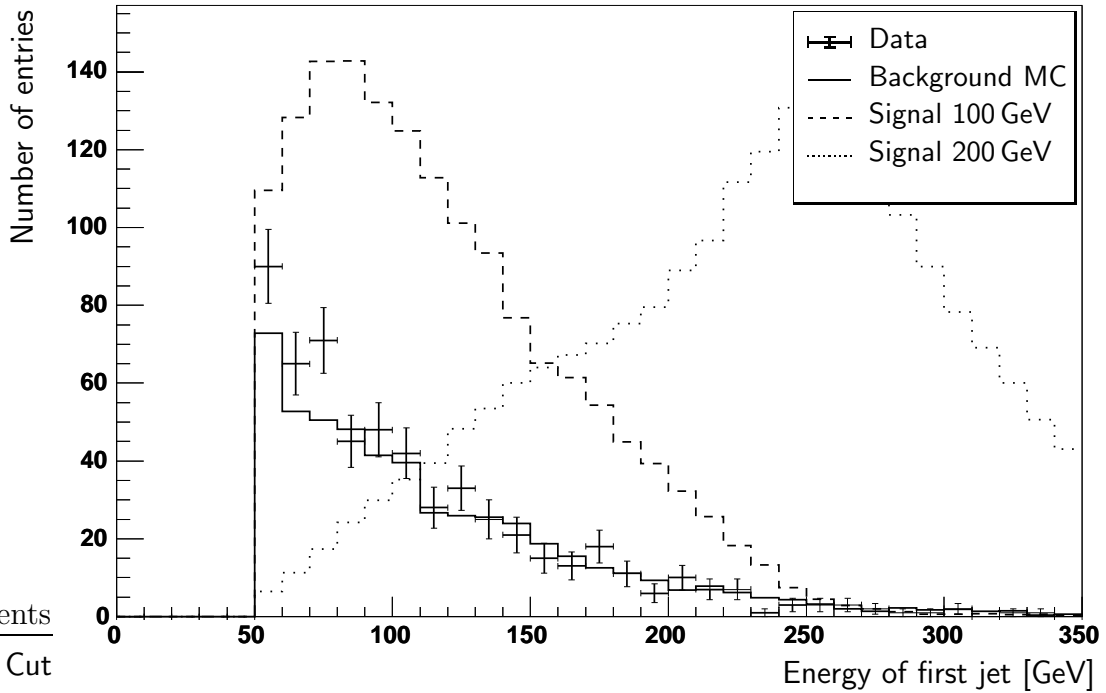


Figure 5.17: Energy of the first jet after cuts on first electromagnetic particle variables  $p_T$  and  $\theta$  and jet energy. The plot shows data, background MC and signal MC samples (scaled by an arbitrary factor).

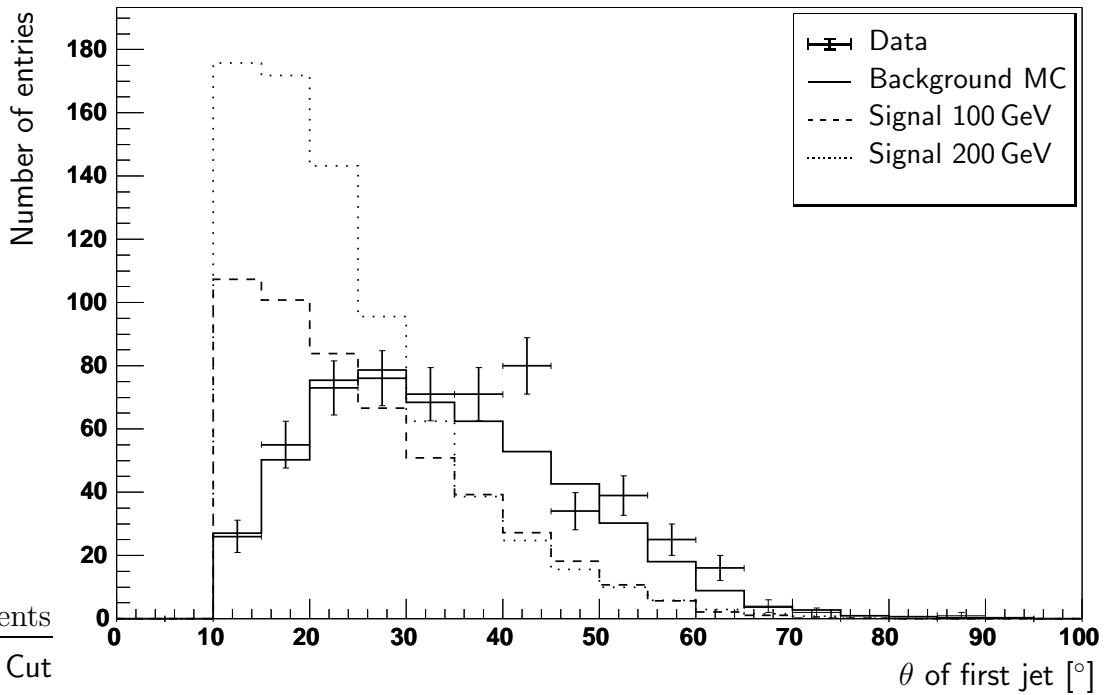


Figure 5.18:  $\theta$  of the first jet after cuts on first electromagnetic particle variables  $p_T$  and  $\theta$  and jet energy. The plot shows data, background MC and signal MC samples (scaled by an arbitrary factor).

### 5.5.3 Photon detection

The typical jet-photon signature of the signal events offers the possibility to further reduce the background by asking for a photon identification of the first electromagnetic particle by a veto on charged particles. The latter are identified by their tracking signature either a track measured in the central driftchambers (tracking cut) or a signal in the central proportional chamber (CIP cut). The track in the driftchamber is extrapolated to the LAr calorimeter surface and the minimal distance to the LAr cluster is measured for the tracking cut. Figure 5.19 shows this distribution together with the cut value of 10 cm. For the CIP cut a line between the interaction vertex and the LAr cluster is formed and the distance from this line to the nearest CIP hit is measured. Figure 5.20 shows this distribution of the cut variable together with the cut value of 5 cm.

Figure 5.21 shows the combination of both cuts with respect to  $\theta$  of the electromagnetic particle. The efficiency for the signal samples drops significantly for the region of  $\theta < 30^\circ$ . The tracking cuts have not been restricted in favour of the high background rejection power of the tracking cuts. The higher losses due to the reduced signal efficiencies in this regions of  $\theta$  tolerated. In certain run ranges parts of the tracking system were inefficient. These run periods have not been used for this analysis if the first electromagnetic particle would point to the inefficient areas in the azimuth angle  $\phi$ . For runs 257590 to 261338 the  $\phi$  range between  $190^\circ$  and  $280^\circ$  was cut out. Figure 5.22 shows the cut efficiency for the

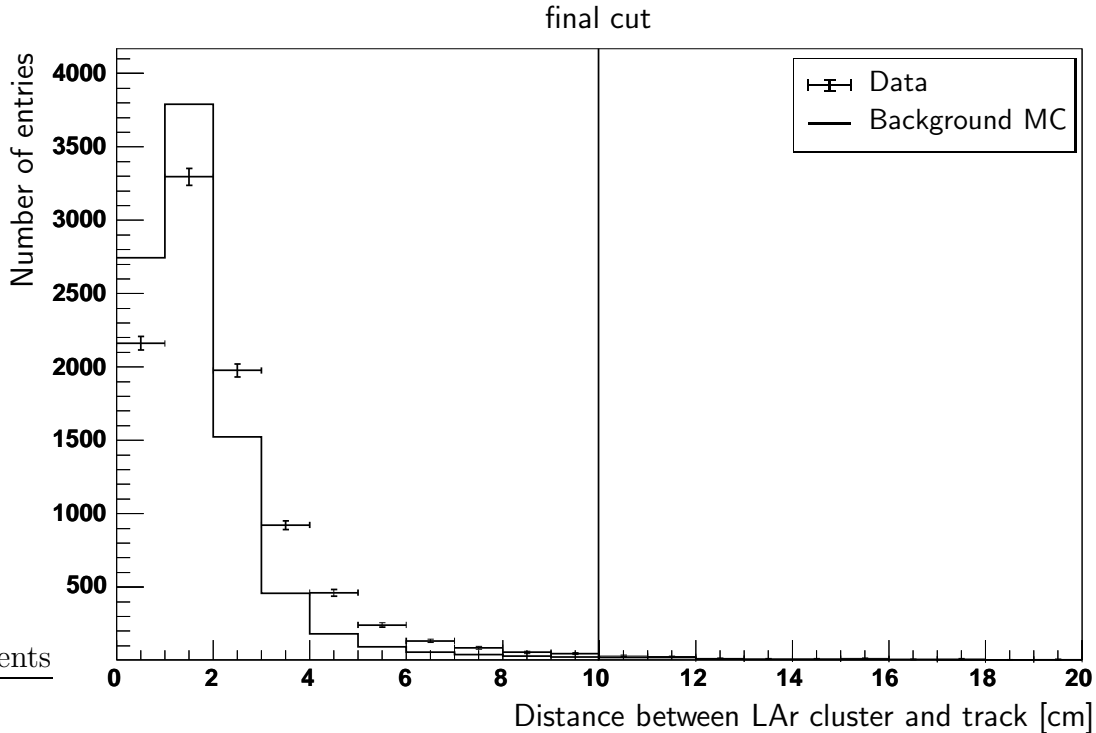


Figure 5.19: *Distance between LAr cluster and track after preselection. The plot shows data and background MC. The value of the final cut on this variable is marked in the plot as a vertical solid line.*

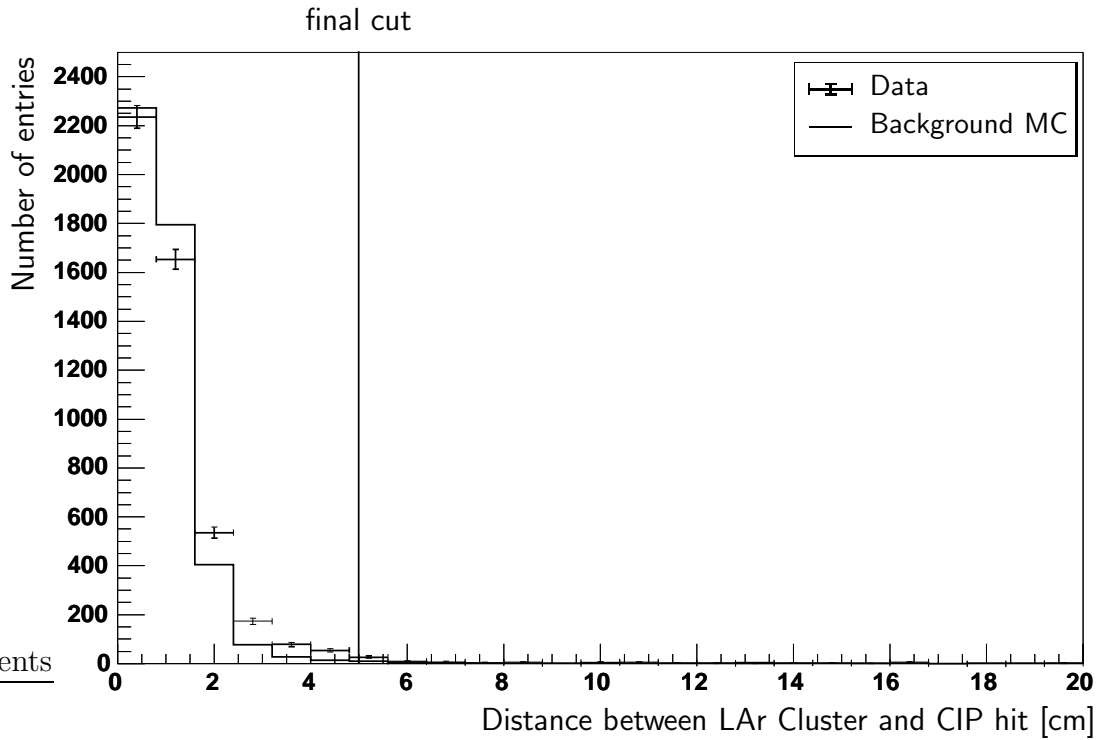


Figure 5.20: Distance between LAr cluster and CIP hit after preselection. The plot shows data and background MC. The value of the final cut on this variable is marked in the plot as a vertical solid line.

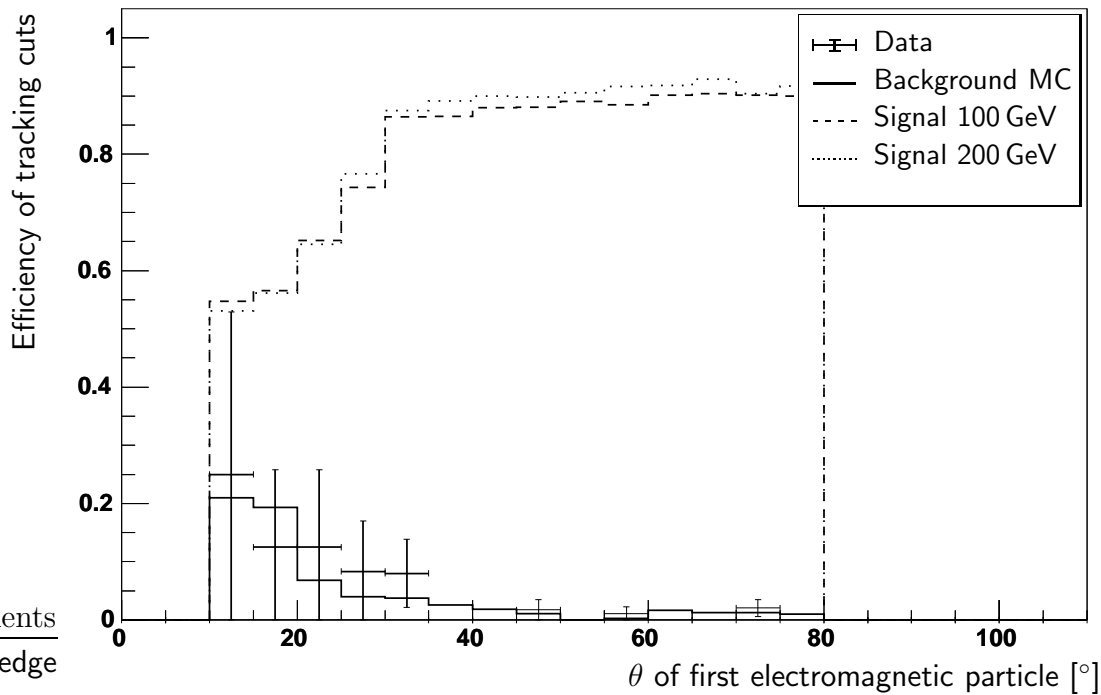


Figure 5.21: Tracking cuts efficiency with respect to  $\theta$  of first electromagnetic particle and with respect to all cuts on the electromagnetic particle variables. The plot shows data, background MC and signal MC samples.

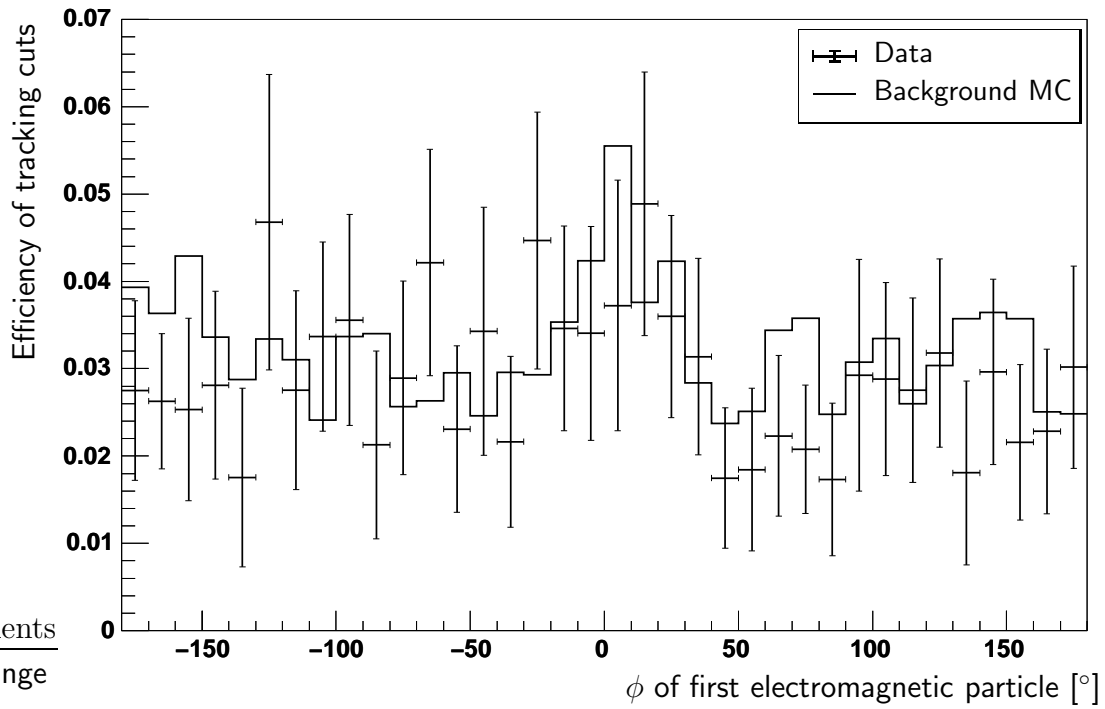


Figure 5.22: Tracking cuts efficiency with respect to  $\phi$  of first electromagnetic particle and with respect to the preselection. The plot shows data, background MC and signal MC samples.

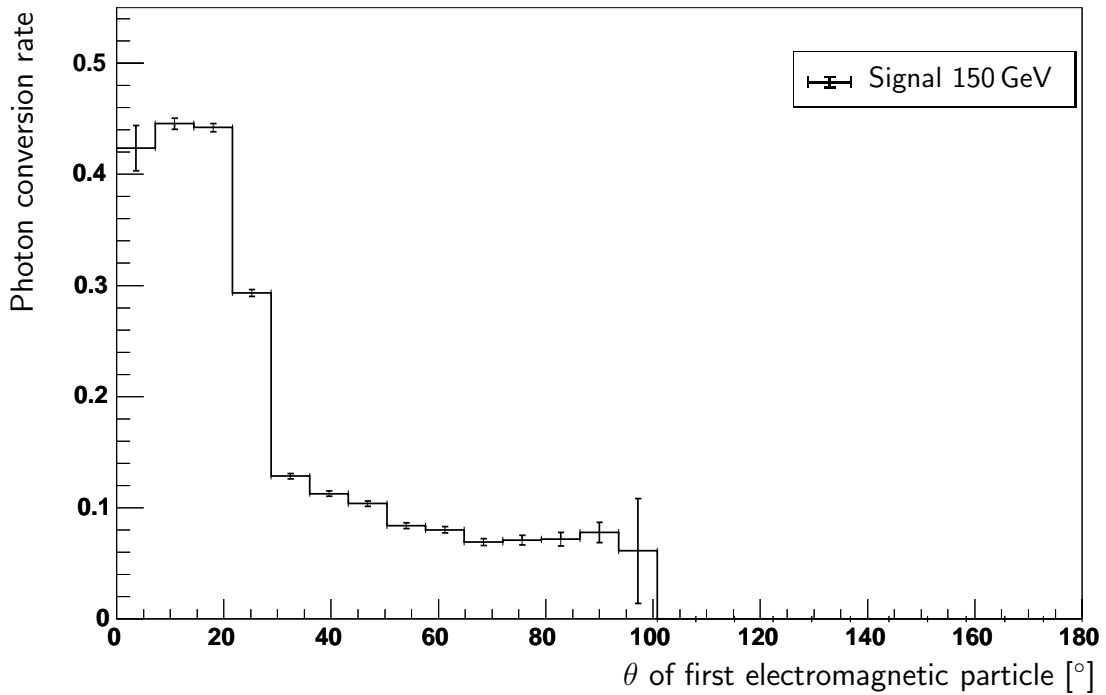


Figure 5.23: Photon conversion rate with respect to  $\theta$  of first electromagnetic particle derived from the 150 GeV signal sample.

	Cut Efficiency [%]		
	Tracking cut	CIP cut	combined cuts
Data	$1.8 \pm 0.6$	$51.5 \pm 2.1$	$1.2 \pm 0.5$
NC Background	$1.7 \pm 0.6$	$50.7 \pm 2.2$	$1.0 \pm 0.5$
Photoproduction BG	$65.5 \pm 16.1$	$90.2 \pm 13.2$	$61.1 \pm 16.3$
Signal ( $m_{q^*} = 50$ GeV)	$14.0 \pm 1.3$	$56.0 \pm 1.8$	$13.2 \pm 1.3$
Signal ( $m_{q^*} = 75$ GeV)	$65.3 \pm 0.6$	$87.8 \pm 0.5$	$63.5 \pm 0.7$
Signal ( $m_{q^*} = 100$ GeV)	$79.0 \pm 0.2$	$94.7 \pm 0.2$	$77.1 \pm 0.3$
Signal ( $m_{q^*} = 125$ GeV)	$80.3 \pm 0.2$	$95.0 \pm 0.1$	$78.5 \pm 0.2$
Signal ( $m_{q^*} = 150$ GeV)	$80.8 \pm 0.2$	$95.3 \pm 0.1$	$79.0 \pm 0.2$
Signal ( $m_{q^*} = 175$ GeV)	$80.2 \pm 0.2$	$95.3 \pm 0.1$	$78.4 \pm 0.2$
Signal ( $m_{q^*} = 200$ GeV)	$78.4 \pm 0.2$	$95.4 \pm 0.1$	$76.9 \pm 0.2$
Signal ( $m_{q^*} = 225$ GeV)	$76.0 \pm 0.2$	$95.3 \pm 0.1$	$74.6 \pm 0.2$
Signal ( $m_{q^*} = 250$ GeV)	$73.8 \pm 0.2$	$95.2 \pm 0.1$	$72.3 \pm 0.2$

Table 5.5: *Efficiencies for tracking cuts with respect to previous cuts.*

combined cut with respect to the  $\phi$  variable of the electromagnetic particle and with respect to the preselection for the data and background MC sample. The data is described by the background MC within 0.5%. The difference is accounted for in the systematic error.

Signal losses due to the tracking cuts are mainly due to conversion of photons into charged particle pairs inside the detector producing tracks that are measured by the tracking system. Converted photons will of course not pass the photon selection criterias of the tracking and the CIP cut. Figure 5.23 shows the fraction of converted photons with respect to  $\theta$  of the first electromagnetic particle. The plot was derived from the MC signal sample with an excited quark mass of 150 GeV. In the central region of the detector the conversion rate is 6 - 8%. For photons going into the forward region of the detector the conversion rate raises, since there is more dead material like the electronics, supply tubes and readout cables of the central and forward detectors.

Table 5.5 shows the efficiency of the tracking cut, the CIP cut and the combination of both cuts with respect to the previous cuts applied on the electromagnetic particle variables and the jet variables. The cuts dominantly reduce the NC background with a good efficiency. Photoproduction background is not affected as much as the NC background by the cuts since the signal comes from a real photon (prompt photons) or neutral mesons faking a photon candidate. One can see a little decrease of the signal efficiency with higher masses since the photon points more into the forward region and the photon conversion has a bigger effect. The decrease of the efficiency for the lower masses under 100 GeV can be explained. Due to the hard cuts on  $p_T$  and  $\theta$  of the first electromagnetic particle and the cut on the energy of the first jet the remaining events are in a phase space where the photon and jet are not separated in the  $(\eta, \phi)$  plane as good

as the majority of the signal events before the cuts. In addition the radius of the jets are bigger than for jets with higher  $p_T$  in the samples with higher quark masses. The veto of the tracking cuts is very sensitive on tracks faked by the jet. The losses in the signal samples are of the order of 20% to 25% for masses higher than 100 GeV.

### 5.5.4 Final cuts and comparison to former H1 publication

The application of all cuts described in the prior sections gives the final number of data and background events found in the final sample and the selection efficiencies of the signal samples for the different masses. The data events after all cuts were visually scanned for evident background events. One event was clearly identified as a cosmic muon event surviving all prior cuts. Figure 5.24 shows the event display of this event with the event number 69526 and run number 254423.

The results of this analysis are compared to the latest H1 publication from July 2000 dealing with the general search for excited fermions at HERA [44]. The publication is based on the analysis carried out in the dissertation thesis [45]. Table 5.6 shows a summary of all final cuts for this analysis and in comparison the cuts made in the analysis of the publication. Compared to the publication the cuts of this analysis are harder for  $\theta$  and  $p_T$  of the first electromagnetic particle and the energy of the first jet. The tracking cuts have been chosen to be as loose as possible to avoid losses in the signal efficiency due to the strong dependency of the tracking veto cuts on the tracking efficiency of the detector.

In addition to the statistical errors of the data samples the following systematic errors have been taken in account for the background and the signal samples:

- An uncertainty on the absolute electromagnetic energy scale ranging from  $\pm 0.7\%$  in the central part of the LAr calorimeter to  $\pm 3\%$  in the forward part.
- An uncertainty of the  $\theta$  measurement of the electromagnetic particles of  $\pm 0.3\%$ .

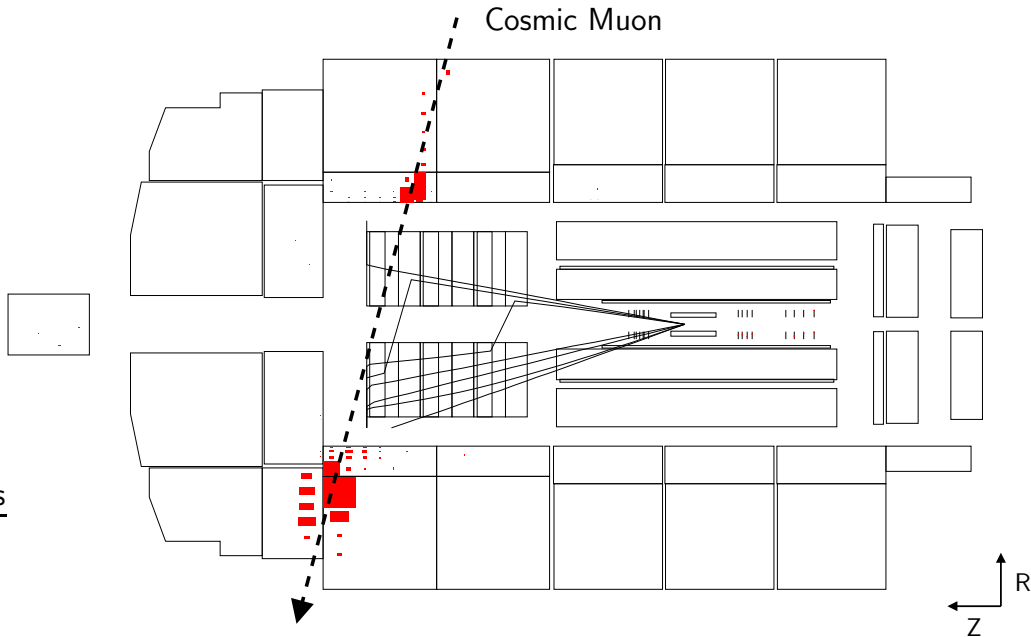


Figure 5.24: Event display of cosmic muon filtered out by visual scan. The event number is 69526. The run number is 254423

Cut	This Analysis	Latest H1 publication
$\theta$ of em particle	$10^\circ < \theta_{em} < 80^\circ$	$10^\circ < \theta_{em} < 90^\circ$
$p_T$ of em particle	$p_T > 40 \text{ GeV}$	$p_T > 20 \text{ GeV}$
$E(E_T)$ of first jet	$E > 50 \text{ GeV}$	$E_T > 15 \text{ GeV}$
$\theta$ of first jet	$\theta_{jet} > 10^\circ$	$\theta_{jet} > 10^\circ$
$E_T$ of second jet	no cut	$E_T < 15 \text{ GeV}$
Tracking cut	$\Delta(\text{Track}, \text{LArCl}) > 10 \text{ cm}$	$\Delta(\text{Track}, \text{LArCl}) > 40 \text{ cm}$
CIP cut	$\Delta(\text{CIP}, \text{LArCl}) > 5 \text{ cm}$	$\Delta(\text{CIP}, \text{LArCl}) > 10 \text{ cm}$
$E_T$ of second em particle	no cut	no electron with $E_T > 5 \text{ GeV}$ in LAr

Table 5.6: Comparison of cuts between this analysis and the latest H1 publication.

- An uncertainty of  $\pm 4\%$  on the energy of the jets due to the uncertainty on the calibration of the calorimeters for hadronic showers.
- An uncertainty of  $0.5\%$  on the tracking efficiency of the electromagnetic particles.
- An uncertainty of  $7\%$  on the predicted DIS cross-sections for the MC generators coming mainly from the lack of knowledge on the proton structure.
- An overall systematic error of  $2\%$  on the luminosity measurement.

Table 5.7 shows the final number of events for the data and the background samples for this analysis in comparison to the latest publication. The statistical and the systematic errors are shown separately. The systematic errors have been calculated by shifting the values of the the energy and  $\theta$  of the electromagnetic particle and the jet separately in the stated error intervals and running through

Sample	Final Number of Events		
	This Analysis		H1 Publication
Data	7	$\pm 2.7$ (stat)	35
Neutral Current BG	4.8	$\pm 0.3$ (stat) $\pm 2.9$ (syst)	2.5
Photoproduction BG	3.7	$\pm 0.2$ (stat) $\pm 0.7$ (syst)	33.5
Background Sum	8.5	$\pm 0.4$ (stat) $\pm 3.0$ (syst)	$36 \pm 5$
Luminosity [ $\text{pb}^{-1}$ ]	63		37

Table 5.7: Comparison of final data and background events for this analysis and the latest H1 publication

$M_{q^*}$ [GeV]	Selection Efficiency [%]	
	This Analysis	H1 Publication
50	$0.1 \pm 0.1$	22
75	$3.8 \pm 2.1$	33
100	$31.4 \pm 0.7$	36
125	$40.4 \pm 0.3$	–
150	$44.5 \pm 0.2$	42
175	$46.6 \pm 0.4$	–
200	$42.2 \pm 0.9$	41
225	$39.8 \pm 0.9$	–
250	$37.1 \pm 1.3$	40

Table 5.8: Comparison of selection efficiencies for this analysis and the latest H1 publication for the different mass samples.

the whole analysis chain. The remaining error sources have been taken into account on top of these results of the shifted analysis. All systematic errors have bin added in quadrature. Table 5.8 shows the signal selection efficiencies for the different mass samples used in this analysis. As stated before for this analysis

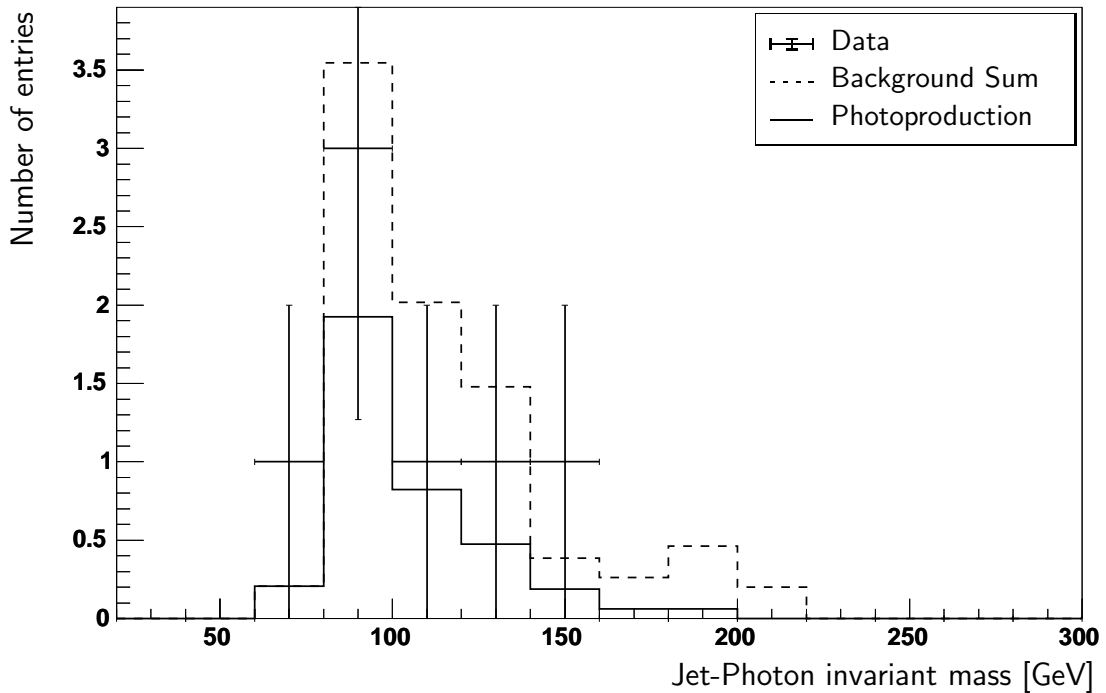


Figure 5.25: Invariant Mass calculated from Jet and Photon. The plot shows data, sum of background and the photoproduction background.

it was chosen to apply very hard cuts which have a very good background rejection power and still a good signal efficiency for high masses but leave the analysis insensitive to masses below 100 GeV. The systematic error for the neutral current background sample is very high due to the systematic error of the tracking efficiency.

Figure 5.25 shows the distribution of the invariant mass of the jet and the photon calculated from the four vectors of the jet and the designated photon. No evidence for a signal of an excited quark decay can be seen in this distribution. Therefore, upper limits on the production cross-section of the excited quarks have been derived as explained and shown in the next chapter.

In comparison to the results of the recent H1 publication the background after the final cuts in this analysis has a different composition. The dominating background source in the H1 publication is photoproduction background. It is almost removed in this analysis by the hard cut on  $p_T$  of the electromagnetic particle. This restricts the results of this analysis to masses larger than 100 GeV because of the drop in the signal efficiency for the lower masses.

Figure 5.28 shows the distribution of the missing transverse momentum of the event. The incoming particles have in leading order no transverse momentum therefore the measured missing transverse momentum should be zero if all particles are detected. Charged current events with an outgoing neutrino do have a missing transverse momentum corresponding to the momentum of the neutrino. The distribution of the missing  $p_T$  after the preselection and after the final cuts peaks at low momentum. The data is well described by the chosen background

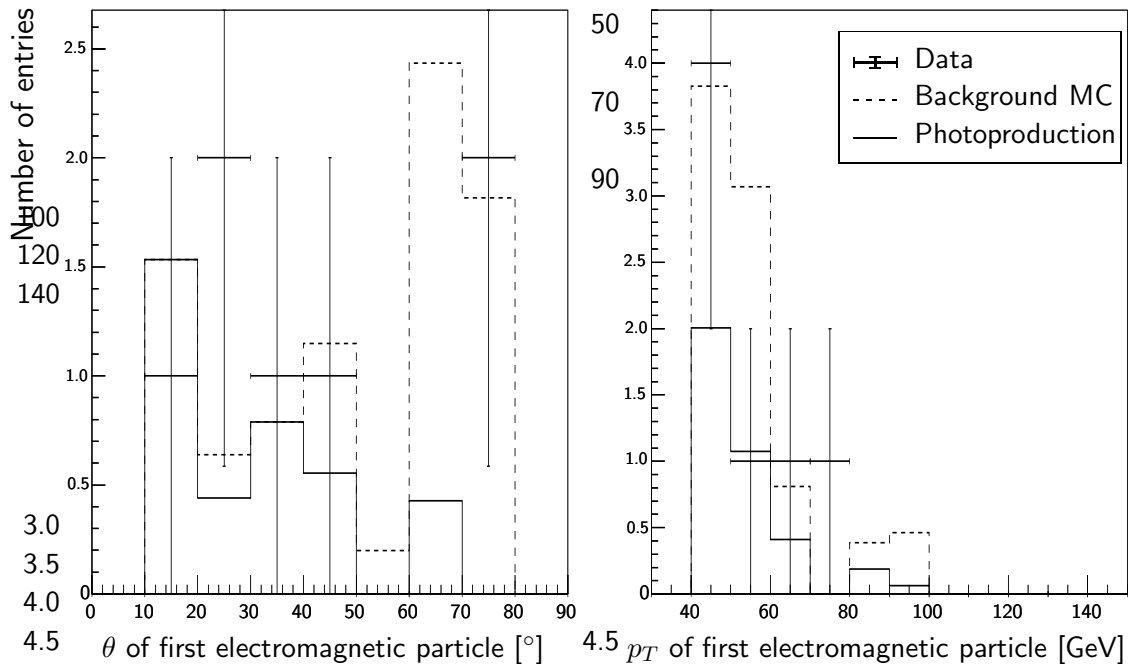


Figure 5.26:  $\theta$  and  $p_T$  of first electromagnetic particle after final selection. The plot shows data, sum of background and the photoproduction background.

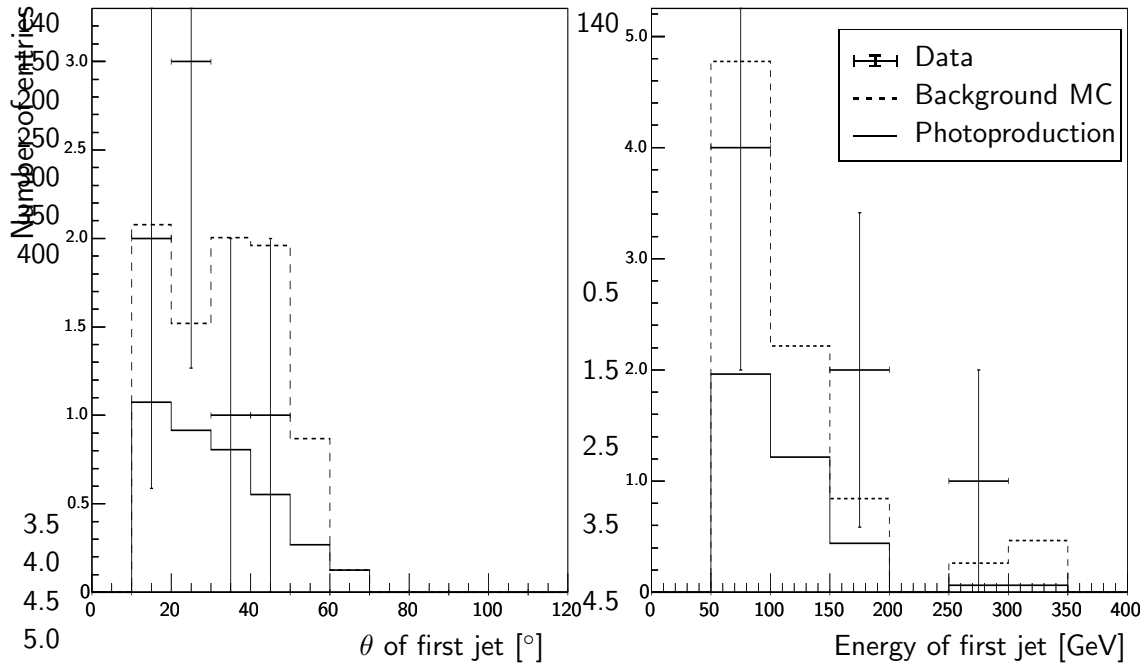


Figure 5.27:  $\theta$  and energy of first jet after final selection. The plot shows data, sum of background and the photoproduction background.

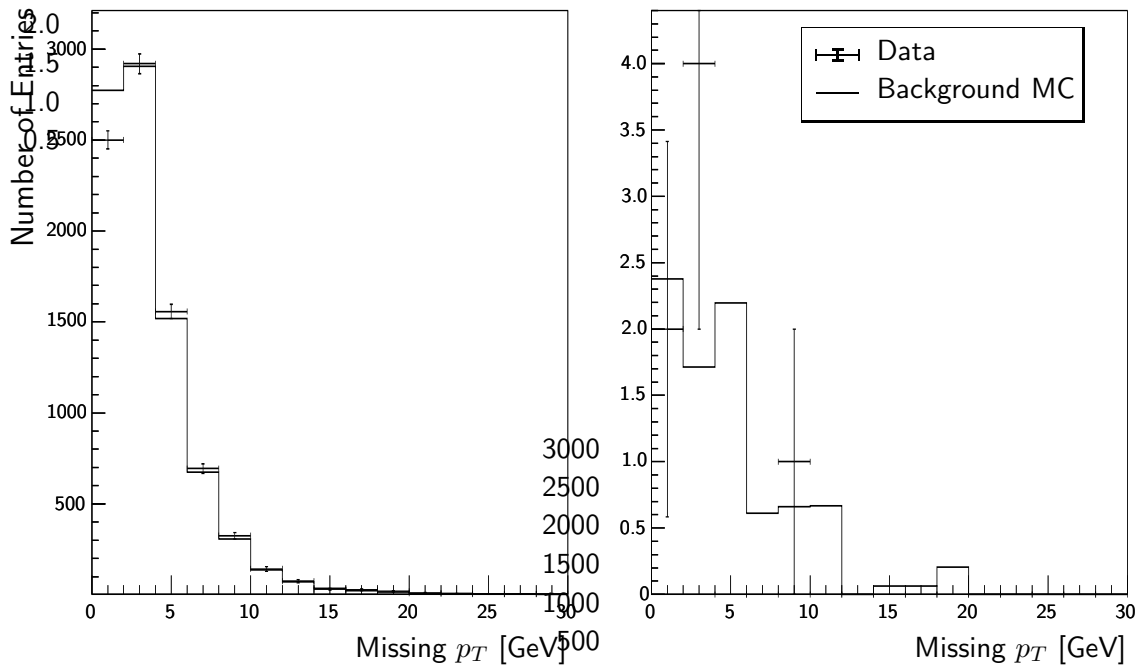


Figure 5.28: Distribution of missing  $p_T$  after preselection (left) and final selection (right). The plot shows data and background MC.

MC composition. There is no evidence for a significant contribution of radiative charged current events which have been neglected in the beginning. Figure 5.26 and Figure 5.27 show the distribution of  $\theta$  and  $p_T$  splitted into neutral current and photoproduction background after the final cuts. In all distributions the data is described by the background MC sets. One can clearly see the different dominating background sources in  $\theta$  of the first electromagnetic particle. For low  $\theta$  values the photoproduction background is dominant while for higher  $\theta$  values the neutral current background dominates.

# Chapter 6

## Limits on the production of Excited Quarks

### 6.1 Introduction to limit calculations

The problem of combining the results of several search channels for new particles is very complex. This analysis makes use of only one dedicated decay channel. But in the following the general case of  $n$  channels using a modified frequentist approach based on the Likelihood Ratio is introduced which of course is broken down to  $n = 1$  in case of this analysis. The implementation used in this analysis is described in [46]. In the following only the basic concepts are summarised.

#### 6.1.1 Likelihood Ratio

To discriminate signal-like outcomes from background-like outcomes of a search with  $n$  independent channels you have to define a test statistic  $X$ . It has been shown in various analysis that the Likelihood Ratio is a good choice for such a test statistic [47]. The Likelihood Ratio is defined for each channel as the probability of observing exactly that outcome, assuming a signal + background (s + b) hypothesis and the background-only hypothesis. If  $N$  is the total number of signal events, the expected number of signal events in the selection channel  $i$  is given by  $s_i = N \cdot (\epsilon\beta)_i$  where  $(\epsilon\beta)_i$  is the total visible branching ratio of the selection channel. With  $b_i$  being the estimated background, and  $d_i$  being the number of candidate events, the Likelihood Ratio of this selection channel is given by:

$$X_i = \frac{e^{s_i+b_i}(s_i + b_i)^{d_i}}{d_i!} / \frac{e^{-b_i}b_i^{d_i}}{d_i!} \quad (6.1)$$

For a set of  $n$  channels the Likelihood Ratio is given by the product of the ratios of the independent channels:

$$X = \prod_{i=1}^n X_i \quad (6.2)$$

This choice of the test statistic can be used to determine confidence levels (CL).

### 6.1.2 Confidence levels

By definition the CL for excluding the possibility of simultaneous presence of signal and background is the probability that the test statistic would be less than or equal to that observed in the data. This probability is given by a sum of Poisson probabilities:

$$CL_{s+b} = P_{s+b}(X \leq X_{\text{obs}}) = \sum_{X(\{d'_i\}) \leq X(\{d_i\})} \prod_{i=1}^n \frac{e^{-(s_i+b_i)}(s_i+b_i)^{d'_i}}{d'_i!} \quad (6.3)$$

where  $X(\{d_i\})$  is the test statistic for the observed set of candidates in each channel  $\{d_i\}$ . The sum runs over all possible final outcomes  $\{d'_i\}$  which lead to a test statistic less than or equal to the observed one. To quote exclusion limits  $1 - CL_{s+b}$  could be used, but it has the property that a search with downward fluctuating background will set strong exclusion limits, simply because the observed outcome was determined to be unlikely in any case. To correct for this effect the  $CL$  for the background alone must be calculated. It is given by:

$$CL_b = P_b(X \leq X_{\text{obs}}) \quad (6.4)$$

where the probability sum is computed assuming the presence of the background only. This  $CL$  expresses the probability that background processes would give fewer than or equal to the number of candidates observed. Then the  $CL$  of the modified frequentist approach can be computed by:

$$CL_s = CL_{s+b}/CL_b \quad (6.5)$$

This  $CL$  is used to set exclusions limits. An upper limit  $N_{lim}$  on the number of signal events is set such that  $CL_s \leq 0.05$  for  $N \geq N_{lim}$ . Systematic uncertainties on signal and background are taken into account by averaging over possible values of the signal and background assuming a Gaussian distribution, with the lower tail cut off at zero. For more details of the computation see [46].

## 6.2 Upper limits on cross-sections

The upper limit  $N_{lim}$  on the number of events coming from an excited quark decay can be calculated at a given  $CL$  using the modified frequentist approach. The following quantities enter this limit calculation:

- The number of events observed in the data. The number of events are integrated within a mass bin around the calculated mass of the excited

quark. The optimal mass window for the integration was derived from the extrapolation of the optimal mass window for the different generated excited quark masses. The optimal mass window for each excited quark mass was derived from the width of the invariant mass distribution. Figure 6.1 shows the mass windows for the generated masses and the extrapolated window ranges.

- The corresponding number of events expected from the SM background processes with the mass window ranges applied.
- The signal efficiencies for the different excited quark masses. The distribution of the efficiencies has been approximated as linear inbetween the different data points.
- The uncertainties on the signal efficiencies and the number of background events discussed in Section 5.5.4.

$N_{\text{lim}}$  is then translated into the limit on the cross-section of the whole process of the excited quark production and the decay into a photon and a quark:

$$(\sigma \times BR)_{\text{lim}} = \frac{N_{\text{lim}}}{\mathcal{L}} \quad (6.6)$$

with  $BR$  being the branching ratio of the process. In this case of the dedicated

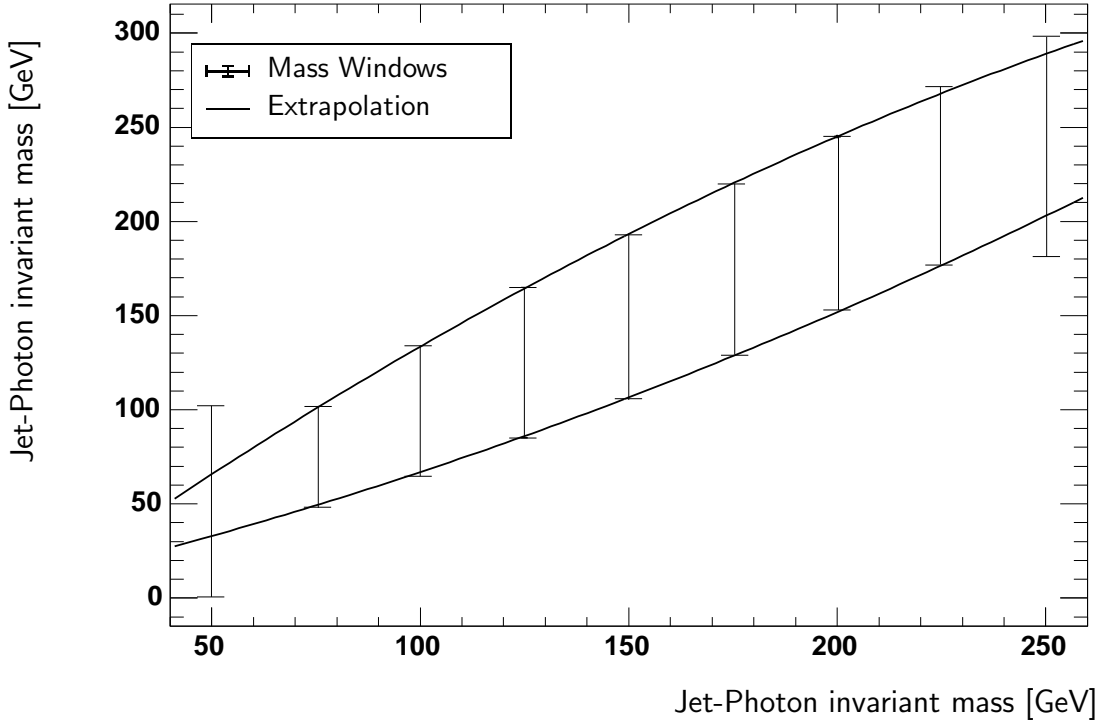


Figure 6.1: *Extrapolation of optimal mass windows.*

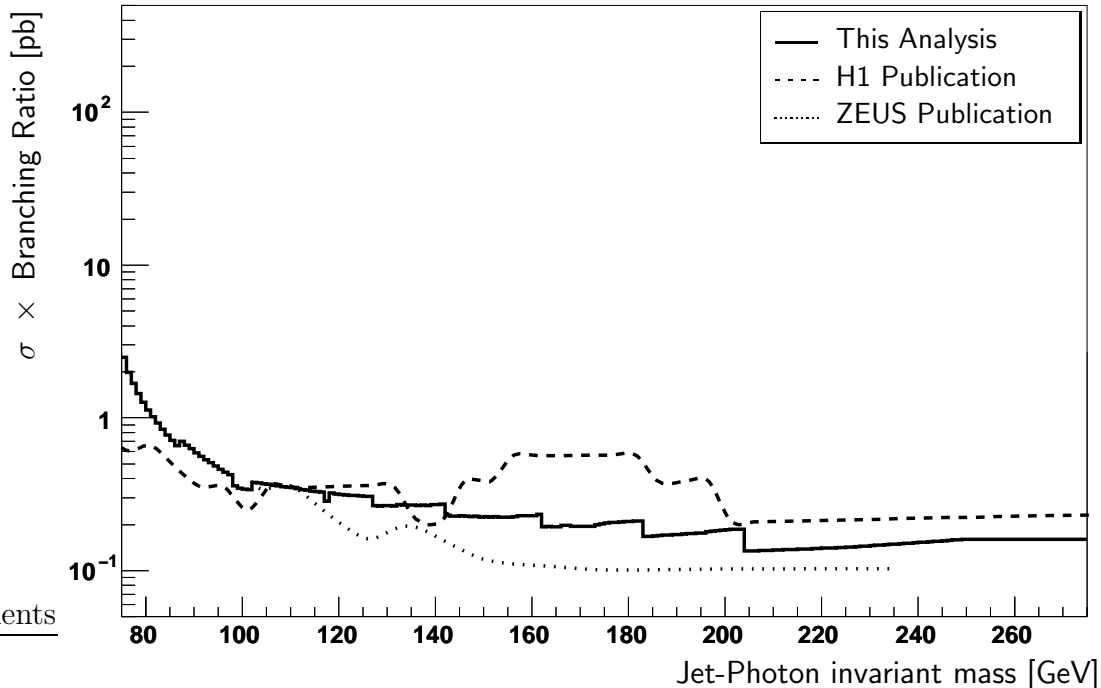


Figure 6.2: *Limit on the cross-section of the excited quark decaying into a photon and a quark. The plot shows the limits calculated in this thesis in comparison to the limit described in the recent H1 publication and the recent ZEUS publication.*

process  $BR$  is given as 1. Figure 6.2 shows the distribution of the limit on the production cross-section of this analysis in comparison to the latest H1 publication and the latest ZEUS publication [48]. The limits are improved for the excited quark masses higher than 120 GeV with respect to the H1 publication. The limits have been determined at a CL of 95%.

### 6.3 Upper limits on coupling parameters

As introduced in Section 2.3 fixed numerical relations between  $f$  and  $f'$  can be assumed. The cross-section then only depends on  $f/\Lambda$  and the mass of the excited quark thus constraints on  $f/\Lambda$  can be derived. We are assuming  $f = f'$  and only electroweak couplings ( $f_s = 0$ ). The limit on the coupling parameter  $f/\Lambda$  can be derived as:

$$\left(\frac{f}{\Lambda}\right)_{\text{lim}} = \sqrt{\frac{(\sigma \times BR)_{\text{lim}}}{(\sigma \times BR)_{\text{Theory}}}} \cdot \left(\frac{f}{\Lambda}\right)_{\text{fixed}} \quad (6.7)$$

where  $(\sigma \times BR)_{\text{lim}}$  is the limit on the cross-section calculated in Section 6.2 and  $\left(\frac{f}{\Lambda}\right)_{\text{fixed}}$  is a fixed coupling with the assumption:  $f = 1$  and  $\Lambda = 1000$  GeV.  $(\sigma \times BR)_{\text{Theory}}$  is calculated from the theoretical prediction of the cross-section and the branching ratio. In this calculation the cross-section and branching ratio of both contributions from the u-quark and d-quark have to be taken into account

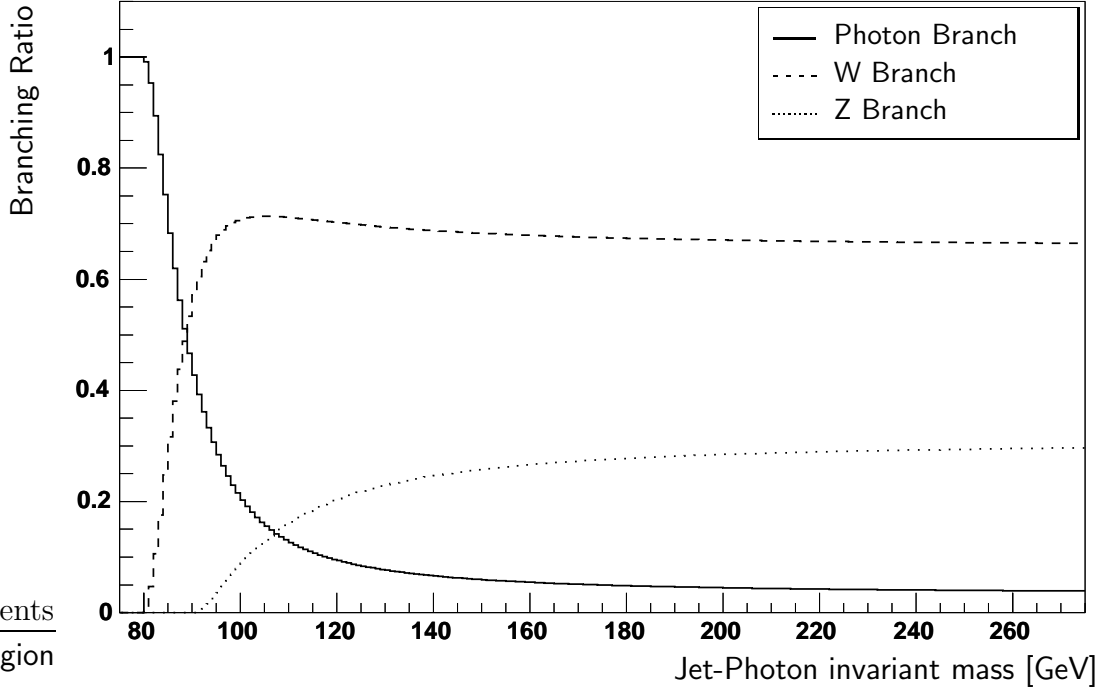


Figure 6.3: Branching ratio for the photon,  $W$  and  $Z$  branch in  $u$ -quark decay.

separately. The combined cross-section and branching ratio is:  $(\sigma \times BR)_{\text{Theory}} = (\sigma_u \times BR_u + \sigma_d \times BR_d)_{\text{Theory}}$ . Figure 6.3 and Figure 6.4 show the branching ratios for the  $u$ -quark and the  $d$ -quark decaying into the photon,  $Z$  and  $W$  branch.

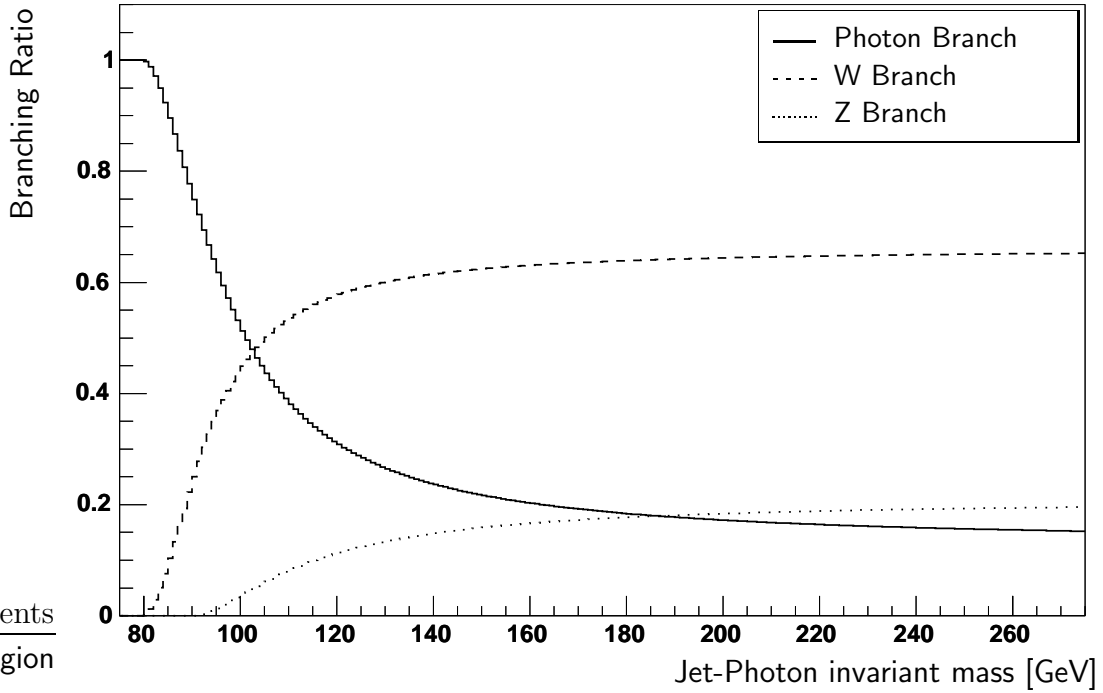


Figure 6.4: Branching ratio for the photon,  $W$  and  $Z$  branch in  $d$ -quark decay.

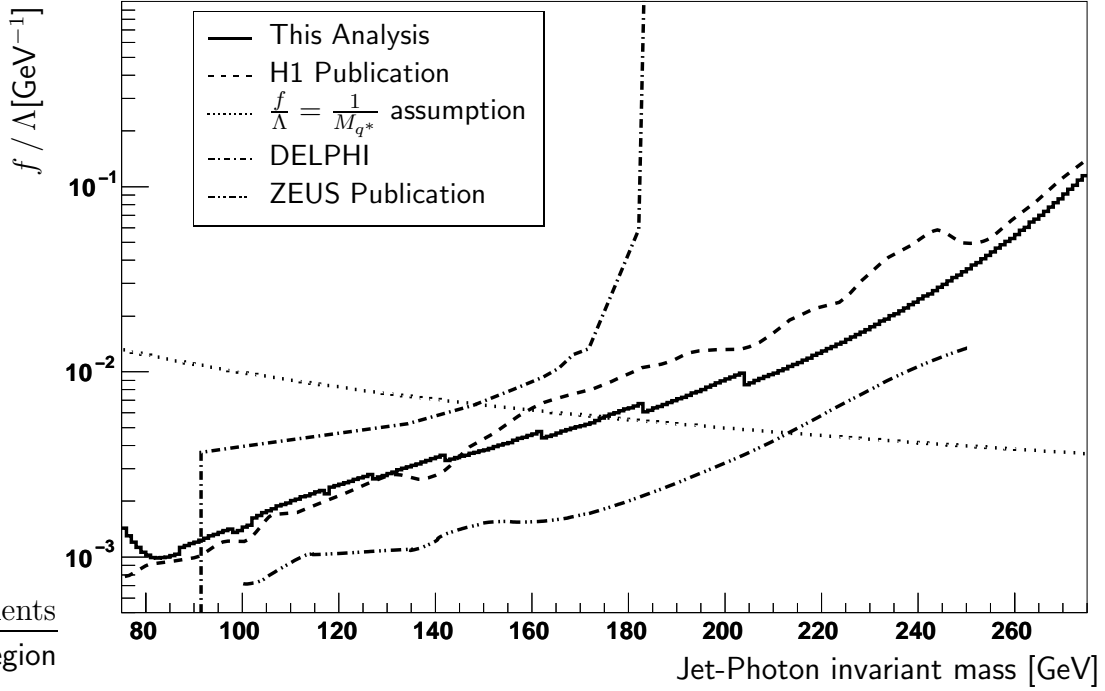


Figure 6.5: *Limit on the coupling parameters for excited quarks. The plot shows the limits calculated in this thesis in comparison to the limit described in the recent H1 publication. For a comparison the limits for the latest ZEUS publication and results from DELPHI are shown.*

Figure 6.5 shows the derived limit on  $f/\Lambda$  in comparison to the latest H1 publication. For further comparison the limits for the latest ZEUS publication [48] and results from DELPHI [49] are shown also. The limits improve the existing H1 limits for masses larger than 145 GeV. Assuming  $\frac{f}{\Lambda} = \frac{1}{M_{q^*}}$  masses below 180 GeV are excluded at 95% CL. Masses below 90 GeV are ruled out by the DELPHI measurements independently of the coupling parameters because pair production of excited quarks is possible below this kinematical limit.

# Chapter 7

## Conclusions and Outlook

In this thesis a search for excited quarks is presented. The dedicated event signature analyzed is the excited quark decaying into a high energetic photon and a high energetic jet, both pointing predominantly into the forward region of the detector. The dominating standard model background comes from neutral current events with a misidentified electron and from photoproduction events with no scattered electron in the detector. Here the dominating background sources come from prompt photon production and from isolated neutral mesons (such as  $\pi^0$  or  $\eta$ ) which are misidentified as photons.

Data collected by the H1 detector in the years 1999 and 2000 with an integrated luminosity of  $63 \text{ pb}^{-1}$  has been used in this analysis. The total integrated luminosity has been nearly doubled in comparison to the latest H1 publication [44]. The analysis has been optimized for a good background reduction of the standard model background processes and for a good signal efficiency for excited quark masses larger than  $100 \text{ GeV}$ . The photon candidate is required to have a minimal transverse momentum of  $40 \text{ GeV}$  with a scattering angle  $\theta$  inbetween  $10^\circ$  and  $80^\circ$ . A veto on not photon like candidates has been applied by not allowing any track to point into the direction of the photon candidate within  $10 \text{ cm}$ . An additional veto is introduced using hits in the proportional chambers. The transverse energy of the jet has to be larger than  $50 \text{ GeV}$ . This selection of the events leads to a very efficient rejection of the background and to signal efficiency of roughly  $40\%$ . In total  $7 \pm 2.7$  data events remain, while  $8.5 \pm 0.4 \text{ (stat.)} \pm 3.0 \text{ (syst.)}$  events are expected from the standard model. No excess of data in the invariant mass distribution is observed. Therefore mass dependend exclusion limits with a confidence level of  $95\%$  on the cross-section and the ratio of coupling constant to the compositeness scale are derived.

The calculated limits improve the existing H1 limits in the high mass regions of larger than  $100 \text{ GeV}$ . The cross section times the branching ratio ( $\sigma \times BR$ ) has been limited to less than  $0.35 \text{ pb}$  for a mass of  $100 \text{ GeV}$  up to less than  $0.18 \text{ pb}$  for excited quark masses around  $275 \text{ GeV}$ . The limit of the ratio of the coupling constant to the compositeness scale ( $\frac{f}{\Lambda}$ ) for a hypothesis of  $f = f'$  has been

improved. With the additional hypothesis of  $(\frac{f}{\Lambda}) = \frac{1}{M_{q^*}}$  and  $f_s = 0$  masses between 50 GeV and 145 GeV can be excluded.

Approaches for further analysis are the extension to run periods before 1999 and of course after 2000 to gain more integrated luminosity and the extension to all decay signatures for general excited fermions.

# Appendix A

## Event Displays of Final Events

The following section show the event displays of all 7 data events that are left after the final cuts.

Photon:  $\theta = 15.8^\circ$       Jet:  $\theta = 23.5^\circ$       Inv Mass:  $M_{q^*} = 80.5 \text{ GeV}$   
 $\phi = 172.2^\circ$        $\phi = -5.5^\circ$   
 $p_T = 41.7 \text{ GeV}$        $E = 93.4 \text{ GeV}$

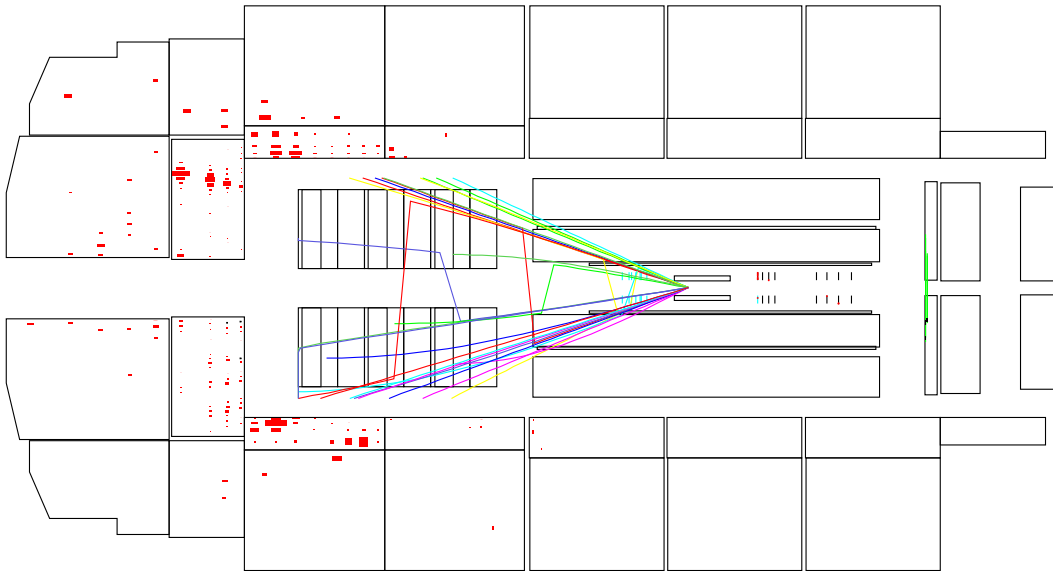


Figure A.1: *Event display of final data event number: 41978, run: 255579*

Photon $\theta$	=	24.3°	Jet $\theta$	=	64.8°	Inv Mass $M_{q^*}$	=	87.8 GeV
$\phi$	=	75.0°	$\phi$	=	-103.6°			
$p_T$	=	53.3 GeV	$E$	=	64.8 GeV			

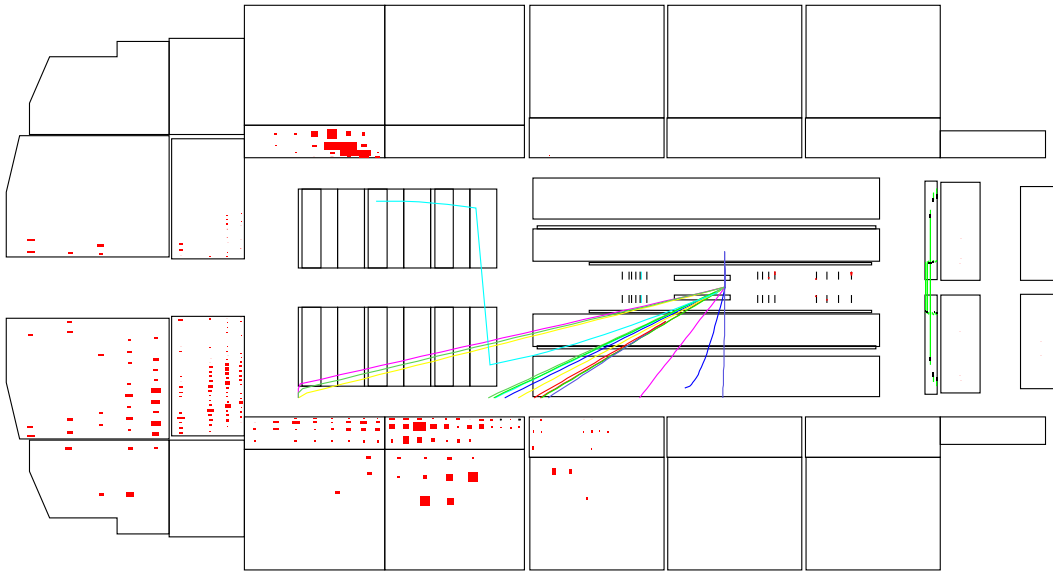


Figure A.2: Event display of final data event number: 68646, run: 256879

Photon $\theta$	=	45.4°	Jet $\theta$	=	12.7°	Inv Mass $M_{q^*}$	=	156.2 GeV
$\phi$	=	147.6°	$\phi$	=	-30.4°			
$p_T$	=	70.3 GeV	$E$	=	262.5 GeV			

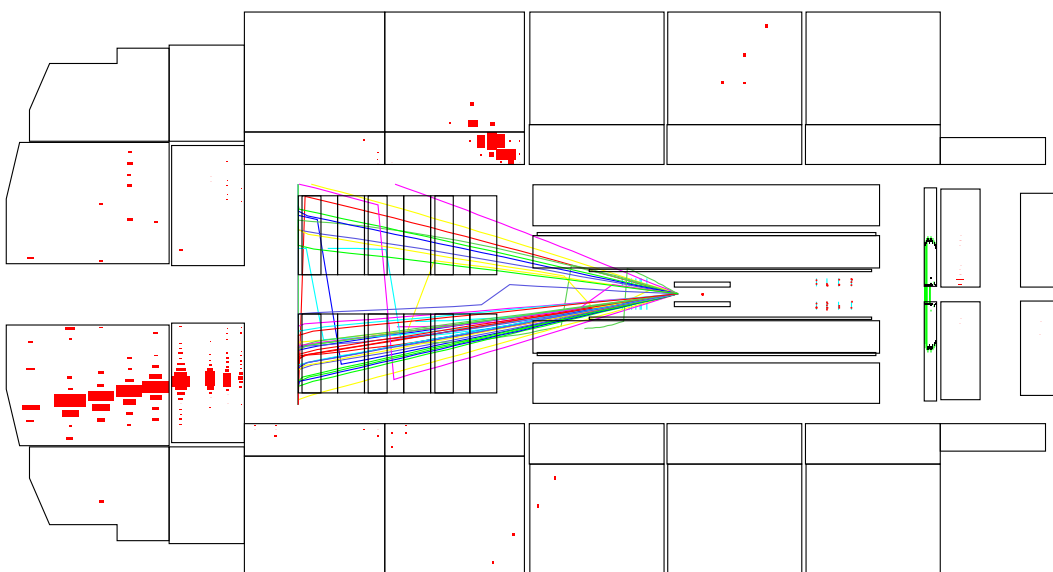


Figure A.3: Event display of final data event number: 54795, run: 264978

Photon  $\theta = 70.2^\circ$     Jet  $\theta = 13.5^\circ$     Inv Mass  $M_{q^*} = 117.0 \text{ GeV}$   
 $\phi = 8.0^\circ$      $\phi = -166.2^\circ$   
 $p_T = 41.9 \text{ GeV}$      $E = 173.1 \text{ GeV}$

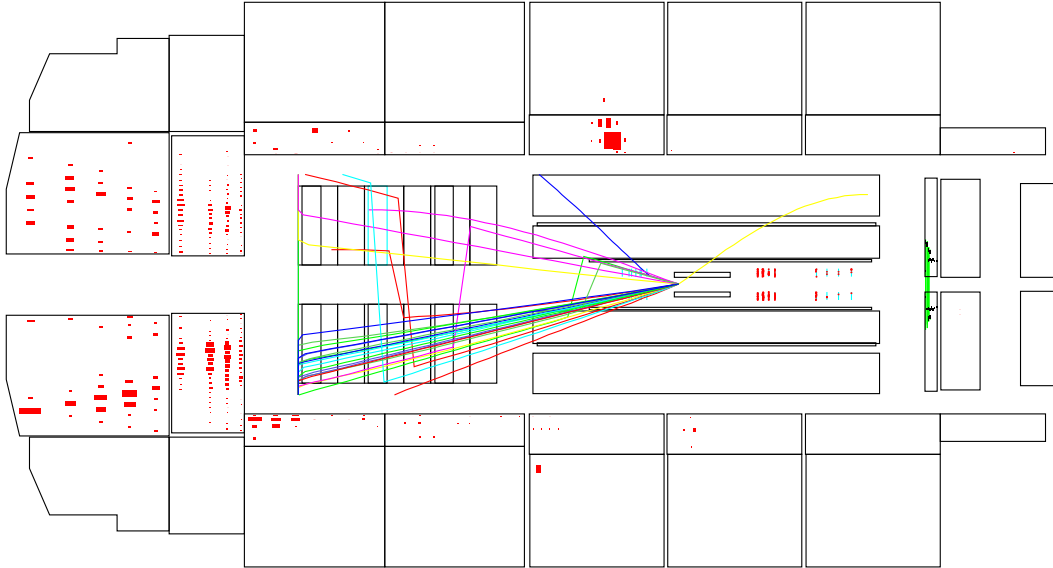


Figure A.4: Event display of final data event number: 19635, run: 268175

Photon  $\theta = 70.2^\circ$     Jet  $\theta = 41.9^\circ$     Inv Mass  $M_{q^*} = 99.9 \text{ GeV}$   
 $\phi = 84.9^\circ$      $\phi = -94.9^\circ$   
 $p_T = 49.4 \text{ GeV}$      $E = 69.1 \text{ GeV}$

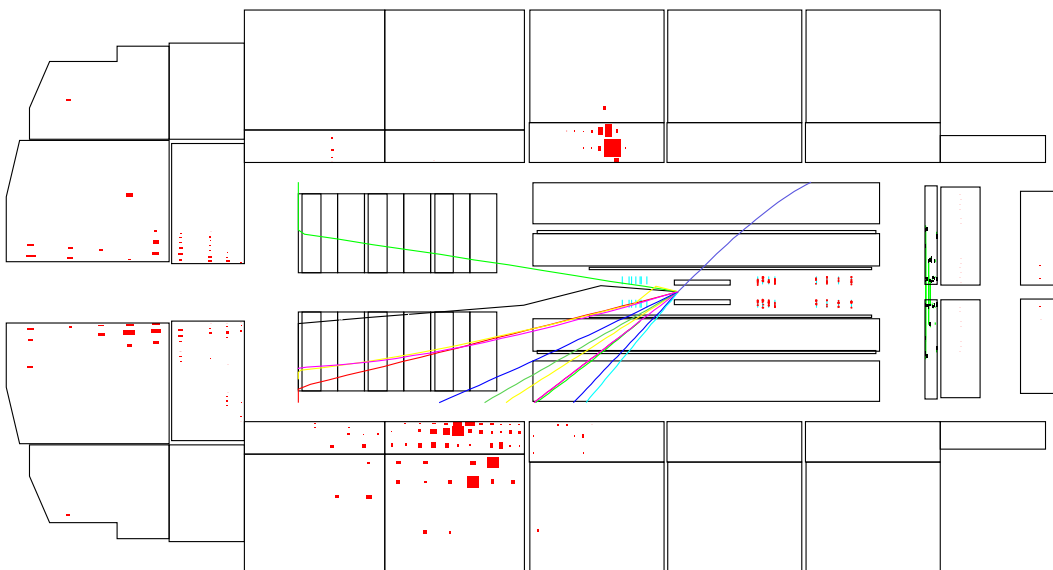


Figure A.5: Event display of final data event number: 17345, run: 276828

Photon  $\theta = 32.3^\circ$       Jet  $\theta = 22.2^\circ$       Inv Mass  $M_{q^*} = 136.3 \text{ GeV}$   
 $\phi = 63.4^\circ$                $\phi = -118.0^\circ$   
 $p_T = 68.9 \text{ GeV}$            $E = 171.9 \text{ GeV}$

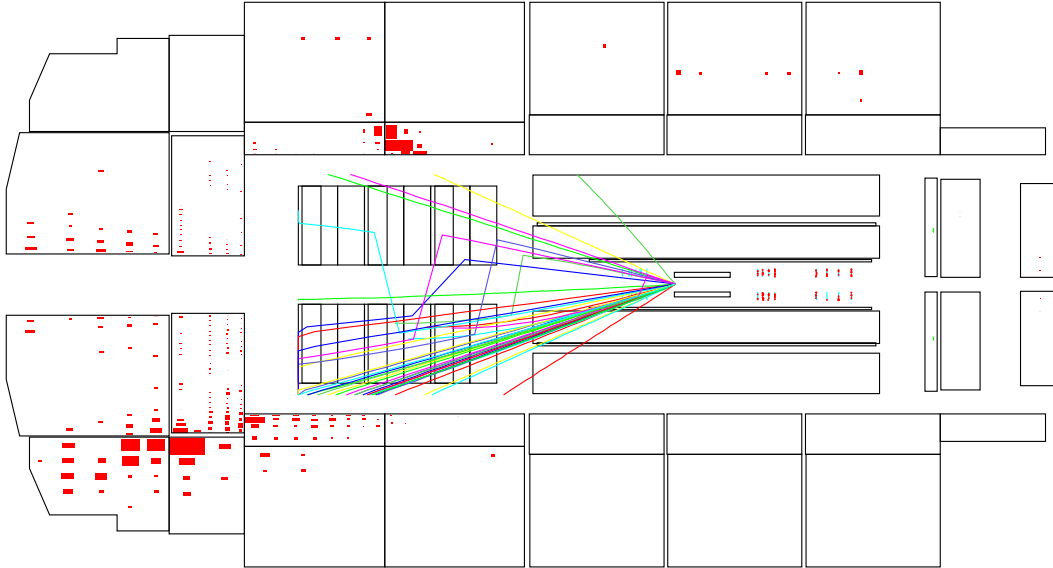


Figure A.6: Event display of final data event number: 18086, run: 277142

Photon  $\theta = 29.0^\circ$       Jet  $\theta = 23.7^\circ$       Inv Mass  $M_{q^*} = 65.4 \text{ GeV}$   
 $\phi = 129.6^\circ$                $\phi = -57.8^\circ$   
 $p_T = 47.5 \text{ GeV}$            $E = 55.7 \text{ GeV}$

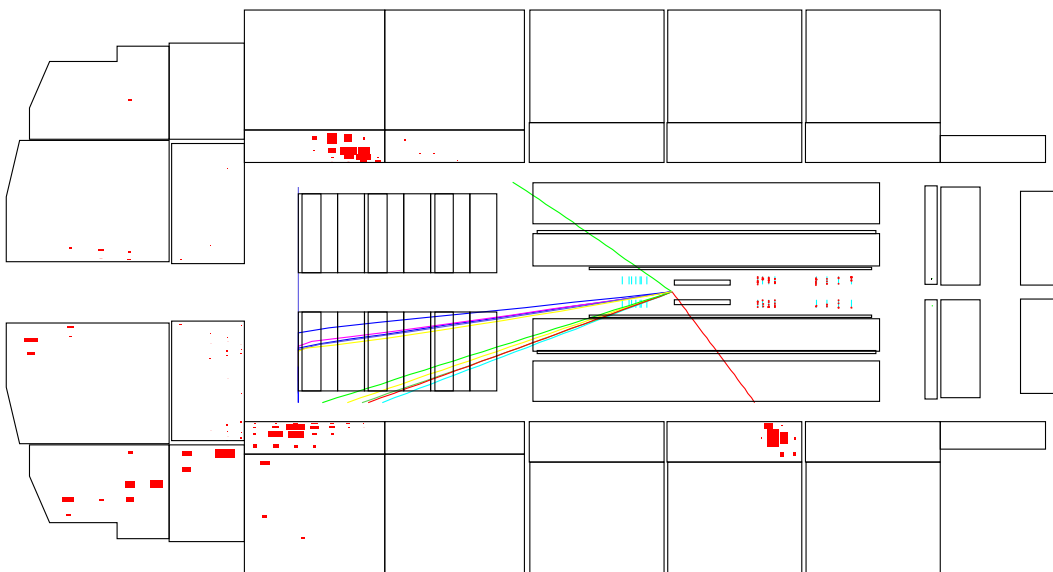


Figure A.7: Event display of final data event number: 147679, run: 278419

# Appendix B

## CIP2000 Trigger Readout System

The investigations of rare processes at the limits of the kinematically accessible range at HERA requires high luminosity. In the year 2000 an upgrade of HERA and the corresponding experiments was accomplished with the goal to increase the luminosity of HERA by a factor of 5 to about  $7.4 \times 10^{31} \text{ cm}^{-2}\text{s}^{-1}$ , which would lead to an annual integrated luminosity of  $150 \text{ pb}^{-1}$ . For further information on the physics goals of the upgrade see [50].

The higher luminosity is mainly achieved by a stronger focusing of both beams in the experimental areas. This required the installation of three new superconducting magnets inside the H1 detector and significant changes to the inner part of the H1 detector were necessary. The assumption was that also the beam related background would increase with higher luminosity, although it is very difficult to predict quantitatively how much. For this reason the CIP2000 upgrade project replaced the CIP and CIZ chambers by a new 5 layer MWPC. A new fast trigger system based on the cathode pad signals of this new chamber was installed to skip uniquely upstream proton background and provide a strongly improved rejection capability for those events. Electron beam induced photon background is suppressed due to the new five layer chambers instead of only two in the old system.

The CIP2000 trigger builds coincidences of pads in the five layered CIP2000 chamber and defines tracks of particles going through the detector. Tracks originating from the beam axis of the H1 detector are counted and summed up in different regions (size:  $\sim 20 \text{ cm}$ ) of the z-axis separately. The resulting numbers form a histogram called z-vertex histogram. It reaches from the forward direction nearly through the whole main detector up to the SPACAL. From this information proton-upstream background events can be easily identified. These events can be rejected or specially examined.

### B.1 CIP2000 Trigger System Overview

The CIP2000 trigger system consists of three main parts. The first part delivers the actual signals from the interactions. 5 cylindrical layers of proportional

chambers deliver the signals for the CIP2000 trigger system via an optical readout. Each layer is divided in 16 sectors in  $\phi$  and about 120 equidistant pads in the  $z$  direction. A projective geometry was chosen to make the tracking algorithm easier [51, 52]. The chamber has an acceptance in  $\theta$  of  $10^\circ - 170^\circ$ . The second part is the CIP2000 trigger and the STC (Subsystem Trigger Control) system forming the subsystem trigger elements and implementing the communication of fast signals between the H1 central trigger and the CIP2000 subsystem trigger. The third part is the readout system of the CIP2000 trigger to extract all chamber and trigger data in the case of a positive trigger decision. Figure B.1 shows a schematic overview of the whole CIP2000 trigger system.

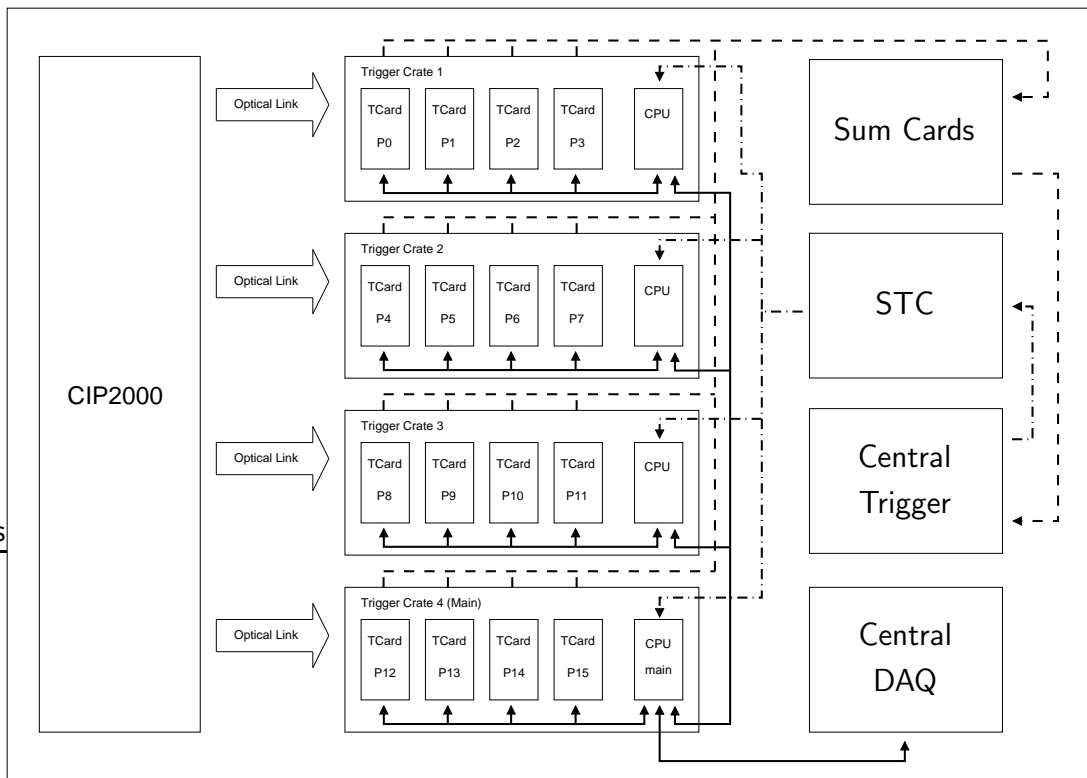


Figure B.1: Schematic overview of the CIP2000 trigger system. Fast signals going towards the central trigger are drawn as dashed lines. Dash-dotted lines represent fast signals coming from the central trigger going to the subsystem. Solid lines mark the readout chains.

The chamber signals of all 5 layers of each of the 16 sectors in  $\phi$  are treated in one trigger card. Four of the trigger cards - corresponding to one quadrant in  $\phi$  - are equipped in one trigger crate. The trigger cards are equipped with FPGAs (Field Programmable Gate Arrays) to make the trigger most flexible and to deal with the big amount of input channels. The FPGAs contain the actual trigger algorithm delivering the  $z$ -vertex histogram separated in  $\phi$ . They also contain the 32 bunch crossings ( $1 \text{ BC} \approx 96 \text{ ns}$ ) deep pipelines storing all the chamber pad data until a positive decision of the H1 central trigger is made. The pipeline is built as a ring

buffer overwriting the data after 32 BCs with new data. The z-vertex histograms are summed up in 3 steps to an overall z-vertex histogram in so called sum cards equipped in a separate crate. After the overall z-vertex histogram is built trigger elements are formed from this information and are send to the central trigger. The central trigger is connected to the CIP2000 subsystem via the so called STC cards in a special STC crate. These cards deliver all necessary fast and slow signals to the subsystem including the very important HERA clock signal and of course the trigger decision from the central trigger. Basically all computing steps in all subsystems are synchronized to the HERA clock of 10.4 MHz. A detailed description of the trigger system, the trigger algorithm and the trigger hardware can be found in [53, 52]. A detailed description of the STC system and preparative tests of the readout system of the CIP2000 trigger system can be found in [51].

## B.2 CIP2000 Trigger System Readout Structure

The readout system of the CIP2000 trigger mainly consists of components already used at the H1 experiment. A part of the readout system structure is shown in Figure B.2. Four trigger CPUs are managing the data readout from the pipelines on the trigger cards to the central data acquisition. One trigger CPU called the main trigger CPU handels the communication to the STC system and the TAXI CPU. The TAXI CPU is the link to the central DAQ of the H1 experiment. The CPUs of the different so called DAQ branches are connected via gigabit ethernet. Before this part of the DAQ was upgraded the data transport was achieved with an optical readout ring connecting specific VMEtaxi cards instead of the CPUs. Different bus standards are used in the whole trigger readout system. The common bus systems in the H1 experiment are the VME bus and the VSB bus. VIC links or VME repeaters connect the VME busses of different crates. A pVIC link connects the local PCI busses of different trigger CPUs. Section B.3 explains the different components and links of the readout system. The pipelines containing the chamber data are implemented in FPGAs mounted on the trigger cards. The same FPGAs run the trigger algorithm. A certain event window consisting of 3 to 5 events is read from the pipeline. The event window is centered around the designated actual triggered event. It is necessary to read out the whole event window to observe the timing behaviour of the trigger and to make sure that the actual triggered event is read out. The information of the full event window could be used to detect a pile up of events in the LAr calorimeter. The events are stored in a readout register in the FPGAs independent of the pipelines. A VME controller on the trigger card maps the readout register on the VME bus. The trigger CPUs can read out the events via the VME bus in a VME block mode. The trigger CPUs collect the event data and transfer the data to the main trigger CPU. The main trigger CPU merges the data of the different trigger CPUs and sends it to the TAXI CPU. The readout of the data from the pipelines via the VME bus to the trigger CPUs is called horizontal readout. The readout of

the data from the CPUs to the main trigger CPU is called vertical readout. The trigger CPUs communicate with the main trigger CPU via a protocol based on control registers implemented in the actual data buffer space. All communication is done via the pVIC link. The block mover of the pVIC system is used to transfer the event data most efficient. The arbitration of the pVIC bus during the block mover access has been implemented using the control registers in a semaphoric way. The initial initialisation of the pVIC system is done via ethernet to set the addresses of the memory spaces. The main trigger CPU communicates with the STC system via a VME repeater link to the STC crate. Interrupts can be passed through to the main trigger CPU and registers and scalers in the STC cards are read and modified.

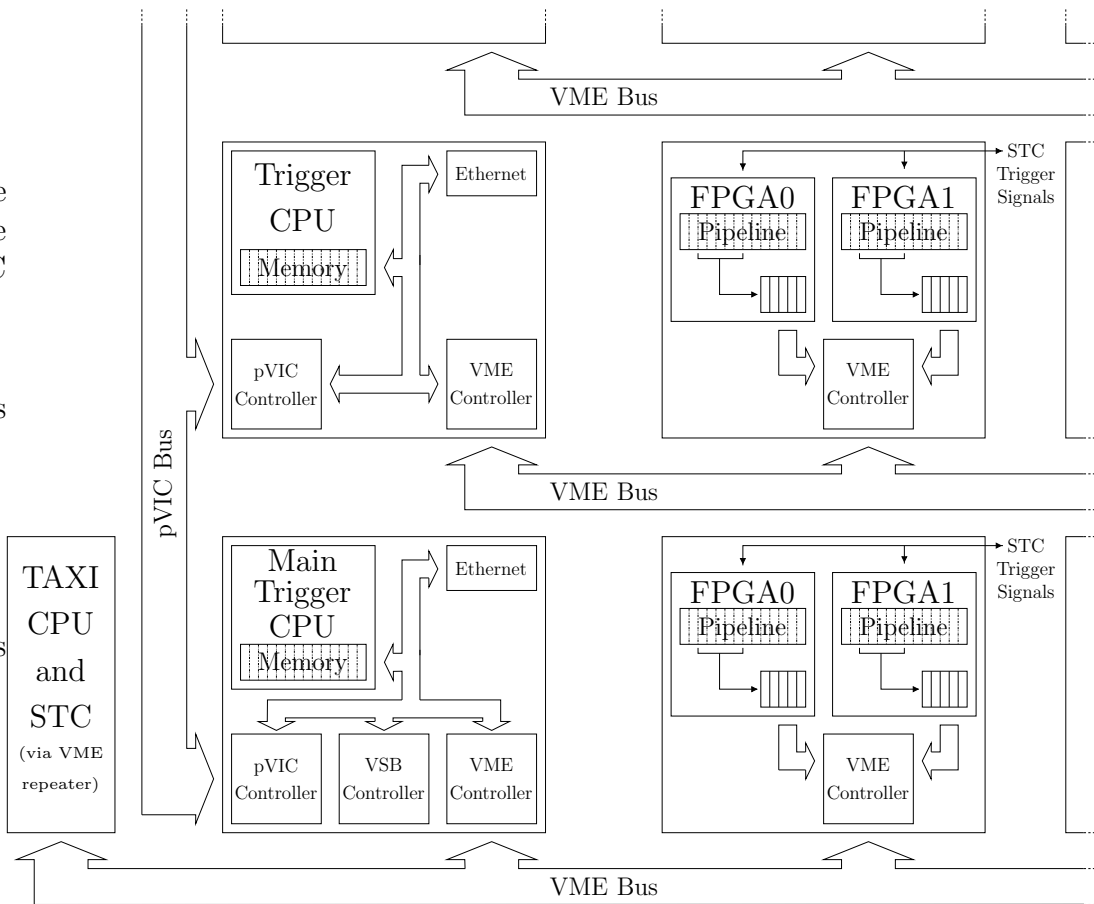


Figure B.2: CIP2000 trigger readout structure. The pipelines containing the chamber data are implemented in FPGAs mounted on the trigger cards. A certain event window of 3 to 5 events is read from the pipeline. These events are stored in a readout register in the FPGAs independent from the pipelines. The trigger CPUs can read out the events via the VME bus in a VME block mode. The trigger CPUs collect the event data and transfer the data to the main trigger CPU. The main trigger CPU merges the data of the different trigger CPUs and sends it to the TAXI CPU.

## B.3 CIP2000 Trigger System Readout hardware

In the following the different bus systems and components used in the CIP2000 trigger system readout are described. First the VME bus is introduced as a generic bus system widely used in H1 as a standard. The second section gives an overview of the facts important to access the trigger cards via the VME bus. The next sections describes the CPUs used in the readout system. The last two section give an overview of the bus to vertically interconnect the CPUs (pVIC) and a bus system used to connect VME busses of different crates called VIC.

### B.3.1 Connection of CPU and trigger card: VME

The VME bus (**V**ersatile **M**odule **E**urope) is a flexible open-ended bus system widely used as a standard in the H1 experiment which makes use of the Eurocard standard. It was introduced by Motorola, Phillips, Thompson, and Mostek in 1981. VME bus was intended to be a flexible environment supporting a variety of computing intensive tasks. It is defined by the IEEE 1014-1987 standard. A documentation can be found in [54] released by the VITA (**V**MEbus **I**nternational **T**rade **A**ssociation) association.

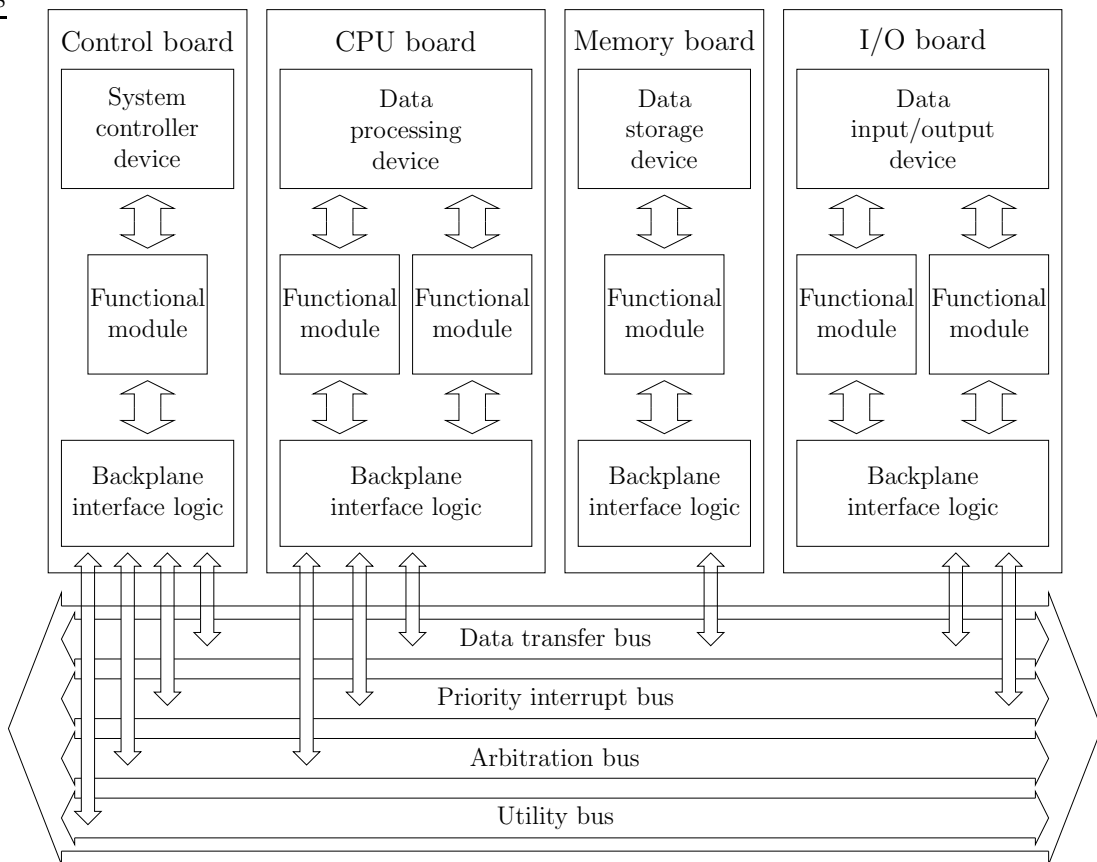


Figure B.3: Structure of VME functional modules and buses

The bus usage offers a completely memory mapped scheme. Every device can be viewed as an address, or block of addresses. Addresses and data are not multiplexed. The bus allows multiple masters and contains a powerful interrupt scheme. A resource manager is required to handle the interrupts. The VME bus uses a TTL based backplane which, although the system is asynchronous, can obtain a data transfer speed of approximately 10 Mbytes per second.

A typical transfer consists of an arbitration cycle to gain bus control, an address cycle to select the register to access and the actual data cycle. Read, write, modify and block transfers are supported. The VME bus system consists of 4 sub buses: the data transfer bus, the arbitration bus, the priority interrupt bus and the utility bus. The data transfer is asynchronous supporting modules with a broad variety of response times. The system is modular and follows the Eurocard standard. Standard VME crates contain 21 slots. The first slot must be used as a crate manager. The usual card sizes are  $160 \times 216$  mm and  $160 \times 100$  mm. Cards of both sizes can be mixed in the same crate. The smaller cards are capable of 8 or 16 bit data transfers. The larger cards can perform 8, 16, 32 or even 64 bit data transfers and can also support a larger address range of 4 Gbytes memory for A32 access instead of 16 Mbytes of memory for A24 access. All VME boards have a P1 connector. Larger cards may have an optional P2 connector. Parts of the P2 connector are used in newer VME standards. Figure B.3 shows the structure of the functional modules and buses defined by the VME standard.

**Arbitration bus** A module controlling the bus will drive the bus busy line (BBSY) low to show that it is in use. When this line is not low the arbiter module will scan the bus request lines (BR0-BR3) looking for a pending action. Requests on the BR3 line have the highest priority. Requests of equal priority are handled by a daisy chain using the bus grant in lines (BG0IN-BG3IN) and the bus grant out lines (BG0OUT-BG3OUT). The arbiter module mounted in slot 1 generates the first grant signal passed on to modules of increasing slot number.

**Data transfer bus** The data transfer bus is used for transferring data between different modules. The data bus lines (D00-D31) hold the actual data during a transfer. The address of the register being accessed is presented on the address bus lines (A01-A31). The address modifier lines (AM00-AM05) indicate the length of the address, the kind of data cycle and the master identifier. The address strobe signal (AS) is used to signal the presence of a valid address. The data strobe signals (DS0, DS1) are used by the master module controlling the data transfer to signal the presence and acceptance of valid data on the bus. Together with the (LWORD) signal the data strobe signals present information on the size of the word to be transferred. The WRITE signal line is used to distinguish between read and write operations. The data transfer acknowledge (DTACK) signal is used by the slave module to signal the completion of a transfer. Errors in this transfer are signaled using the bus error line (BERR).

**Priority interrupt bus** Processors in the system are dedicated to handling interrupts by monitoring the interrupt request lines (IRQ1-IRQ7). The interrupt request line IRQ7 has the highest priority. In response to an interrupt, an address cycle is generated indicating that the request has been acknowledged. The interrupt acknowledge (IACK) signal is changed in the arbiter to a signal which is daisy chained down the bus using the interrupt acknowledge in pin (IACKIN) and interrupt acknowledge out pin (IACKOUT). A data cycle follows where the module requesting the interrupt posts its status and ID.

**Utility bus** The power is supplied to modules via pins at +5 V, -12 V and +12 V. An optional battery backup of the +5 V supply indicated by the (+5STDBY) signal can also be present. The utility bus supports an independent 16 MHz system clock (SYSCLK). The system failure signal line (SYSFAIL) and the AC failure signal line (ACFAIL) indicate global system problems. The system reset signal line (SYSRESET) is used for the initialization of the system. An additional data transfer synchronized with the serial clock line (SERCLK) can take place along the serial data line (SERDAT).

The J1 backplane of the trigger crate is a standard VME D64 backplane. The J2 backplane of the trigger crates is a special backplane with the first 3 slots corresponding to the VME D64 standard and special connectors for the rest of the backplane supporting the VME D64 standard without the standard pin assignment to access the trigger cards and the control cards. The optical receiver cards can be mounted on the back side of the J2 backplane. Additional power supplies of +2.5 V and 3.3 V for the trigger cards are used. The trigger CPUs used in the trigger readout system provide all slot 1 functions of the VME standard like arbitration, interrupt acknowledging and a bus time out function.

### B.3.2 Trigger card

A detailed description of the trigger card can be found in [52]. The main devices on the trigger cards are the two FPGAs APEX 20k400GCC/3 [55] from the company Altera. The FPGAs have an internal memory space to implement a pipeline for the chamber data and sufficient room to run the trigger algorithm. A VME [54] controller build in a Lattice ispL-2048 PLD [56, 57] manages the VME access to the trigger card. The VME controller is build for a A24/D32 VME access to the devices on the trigger card. It supports the VME single cycle mode and the VME block mode. A built in daisy chain makes it possible to span the block of a VME block transfer over several trigger cards. The mapping of the different devices on the trigger card is shown in Figure B.4.

The most significant byte of the 24 bit wide address of the VME bus resources specifies the trigger card. Two hexadecimal rotary switches on the trigger card define the VME base address of the trigger card. The Lattice control bits specify the access to registers in the VME controller and control special features like

programming the EEPROMs or the FPGAs from the VME bus. The APEX control bits specify the different resources in the FPGAs like the pipelines and registers. The APEX bits are used to map an address space in the different resources of the FPGAs. Other address lines are not connected to devices on the trigger card. All 32 data lines are connected to the VME controller and both FPGAs.

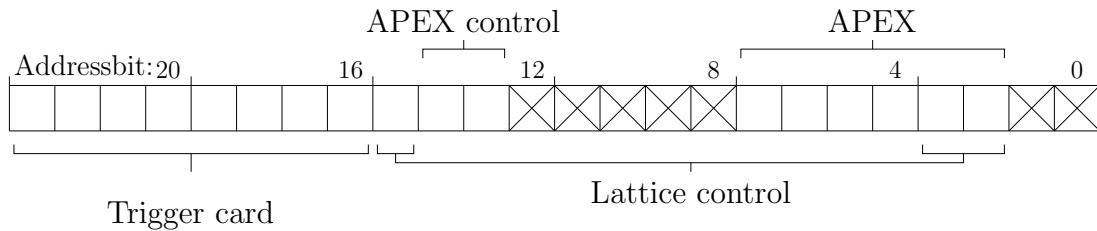


Figure B.4: Mapping of the VME resources on the trigger cards.

### B.3.3 CPU board

As trigger CPUs and the main trigger CPU RIO2 8062 PC boards manufactured by the company CES are used. They are described in detail in [58]. Figure B.5 shows an overview of the structure of the PC board. The main part of the RIO2 8062 PC board is the PowerPC 603 CPU with the system memory and the L2 cache. These components are connected via a local bus and build the main computing unit of the board. A PCI bridge links the main computing unit to the PCI bus of the PC board. All other components of the board are connected to the PCI bus. An ethernet controller supporting 10/100 baseT ethernet can link the PC board resources to a local area network.

A VME bridge supporting D32/D64 access to the VME board maps the local PCI bus on the VME bus and vice versa. A BMA (**B**lock **M**over **A**ccelerator) controller manages the transfer of big amounts of data between the VME bus and the PCI bus. The PC board has different sub I/O resources accessible via the PCI which are timers, an interrupt controller, two serial lines and a FEPR0M holding data without a connection to a power supply. Different PMCs (**P**CI **M**ezzanine **C**ard) can be mounted on the PC board for different tasks. In the trigger system PMCs for SCSI adapters, pVIC connections and VSB connections are used. The following resources of the PC board are mainly used in the trigger readout system.

**Computing unit** The PC boards in the trigger readout system use an IBM PowerPC 603e microprocessor, Mach5, Arthur 740. 32 Mbyte system memory and 1 Mbyte L2 cache are installed. The different parts of the computing unit are connected via a CPU bus.

**PCI bridge** The IBM 27-82660 PCI bridge is the connection of the computing unit to the PCI bus of the PC board. It manages the mapping of the system

memory and registers in the CPU to the PCI bus. Interrupts coming from a device on the PCI bus can be mapped on the CPU. A PCI central arbiter handles the arbitration process of the different PCI devices on the PC board.

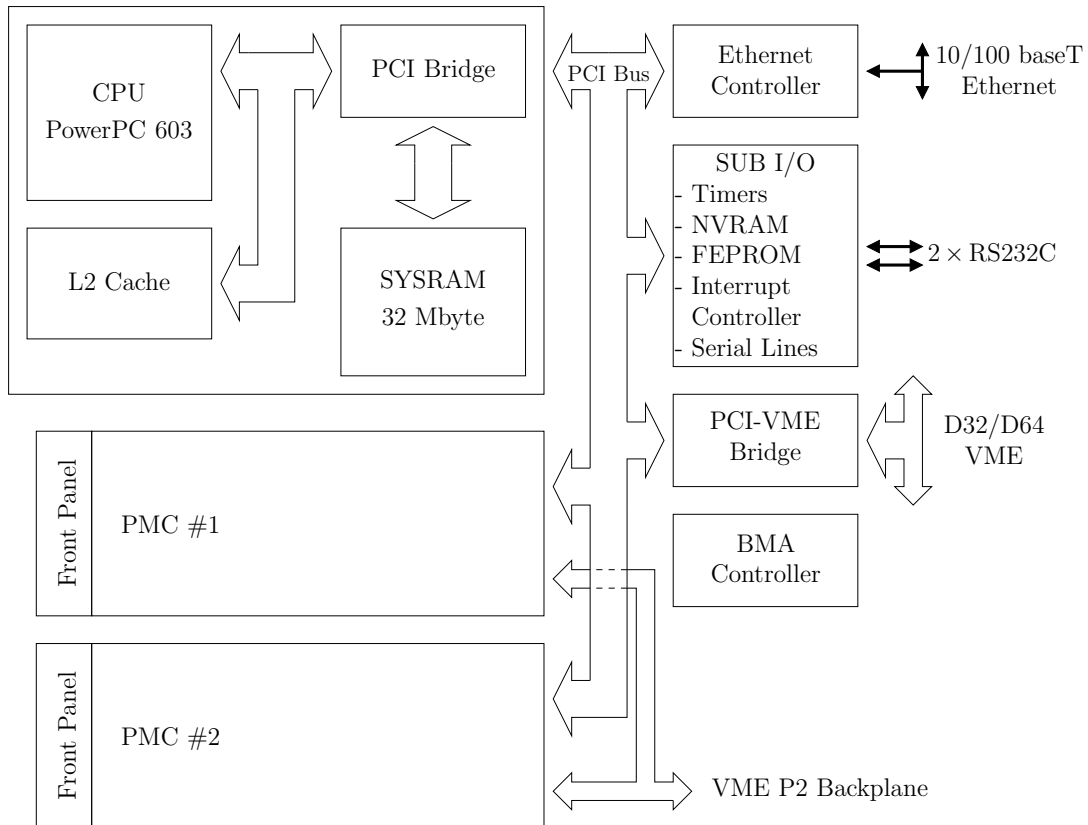


Figure B.5: *Structure of the RIO2 8062 PC board*

**VME bridge** The VME interface of the PC board incorporates VME master and slave logic. The VME slave mapping is done through a programmable 16 to 128 Mbytes window to map the internal system memory and through a 64 Kbytes window to map resources such as remote reset, message passing FIFO and remote configuration parameters. The memory windows are divided in 2048 pages of 64 Kbytes, each of them owning a page descriptor for the complete PCI address and specific control bits. The VME master access is mapped on two PCI windows. These windows are divided in pages of 64 Kbytes, each of them owning a page descriptor for the complete VME address, address modifier and specific control bits. A complete VME arbitration requester is implemented as well as a full VME slot 1 functionality. VME IACK cycles can also be generated to implement a VME interrupt handler through specific page descriptor initializations.

**BMA controller** An autonomous VME-PCI block mover (BMA) is integrated to implement efficient data transportation between the local system memory

and the VME bus. This block mover allows the implementation of high speed VME transactions in the D32 and D64 mode.

**FEPRM** An 8 Mbyte flash EPROM is available on the PC board. The PC board can be booted from the FEPRM.

**Ethernet controller** The ethernet controller PC-Net 79C97x is interfaced directly on the local PCI bus and also to a serial EEPROM storing initial network parameters. All PCI target devices can be addressed by the ethernet controller.

**Serial lines** Two full modem RS232 serial interfaces are provided on the PC board. They are completely independent.

**Interrupt controller** The interrupt structure of the PC board is based on the SIC 6351 ASIC. All on board interrupts are routed to the ASIC and dispatched to the PowerPC CPU through the PCI bridge with programmable registers. Interrupt sources can be the VME bus, the ethernet controller, the BMA handler, the serial lines, PMCs or timers.

### B.3.4 Connection of CPUs: pVIC

The pVIC bus is a high bandwidth PCI to PCI transparent connection. Remote PCI resources are seen as if they were local. A detailed description of the pVIC system and its components can be found in [59]. This bus system was developed by the company CES. It allows to connect clusters of 15 nodes spanning up to 200 meters while preserving the full PCI throughput (132 Mbyte/s at 32 bit, 33 MHz). An integrated DMA controller allows to perform complex data transactions with a minimal CPU load. Broadcast, and multicast cycles, interrupt dispatching, mailboxes, a mirrored memory and global semaphores provide the hardware support for efficient interprocessor communication. Different transmission technologies like GTL+, differential PECL lines and an optical link are available for the pVIC system. The pVIC module used in the CIP2000 trigger system readout is mounted on a PMC housed in the trigger CPU board.

**Master interface** The local bus to pVIC bridge is controlled through an outgoing scatter-gather making the complete remapping of the local addressing schema to the pVIC addressing possible. The pVIC uses a PCI memory space window of 32 to 256 Mbyte. This window is tailored in  $4092 \times 64$  kbyte pages. Each individual page is associated with a descriptor supplying the pVIC page parameters.

**Slave interface** The pVIC slave interface permits access to the pVIC local resources like registers, SSRAM, mirrored memory and the local PCI bus. It receives and decodes the pVIC transaction. The decoding is handled through node id informations. Each pVIC slave has its own unique node id. pVIC broadcasts to all nodes are possible.

**Mirrored memory** The pVIC mirrored memory allows the building of a shared memory system with a global write and a local read. The mirrored memory is implemented with a true dual port SRAM device.

**DMA controller** The pVIC interface incorporates a DMA controller. The local DMA controller supports a local read and pVIC write. The DMA initialization is controlled by a chaining-block in the local SSRAM. The DMA chaining-block initialization can be done locally or remotely from the pVIC.

**Interrupt dispatching** The pVIC provides a mechanism to export transparently local interrupts or events to external pVIC nodes. On an event detection the local controller issues a mirrored memory write transaction.

### B.3.5 Connection between different VME busses: VIC

The VIC system connects different crates with local bus systems like the VME bus. It uses the the VMV bus structure to transfer the data between the different crates. A detailed description of the VIC modules build by the company CES can be found in [60]. The VMV bus is a multiplexed bus for full 32 bit address and data transfer. Figure B.6 shows the structure of the in the CIP2000 trigger readout system used VIC module. Two of these modules are connected by two flat cables transmitting signals in differential standard. The module can be accessed by the VME bus and by a VSB bus.

**VMV bus** The VMV bus is a multiplexed bus for full 32 bit address and data transfer. The electric signals transmitted across the two flat cables are differential. Each signal of the differential bus is terminated at its two physical ends by an active terminator. The VMV bus is asynchronous and uses a signal called vertical timing to provide a correct handshake mechanism between the master and the slave. Three different types of transfer cycles are supported. A direct access on the local VME of the VMV slave module, a direct access on the internal control resources of the VMV slave and interrupt cycles to pass the interrupt information on to the VME bus. The interrupts are transfered multiplexed on the bus interrupt lines.

**VMV master** The VMV master module drives the VMV bus. Incoming VME or VSB cycles destined for the VMV bus are controlled by this logic. Arbitration phases and handshaking cycles are transparent to the VME and VSB bus. The internal TTL signals are converted into differential signals to drive the VMV flat cables.

**VMV slave** The VMV slave module decodes the VMV bus cycles and converts them into one of four types of cycles. A cycle to access the VMV internal registers, a cycle to access the VME resources, a cycle to generate VME

interrupt acknowledge cycles and a cycle to access the internal buffer memory. The VMV slave internal register module contains informations about the VMV slave module and the VME master interface.

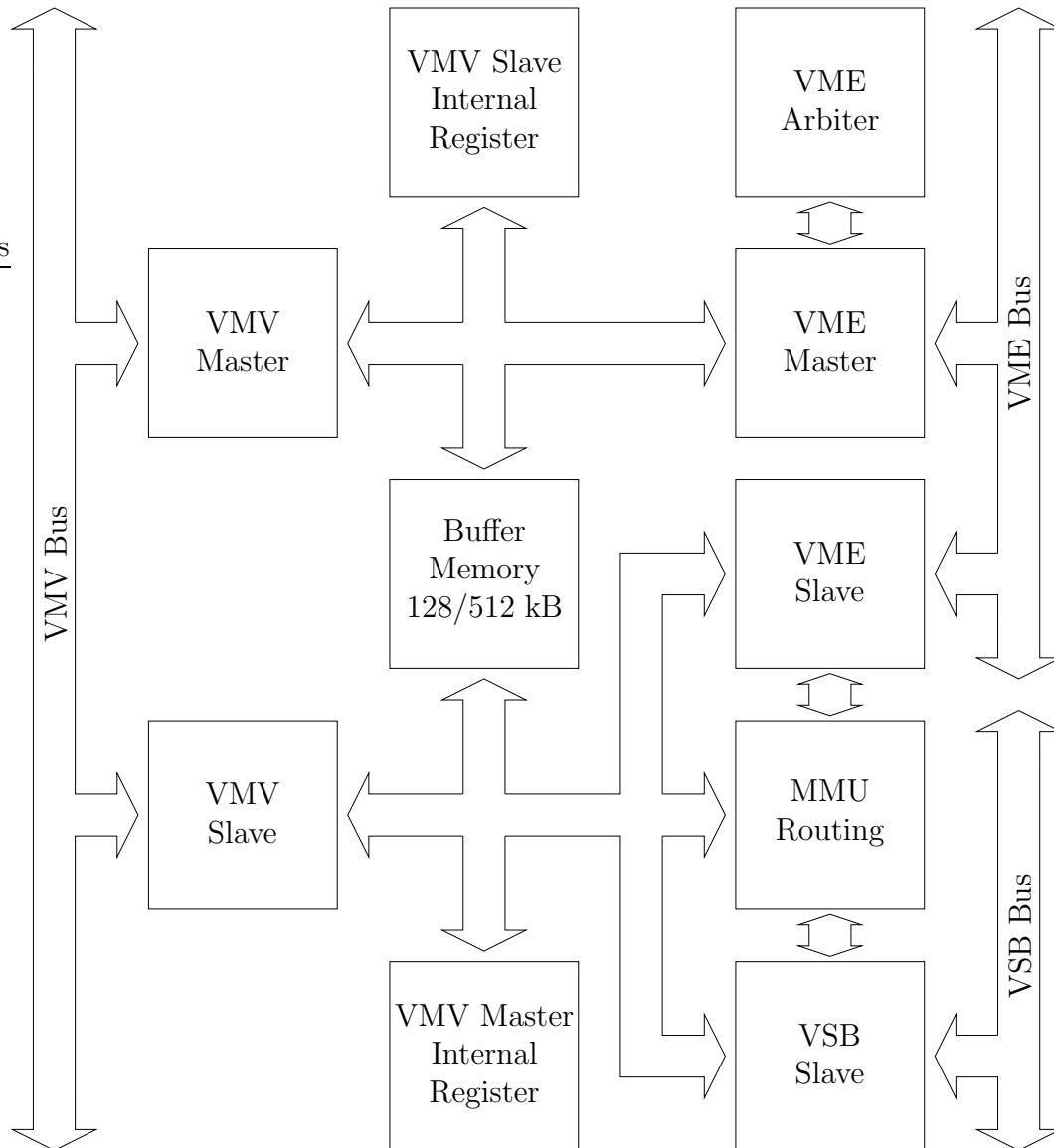


Figure B.6: *VIC 8250 module structure*

**VME master** The VME master module converts the decoded VMV cycles into standard VME cycles. The conversion is done in real time at every cycle. A build in VME arbitration module can handle the VME arbitration.

**VME slave** The VME slave module connects the VIC module to the VME master unit of the VME bus. The VME slave resources are mapped to the VME

bus in a 1 Mbyte window in the VME standard address space. The mapping is defined by a hexadecimal rotary switch. The VMV master internal register, the VMV slave internal registers, the internal buffer memory and the MMU routing RAM can be accessed. The VME slave module also transmits the VME bus cycles to the VMV bus through the MMU routing module. The VME slave module can be a VME interruptor.

**VSB slave** The VSB slave module is similar to the VME slave module with the same abilities. The VSB mapping is done through a 16 Mbyte window with a software programmable offset. After a VME reset the VSB slave port is disabled. The VSB slave module can be a VSB interruptor.

**MMU routing module** The MMU (Memory Managing Unit) routing module acts as a dynamic decoder over the VME bus and the VSB bus. The different address fields are divided into 1 Mbyte windows covering the complete addressing range. Each page can be marked to be taken by the VMV master module to be sent over the VMV bus to other VMV slave units. When a page is marked the high address field, the VME destination crate and other specific informations are defined in the associated page descriptors. A total of 8196 page descriptors are stored in the MMU RAM.

**Internal buffer memory** The 32 bit internal buffer memory module is triple ported via VME, VSB and VMV and locally arbitrated. The memory area up to 512 kbytes is mapped in the VMV master internal register accessible from the VME and VSB bus.

## B.4 CIP2000 Trigger System Readout software

The software of the CIP2000 readout system is written in C/C++ in POSIX standard. All software is stored in a CVS [61] repository with the name `cip2000-daq` in the H1 CVS framework.

Several processes on the different CPUs in the readout system handle the data transfer and communication. Figure B.7 gives an overview of the processes and communication structures on the different CPUs. Processes handling the monitoring and the control system e.g. via the PVSSII system are not included in the figure and are not a subject of this description. Four CPUs each housed in one trigger crate labeled from `cip2000-0` to `cip2000-3` handle the full readout. The CPU `cip2000-0` is the master CPU controlling the whole system. It runs the master process called `mastercrate`. It handles the basic event loop until all data of the event is saved into a data structure. On the other CPUs just one process is running called `slavecrate`. This process handles the local readout of the trigger cards and the communication to the main CPU. On a positive trigger decision (`L2Keep`) the pipelines in the trigger cards are already stopped by the `L1Keep` signal and the relevant data is copied into readout registers. The `L2Keep` signal arrives at all CPUs via a lemo connector from the STC system. The `slavecrate`

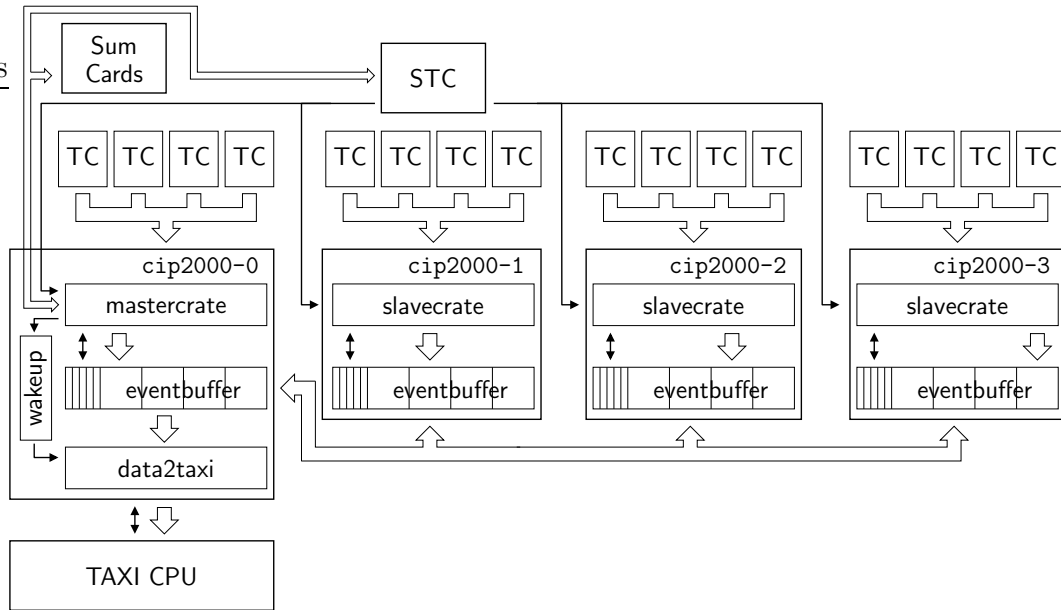


Figure B.7: *Readout structure of the CIP2000 readout system software. The master CPU called `cip2000-0` controls the whole system running the main event loop. The communication and the data transfer between the master CPU and the slave CPUs is handled via the pVIC bus and the `eventbuffer` data structures. The master CPUs run another process called `data2taxi` arranging the data transfer from the `eventbuffer` to the central DAQ in an asynchronous way.*

processes on all CPUs are in a state waiting for a command from the `mastercrate` process to start the readout of the trigger cards into a so called `eventbuffer` structure. The detailed structure of the `eventbuffer` is described later in this section. All the data storage and the control mechanisms between the different CPUs are handled via the `eventbuffer`. The `mastercrate` process itself reads out its trigger cards and stores the data into the `eventbuffer`. The arbitration of the pVIC bus for DMA accesses has to be implemented in the software itself. The `mastercrate` grants the bus to the first slave CPU by setting a control register in the `eventbuffer` structure on the slave CPU. On this command the slave CPU sends its data via a DMA transfer on the pVIC bus to the `eventbuffer` of the master CPU and releases the bus afterwards by setting a register in the `eventbuffer` of the main CPU. Now the main CPU grants the bus to the next CPU and so on until all data is collected in the `eventbuffer` structure of the main CPU. Inbetween the `mastercrate` process collects all additional information from the STC system and e.g. the Sum Cards to crosscheck the data. The `eventbuffer` of the master CPU is pipelined in 32 steps. After the full readout is done the `mastercrate` process acknowledges the end of the readout to the STC system and a new event can be triggered. If the `eventbuffer` of the master CPU is full the end of the readout is not acknowledged until a free buffer is found.

Bank written in runstart record	
CTST	General setup bank of CIP2000 trigger system
CTSS	Additional setup bank of CIP2000 trigger system
CTSK	Setup bank of so called komposti cards (not described here)
CRMD	Bank with dead channels
Banks written each event	
TSTC	Bank of STC information for crosschecks in central DAQ
CRM2	Bank of pad numbers of active pads in all chambers
CRMS	Bank with histograms read out from different sum cards
CRMZ	Bank with z-vertex histogram for 16 bunch crossings (special runs)
CIPT	Bank for timing monitoring

Table B.1: *Description of banks written by the CIP2000 trigger readout.*

The second stage of the readout is asynchronous to the frontend readout. A second process on the main CPU called `data2taxi` cares for the data transport of the events to the central DAQ system of H1. The process looks for full buffers in the `eventbuffer` of the main CPU. If the process finds a full buffer it reserves a buffer in the TAXI CPU where the data has to be transferred to. It translates the read out raw data from the trigger cards to unique pad numbers reducing the data in case of low occupancy of the chambers and crosschecks of the data are applied here. All data is formatted into banks in the BOS format used at H1. Table B.1 shows an overview of all banks written by the CIP2000 trigger readout. The `data2taxi` process normally sleeps and runs with a low priority to not disturb the `mastercrate` process what would lead to deadtimes in the readout. After an event is read out by the `mastercrate` process the `data2taxi` process is woken up by a communication via a pipe with help of the `wakeup` process. Figure B.8 shows the structure of the `eventbuffer` used on all CPUs to collect the read out data and to establish the communication via the pVIC bus. The buffers on the slave CPUs just hold the data from the crate connected to.

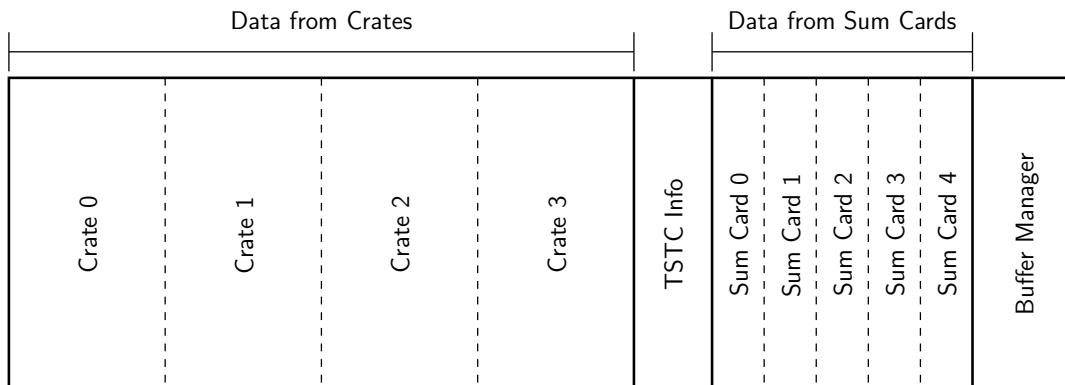


Figure B.8: *Eventbuffer structure.*

Programs	
<code>mastercrate.c</code>	Program running the main event loop on master CPU
<code>slavecrate.c</code>	Program for trigger card readout on the slave CPUs
<code>data2taxi.c</code>	Program for asynchronous readout from the events in the <code>eventbuffer</code> of the main CPU to the TAXI CPU.
Libraries	
<code>eventbuffer.c/.h</code>	Handling of eventbuffers in the different CPUs.
<code>vmeaccess.c/.h</code>	Low-level functions to access the VME bus.
<code>pvicaccess.c/.h</code>	Handling of the pVIC bus (DMA access, messages and arbitration).
<code>trigcard.C/.h</code>	Library to access the trigger cards.
<code>stcaccess.c/.h</code>	Library to access the STC cards.
<code>sumcard.c/.h</code>	Library to access and initialise the Sum Cards.
<code>taxiio.c/.h</code>	Higher-level functions to access the TAXI CPU.
<code>taxilib.c/.h</code>	Basic library to access the TAXI CPU.
<code>xiuserlib.c.c/.h</code>	Low-level library to access the TAXI CPU (general use at H1).
<code>bos.c/.h</code>	Library to write BOS banks. Some functions to adjust pad numbers due to multiplexing problems are implemented here.
<code>trigsim.C/.h</code>	High-level functions for subtrigger simulation and comparison to read out data banks.
<code>H1CIP2kSim.C/.h</code>	Library with full subtrigger simulation based on chamber data. The output can be accessed at different stages of the trigger algorithm for online checks.
<code>wakeup.c/.h</code>	Low-level functions for interprocess communication of <code>mastercrate</code> and <code>data2taxi</code> process via a pipe.
<code>cleanup.c/.h</code>	Library to setup signal handlers to execute cleanup functions.
<code>message.h</code>	Definition of messages in readout procedure.
<code>ssp.c/.h</code>	Library to send messages to the supervisor.

Table B.2: *Description of files in the CIP2000 trigger readout package.*

The master CPU buffer holds all information of the event after the full readout is done. The buffer manager part of the `eventbuffer` holds control registers to establish a messaging system between the different CPUs. The registers are used in a semaphoric way to grant the pVIC bus just to one CPU at a time. Table B.2 gives an overview of the different files and libraries used in the CIP2000 trigger readout and its usage.

# Bibliography

- [1] H. P. Nilles, Phys. Rept. **110** (1984) 1.
- [2] H. E. Haber and G. L. Kane, Phys. Rept. **117** (1985) 75.
- [3] S. R. Coleman and J. Mandula. Phys. Rev. **159** (1967) 1251.
- [4] S. P. Martin, *A supersymmetry primer*, 1997, hep-ph/9709356.
- [5] H. Georgi and S. L. Glashow, Phys. Rev. Lett. **32** (1974) 438.
- [6] G. Jikia, *Excited quark production at ep and  $\gamma p$  colliders*, Nucl. Phys. **B333** (1990) 317-334.
- [7] S. J. Brodsky and S. D. Drell, Phys. Rev. **D22** (1980) 2236.
- [8] F. M. Renard, Phys. Lett. **B116** (1982) 264.
- [9] U. Baur, M. Spira and P. Zerwas, Phys. Rev. **D42** (1990) 815.
- [10] F. Boudjema, A. Djouandi and J. L. Kneur, Z. Phys. **C57** (1993) 425.
- [11] H1 Collaboration, I. Abt et al., Nucl. Instr. and Meth. **A386** (1997) 310.
- [12] H1 Collaboration, I. Abt et al. Nucl. Instr. and Meth. **A386** (1997) 348.
- [13] E. Elsen, *The H1 Trigger and Data Acquisition System*, H1 internal note, H1-01/93-262.
- [14] W. J. Haynes, *VMEtaxi Mark-2 System Software Package*, July 1993, DESY, Version 4.2, unpublished.
- [15] F. Halzen and A. D. Martin, *Quarks and Leptons: An Introductory Course In Modern Particle Physics*, Wiley, New York, 1984.
- [16] O. Nachtmann, *Phenomena And Concepts Of Elementary Particle Physics*, Vieweg, Braunschweig, 1986.
- [17] Internal H1Oolt Documentation:, *H1Oolt Analysis Framework Homepage*, <https://www.desy.de/~laycock/Work/H1Lt/documentation/htmlldoc/>.

- [18] Internal H1OO Documentation:, *H1OO Analysis Framework Homepage*, <http://www-h1.desy.de/icas/oop/>.
- [19] T. Sjostrand et al., *Computer Physics Commun.* **135** (2001) 238-259, hep-ph/0010017.
- [20] B. Andersson, G. Gustafson, G. Ingelman and T. Sjostrand, *Phys. Rept.* **97** (1983) 31.
- [21] M. Glück, E. Reya and A. Vogt, *Phys. Rev.* **D45** (1992) 3986.
- [22] H. L. Lai et al., *Eur. Phys. J.* **C12** (2000) 375, hep-ph/9903282.
- [23] H. Jung, *Comp. Phys. Commun.* **86** (1995) 147.
- [24] A. Kwiatkowski, H. Spiesberger and H. J. Mohring, *Comp. Phys. Commun.* **69** (1992) 155.
- [25] T. Köhler, Diploma thesis, *Ereignisgeneratoren zur Elektron Proton Streuung bei HERA*, 1989 (Aachen).
- [26] G. P. Lepage, *Journal of Computational Physics* **27** (1978) 192-203.
- [27] T. Sjostrand and M. Bengtsson, *Computer Physics Commun.* **43** (1987) 367.
- [28] Ch. Berger, M. Spira, J. Tutas and P. M. Zerwas, *Proceedings of the HERA Workshop Vol.2*, **851** (1987).
- [29] Ch. Berger, W. Wagner, *Phys. Reports* **146** (1987).
- [30] R. Brun, F. Bruyant, M. Maire, A. C. McPherson and P. Zancarini, CERNDD/EE/84-1.
- [31] C. Veelken, *H1NonepBgFinder - Rejection of cosmic muon and beam-halo events in the H1OO framework*, H1 internal note, August 2002, H1-IN-603(09/2002).
- [32] E. Chabert et al., *QBGFMAR: An Updated Phan Package for Cosmic and Halo Muon Topological Rejection in High PT Physics Analysis*, H1 internal note, August 1998, H1-IN-556(11/1998).
- [33] M. Rudowicz, Diploma thesis, *Algorithmen zur Kalorimetersimulation mit parametrisierten Schauern am Beispiel des H1-Detektors*, 1989 (Munich).
- [34] L. Goerlich, H. P. Wellisch, H1 Internal Note, H1-IN-204 (1991).
- [35] V. Shekelyan, *Simulation and Reconstruction in the H1 Liquid Argon Calorimeter*, H1 internal note, H1-04/93-288 (1993).
- [36] J. Marks, *QESCAT - e identification software in H1PHAN* (1996), H1 internal note, [https://www.desy.de/~marks/electron/phan\\_e\\_finder.html](https://www.desy.de/~marks/electron/phan_e_finder.html).

- [37] B. Heinemann, Dissertation thesis, *Measurement of Charged Current and Neutral Current Cross Sections in Positron-Proton Collisions at  $\sqrt{s} = 300 \text{ GeV}$* , 1999 (Hamburg).
- [38] G. C. Blazey et al., *Run II Jet Physics: Proceedings of the Run II QCD and Weak Boson Physics Workshops*, 2000, hep-ex/0005012.
- [39] S. Catani, Y. L. Dokshitzer, M. H. Seymour and B. R. Webber, Nucl. Phys. **B406** (1993) 187.
- [40] M. Wobisch, Dissertation thesis, *Measurement and QCD analysis of jet cross sections in deep- inelastic positron proton collisions at  $\sqrt{s} = 300 \text{ GeV}$* , 1999 (Aachen).
- [41] H1 Collaboration, C. Adloff et al., Eur. Phys. J. **C19** (2001) 289.
- [42] Internal H1OO Documentation: M. Peez, B. Portheault and E. Sauvan, *An energy flow algorithm for Hadronic Reconstruction in OO: Hadroo2*, 2005.
- [43] DELPHI Collaboration, P. Abreu et al., Eur. Phys. J. **C8** (1999) 41.
- [44] H1 Collaboration, C. Adloff et al., DESY-00-102, July 2000.
- [45] I. Négri, Dissertation thesis, *Recherche de fermions excités dans l'expérience H1 auprès du collisionneur positron-proton HERA*, 1998 (Marseille).
- [46] T. Junk, *Confidence Level Computation for Combining Searches with Small Statistics*, Nucl. Instrum. Meth. **A434** (1999) 435.
- [47] A. L. Reed, *Optimal Statistical Analysis of Search Results based on the Likelihood Ratio and its Application to the Search for the MSM Higgs Boson at  $\sqrt{s} = 161$  and  $171 \text{ GeV}$* , 1997, DELPHI note 97-158 PHYS 737.
- [48] ZEUS Collaboration, S. Chekanov et al., *Searches for excited fermions in ep collisions at HERA* Phys. Lett. **B549** (2003) 32-47.
- [49] DELPHI Collaboration, P. Abreu et al., Eur. Phys. J. **C8** (1999) 41.
- [50] H1 Collaboration, *ep Physics beyond 1999*, H1 internal note, October 1997, H1-10/97-531.
- [51] J. Becker, Diploma thesis, *The Data Acquisition and Control System for a Fast Trigger at H1*, 2000 (Heidelberg).
- [52] M. Urban, Dissertation thesis, *The new CIP2k z-Vertex Trigger for the H1 Experiment at HERA*, 2003 (Zurich).
- [53] M. Urban, Diploma thesis, *Ein schneller Trigger für H1 bei HERA*, 2000 (Heidelberg).

- [54] VITA – VMEbus International Trade Association,  
VME64 (ANSI/VITA 1-1994), <http://www.vita.com>.
- [55] Altera, APEX 20k Programmable Logic Device Family,  
<http://www.altera.com>.
- [56] Lattice Semiconductor Corporation, Specifications ispLSI 1048E,  
<http://www.latticesemi.com>.
- [57] Lattice Semiconductor Corporation, 1000EA, 1000E and 1000 family archi-  
tectural description, <http://www.latticesemi.com>.
- [58] CES – Creative Electronic Systems,  
RIO 8062 Power PC based RISC I/O Board.
- [59] CES – Creative Electronic Systems,  
pVIC Systems 4025/4425/7225/8025/8425/8426 PCI to PCI connections.
- [60] CES – Creative Electronic Systems,  
VIC 8250 VMV to VME One Slot Interface.
- [61] CVS – Concurrent Versions System homepage, <https://www.cvshome.org>.

# Acknowledgements

I would like to thank Prof. Dr. Ulrich Straumann and Prof. Dr. Peter Truöl giving me the opportunity to work at the Physik Institut of the University of Zurich and in the H1 collaboration.

I am totally grateful to Dr. Katharina Müller being absolutely patient with me throughout the whole analysis and giving me support at any time.

Thanks to all my colleagues in Hamburg and Zurich and of course all CIP group members. Specially I would like to thank Max Urban for all the years we accompanied us through the CIP project. Many thanks to Stefan Schmitt for teaching me so many things and to always having an answer to almost everything.

Many thanks to all H1 members for the fruitfull discussions and pleasent work at H1. Specially I would like to thank: A. Schoening, A. Rimmer, C. Veelken and I. Mudhahir.

I would like to thank my parents for allways being there when I need them.

I would like to thank Diana for her love and patience!



# Curriculum Vitae

## Personalien

Name	Becker
Vorname	Jan
Geburtsort	Hamburg
Geburtstag	11.03.1975
Staatsangehörigkeit	deutsch

## Bildungsgang

1981 - 1985	Gottfried-Keller-Grundschule in Norderstedt, Deutschland
1985 - 1994	Copernicus Gymnasium in Norderstedt, Deutschland
1994	<b>Abitur</b>
1995 - 2001	Studium der Physik an der Ruprecht-Karls-Universität Heidelberg, Deutschland
Juli 1997	<b>Vordiplom</b>
2000 -2001	Diplomarbeit in der experimentellen Hochenergiephysik unter der Leitung von Prof. Dr. F. Eisele mit dem Titel: <i>“The Data Acquisition and Control System for a Fast Trigger at H1”</i>
Januar 2001	<b>Diplom in Physik</b> (Nebenfach: Informatik, Wahlfach: Elektronik)
2001 - 2005	Wissenschaftliche Mitarbeit am Physik-Institut der Universität Zürich
	<b>Promotion</b> unter der Leitung von Prof. Dr. U. Straumann
2001 - 2005	Forschungsaufenthalt am Deutschen Elektronen Synchrotron (DESY) am H1 Detektor in Hamburg, Deutschland
2005	<b>Dissertation</b> mit dem Titel: <i>“A Search for Excited Quarks with the H1 Detector at HERA”</i>